

Electron Equations of State During Magnetic Reconnection

ARCHIVES

by

Ari Le

A.B., Brown University (2006)

Submitted to the Department of Physics
in partial fulfillment of the requirements for the degree of

Doctor of Philosophy in Physics

at the

MASSACHUSETTS INSTITUTE OF TECHNOLOGY

June 2012

© Massachusetts Institute of Technology 2012. All rights reserved.



Author

Department of Physics

May 4, 2012



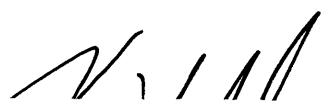
Certified by



Jan Egedal

Associate Professor

Thesis Supervisor



Accepted by



Krishna Rajagopal

Professor, Associate Department Head for Education

Electron Equations of State During Magnetic Reconnection

by

Ari Le

Submitted to the Department of Physics
on May 4, 2012, in partial fulfillment of the
requirements for the degree of
Doctor of Philosophy in Physics

Abstract

Magnetic reconnection is a rapid reconfiguration of the magnetic field lines in a plasma that converts stored magnetic energy into particle energy in a wide range of environments. It is a source of energetic particles in the solar corona and wind, and in planetary magnetospheres. Disruptive reconnection in laboratory fusion experiments rapidly deconfines the plasma. While reconnection alters the global magnetic field and plasma properties, it depends on small-scale local electron dynamics. Particularly in collisionless plasmas, velocity-space anisotropy of the electrons plays a leading role in governing the energy exchanges and shaping the currents that develop during reconnection. The anisotropy results from an electric field parallel to the magnetic field that tends to accelerate electrons towards the site of reconnection. In this thesis, the equations of state that describe the main anisotropy of the electrons during collisionless reconnection are derived. The equations of state give the components of the electron pressure tensor parallel and perpendicular to the magnetic field as functions of the plasma density and magnetic field strength. Through comparison to numerical solutions of the kinetic plasma equations of motion starting from a variety of initial conditions, several predictions and consequences of the equations of state are tested. The electron pressure anisotropy feeds back on the magnetic geometry of the reconnection region and drives narrow current layers. The dynamics depend on the plasma parameters, and electron heating is most extreme when the electron pressure is much smaller than the magnetic field pressure.

Thesis Supervisor: Jan Egedal
Title: Associate Professor

Acknowledgments

Thanks, Jan!

And thanks, Bill, for all the data!

Contents

1	Magnetic Reconnection	15
2	Electron Distributions	29
3	The Equations of State	39
4	Strong Guide Field Regime	47
5	Neutral Sheet Reconnection	57
6	Guide Field and Mass Ratio Scans	73
7	Extensions	93
7.1	Asymmetric Current Sheets	94
7.2	Reconnection with Fully 3D Evolution	97
7.3	Island Merging	103
8	Summary of New Results	113
A	Waves Launched by Island Merging	115
B	Including Collisions	121
C	Particle-in-Cell Codes	125

List of Figures

1-1	Some possible reconnection scenarios reproduced from Ref. [1].	16
1-2	Magnetic field lines associated with currents on the Sun's surface (Ref. [5]).	17
1-3	Reconnection in the geotail driven by the interaction with the solar wind. (Top: ESA. Bottom: Ref.[12].)	18
1-4	Geotail and Equator-S measurements of flows believed to be driven by reconnection in Earth's magnetopause. (Ref. [15]).	19
1-5	Sawteeth in the ST tokamak (Ref. [29]) and disruptive instabilities in the PLT tokamak (Ref. [31]).	20
1-6	Equatorial cross-section of the VTF device during two discharges showing the inductive electric field $\propto \partial A_\phi / \partial t$, which illustrates the 3D localized onset of reconnection in the experiment (Ref. [33]).	21
1-7	Parker's picture of Sweet's mechanism on the Sun [56].	25
1-8	Top: An early fluid simulation of the $m = 1$ mode in a tokamak (Ref. [60]). Bottom: A recent fully-kinetic, three-dimensional simulation of a reconnecting current sheet (Ref. [63]).	27
2-1	One-dimensional distribution function for particles trapped in a potential that varies slowly in time.	32
2-2	Reconnection geometry with typical passing (red) and trapped (blue) electron orbits and the phase space density f_e	34
2-3	Trapped and passing particles in a flux tube populate different regions of velocity space.	36

2-4	Electron distribution observed by Wind during reconnection.	37
3-1	One-dimensional pressure p and density n as functions of potential U	42
3-2	One-dimensional equation of state: pressure p as a function of density n	42
3-3	The equations of state.	45
4-1	Profiles from a PIC simulation of reconnection with a strong guide field along with sample particle distributions.	49
4-2	Parallel potential in a PIC simulation of reconnection with a guide magnetic field.	51
4-3	Comparison of direct PIC simulation results to the equations of state, which predict the pressure and parallel potential profiles based on the PIC density and magnetic field strength.	52
4-4	Comparison of equation of state for the parallel pressure to simulation results at two different mass ratios.	54
4-5	Prediction for the parallel electron current compared to PIC results.	55
4-6	Comparison of kinetic simulation to fluid simulations, with and without the new equations of state.	56
5-1	Profiles from a PIC simulation of neutral sheet reconnection.	59
5-2	Pressure ratio and magnetic field strength with a typical trapped electron orbit.	60
5-3	The magnetic tension and electrical forces acting on an electron fluid element in an outflow jet.	62
5-4	The magnetic tension force (green arrows) on an electron fluid element is balanced by anisotropic pressure gradients.	63
5-5	Magnetic tension and anisotropic pressure dominate x momentum	63
5-6	Pressure anisotropy and magnetic tension along a simulation cut.	64
5-7	Predicted scaling laws and values from three simulations.	66
5-8	Cluster spacecraft observations of electron distributions are consistent with a parallel potential of $e\Phi_{\parallel} \sim 100T_e$	67

5-9	Density, parallel electric field, and parallel potential in a large PIC simulation.	67
5-10	Simple model for the electron currents in a jet.	69
5-11	High-resolution electron phase space distributions from the paper by Ng <i>et al.</i> [100]	70
5-12	Electron bouncing motion generates finger-like phase space structures.	71
6-1	Guide field and mass ratio scan: plasma density n normalized to background density n_∞	77
6-2	Electron pressure anisotropy p_{\parallel}/p_{\perp}	78
6-3	Ratio of electron Larmor radius to magnetic field radius of curvature, ρ_e/R_B	79
6-4	Exhaust electron flow u_{ex} normalized to thermal speed v_{the}	81
6-5	Out-of-plane electron flow u_{ey} normalized to thermal speed v_{the}	82
6-6	Ratio of electron Larmor radius to magnetic field radius of curvature, ρ_e/R_B . (Color scale altered.)	83
6-7	Pressure anisotropy and electron jets with varying guide magnetic fields ($m_i/m_e = 400$).	84
6-8	Hall electric and magnetic fields above and below the guide field threshold for jet formation.	86
6-9	The Hall currents become asymmetric in the presence of a guide field.	87
6-10	New type of magnetized electron jet driven by pressure anisotropy (at physical proton mass ratio and $B_g = 0.282B_0$).	89
6-11	Reconnection regimes for different guide fields and mass ratios m_i/m_e	91
7-1	Magnetopause reconnection geometry.	94
7-2	Parallel potential and electron pressure anisotropy during asymmetric reconnection.	96
7-3	Two fluxropes in a 3D PIC simulation.	98
7-4	Ratio p_{\parallel}/p_{\perp} in a 3D PIC simulation.	100

7-5	Test of the equations of state in 3D on isosurfaces of magnetic field strength. Pressure moments from the PIC data (green and blue) are compared to predictions of the equations of state based on the PIC density and magnetic field strength.	101
7-6	Test of the equations of state during 3D reconnection with asymmetric density.	102
7-7	Cartoon of plasmoids formed in the corona (reproduced from Ref. [127])	104
7-8	Magnetic island coalescence: density and sample field lines.	106
7-9	Parallel potential and temperature, and equations of state between merging magnetic islands.	109
7-10	Electron distribution for pitch angles parallel and perpendicular to the magnetic field during island merging.	110
A-1	Electric field component with resonance and cut-off layers.	116
A-2	CGL equations of state hold in the wave.	118
A-3	Electron distribution outside the resonance layer.	119
B-1	Acceleration potential in weakly collisional plasmas.	123
B-2	Electron outflow jets.	124

List of Tables

6.1 Simulation parameters.	75
------------------------------------	----

Chapter 1

Magnetic Reconnection

Magnetic reconnection is a fundamental process in plasmas that converts magnetic energy into particle energy through a rapid reconfiguration of the magnetic field lines [1-4]. While reconnection alters global plasma properties, it depends on small-scale local electron dynamics. Particularly in collisionless plasmas, velocity-space anisotropy of the electrons plays a leading role in shaping the currents and governing the energy exchanges near reconnection sites. In this thesis, equations of state that describe the main anisotropy of the electrons are derived. In addition, several predictions are tested, including how the electron pressure anisotropy feeds back on the magnetic geometry of the reconnection region and how these effects depend on the plasma parameters.

A few possible reconnection scenarios are sketched in Fig. 1-1. In (a) and (b) on top, oppositely directed, open field lines merge. Note that in (a) plasma from the left and right is initially not connected by field lines, but in (b) those regions may lie on the same field line. This topological rearrangement is what is implied by the term reconnection. Reconnection may also occur in closed field line configurations. For example, in the bottom figures, magnetic islands encircled by closed field lines either (a) separate or (b) coalesce. The field lines in these cartoons are shown in a single plane, with reconnection occurring at magnetic nulls where the magnetic field goes to zero. Reconnection is also possible, however, when there is a guide magnetic field, a component of magnetic field out of the plane. In guide field reconnection, the

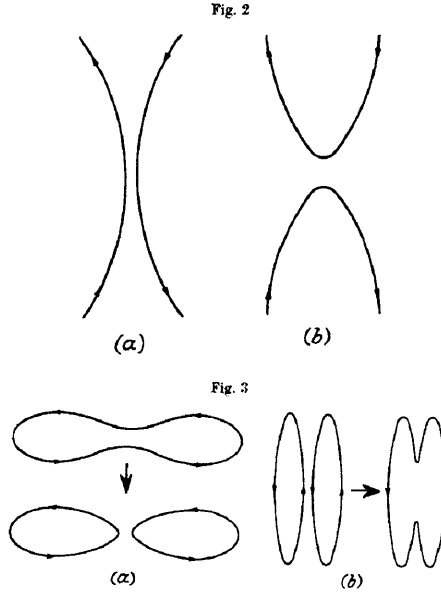


Figure 1-1: Some possible reconnection scenarios reproduced from Ref. [1].

magnetic field is typically sheared, and only certain components reverse direction. The total magnetic field need not go to zero.

Reconnection was first proposed as a dynamical process in the solar corona [5]. The magnetic fields associated with sunspots are hypothesized to interact and drive currents in the solar plasma depending on the complicated 3D field geometry. A cartoon from Giovanelli's paper is reproduced in Fig. 1-2. The energy stored in the solar magnetic fields is substantial. The magnetic energy density in the corona is typically much larger than the thermal energy density of the plasma, with $\beta < 1\%$ (where β is the plasma thermal pressure normalized to magnetic pressure). It is assumed that solar flares and other eruptive solar phenomena derive their energy, which can be upwards of 10^{32} ergs for a single large flare, from the magnetic field. Reconnection is the best candidate for transferring magnetic energy into the plasma, and it likely produces high-energy electrons in the 10s to 100s of keV range [6, 7]. Although there is still no complete model for how solar reconnection occurs, there is ample evidence for reconnection and concomitant electron and ion energization during flares and coronal mass ejections [8-10].

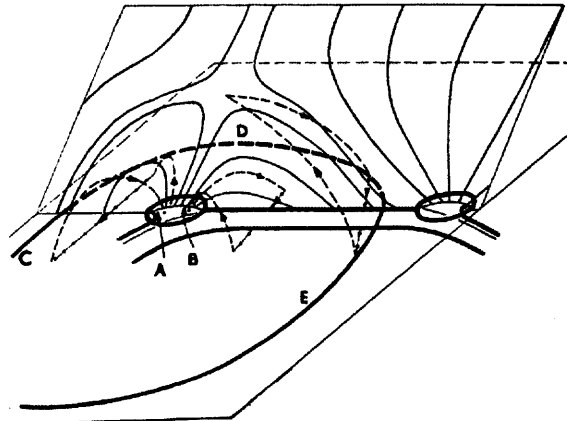


FIG. 2.—Magnetic field and current distribution in a growing bipolar spot group.

Figure 1-2: Magnetic field lines associated with currents on the Sun's surface (Ref. [5]).

Reconnection also couples the solar wind to Earth's magnetosphere [1]. The Earth's global dipole field prevents most of the flux of charged particles in the solar wind from entering Earth's atmosphere, but reconnection can allow magnetic field lines from the interplanetary magnetic field to become connected with Earth. This process is most prevalent around the magnetopause, the boundary between the solar wind and Earth's magnetosphere where the solar wind dynamical pressure is roughly equal to the magnetic pressure of Earth's dipole field. Meanwhile, on the night side, Earth's magnetosphere is stretched into an elongated tail by the solar wind. A current layer is induced in the neutral sheet, where the magnetic field is weak and across which the field changes direction. Already 46 years ago, it was pointed out that this configuration could be unstable to a reconnecting mode and that the reconnection could produce energetic electrons [12]. The reconnected field topology is illustrated in Fig. 1-3.

Several spacecraft orbiting Earth, equipped with magnetic and plasma measurement instruments, have diagnosed magnetospheric reconnection. Evidence for reconnection has been detected around the magnetopause, for example, by the ISEE satellites [13]. More detailed measurements suggested that the POLAR spacecraft

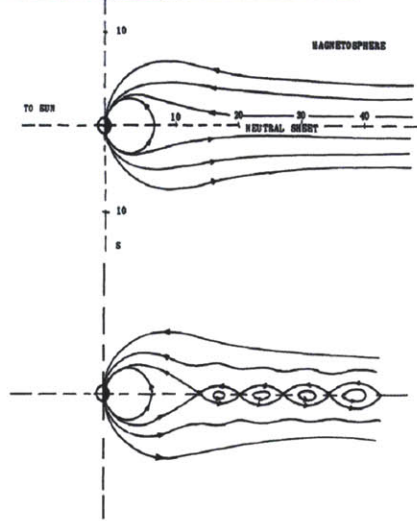
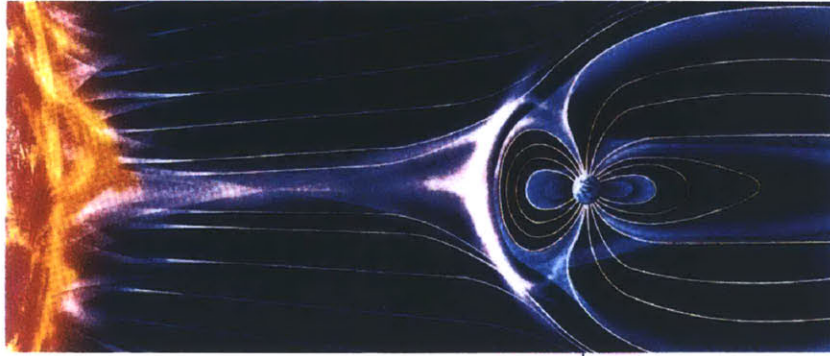


Figure 1-3: Reconnection in the geotail driven by the interaction with the solar wind. (Top: ESA. Bottom: Ref.[12].)

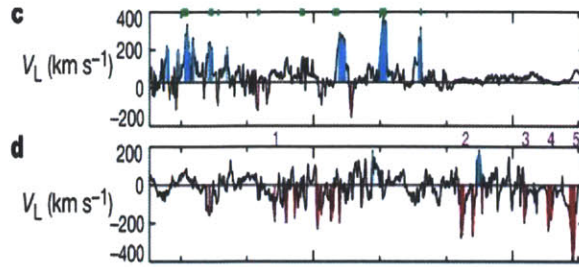


Figure 1-4: Geotail and Equator-S measurements of flows believed to be driven by reconnection in Earth’s magnetopause. (Ref. [15]).

flew through a reconnection diffusion region [14], where localized kinetic effects are essential. Geotail and Equation-S measurements indicated reconnection outflows in the magnetopause, and some data are plotted in Fig. 1-4 from Ref. [15]. The reconnection signature is the intense plasma flows of opposite direction, which are posited to be composed of exhaust plasma accelerated by reconnection. In the magnetotail, there is ample evidence for reconnection from the Wind spacecraft [16] and the four Cluster spacecraft [17]. THEMIS, WIND, and Cluster measurements include full electron particle distributions, which will be shown to develop characteristic anisotropies in the following chapters [17-25]. The Magnetospheric Multiscale (MMS) mission will be launched in a few years, and it has the explicit goal of measuring in higher resolution the characteristics of the electron diffusion region during magnetic reconnection [26]. In more distant environments, the Voyager 2 spacecraft collected data suggesting reconnection occurs both in the far solar wind [27] and in the dayside magnetosphere of Uranus [28].

Plasma fusion experiments are also subject to reconnection. Sawtooth oscillations in the core temperature are regularly observed in tokamak plasmas and were first noted on the ST tokamak [29]. Sawteeth are a series of intermittent rapid drops in the core temperature, inferred from X ray emission from hot electrons. Between these fast losses of core thermal energy, comparatively slow reheating of the core. Some of the first measurements are shown in Fig. 1-5, where the traces follow the characteristic sawtooth pattern. An early model by Kadomtsev [30] attributes sawteeth to an

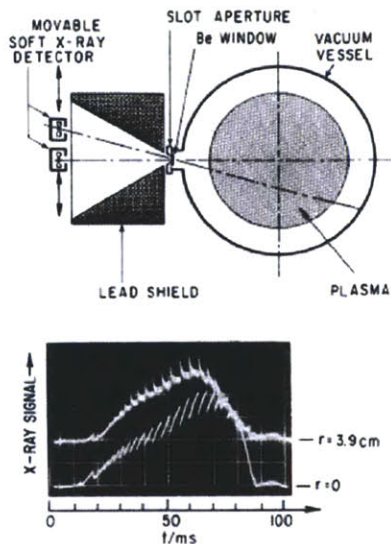


FIG. 1. Experimental arrangement of x-ray detectors. The x-ray traces exhibit internal disruptions.

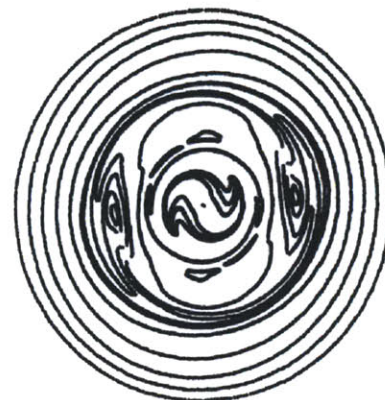


FIG. 7a. Contours of equal X-ray emissivity for the $m = 2$ mode.

Figure 1-5: Sawteeth in the ST tokamak (Ref. [29]) and disruptive instabilities in the PLT tokamak (Ref. [31]).

internal resistive kink mode that forms a magnetic island through reconnection when the safety factor q , the number of poloidal field line windings per toroidal winding, drops below one in the plasma core. The mode is resonant at the $q = 1$ surface, and it causes a large magnetic island to form and shift the hot core outwards, transporting thermal energy. The detailed predictions of the model are incorrect, but sawteeth almost certainly involve reconnection. More violent, but related to sawteeth, are disruptive instabilities [31], which rapidly dump the stored energy in the tokamak. Evidence for an $m = 2$ mode is evident in the tomographic X ray data from a disruption on the PLT tokamak in Fig. 1-5. The island structure is clear evidence that reconnection changed the initial magnetic topology of nested toroidal flux surfaces.

Basic plasma physics experiments have also documented reconnection in detail. Several laboratory experiments are devoted to studying magnetic reconnection. At MIT, VTF experiments have diagnosed reconnection with a guide field in the collisionless regime in a toroidal device [32]. It was later found that this reconnection

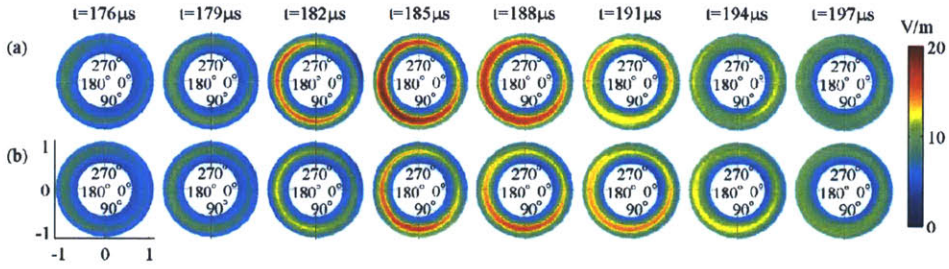


Figure 1-6: Equatorial cross-section of the VTF device during two discharges showing the inductive electric field $\propto \partial A_\phi / \partial t$, which illustrates the 3D localized onset of reconnection in the experiment (Ref. [33]).

could be fully 3D, with non-axisymmetric onset [33]. The inductive reconnection electric field in VTF during non-axisymmetric reconnection is plotted in Fig. 1-6, which shows cross sections of the equatorial plane of the device at various times during a plasma shot. Furthermore, electrostatic turbulence is prevalent during reconnection in VTF, and non-linear disturbances such as electron holes have been observed and characterized [34]. Reconnection has also been observed in a linear discharge plasma at UCLA [35]. There, reconnection was driven by the magnetic attraction of interacting current channels. At PPPL, driven reconnection experiments without a guide field are performed on the toroidal MRX device [36]. A notable result was the identification of Hall physics signatures, particularly a signature quadrupolar magnetic field perturbation [37]. Similar Hall fields were also observed in the Swarthmore Spheromak Experiment, where 3D effects have been studied by merging two spheromak plasmas [38]. At Los Alamos, the Reconnection Scaling Experiment observes multiple flux tubes merging during 3D evolution in a linear chamber [39]. Finally, reconnection has also been observed in laser-produced high-energy-density plasmas. Because of the intense density and temperature gradients produced on laser illuminated metallic foils, megagauss magnetic fields may be generated, and these fields have been observed to undergo reconnection [40-42].

Despite the large amount of observational data, there are gaps in the theoretical understanding of reconnection. On large scales, high-temperature plasmas are generally very good electrical conductors, with a classical collisional resistivity that scales

as $\eta \propto 1/T_e^{3/2}$. In the ideal limit where resistivity and other effects are neglected, the electric field in the plasma frame is zero,

$$\mathbf{E} + \mathbf{u} \times \mathbf{B} = 0. \quad (1.1)$$

This condition places stringent constraints on the evolution of the magnetic field, which evolves as though it were frozen into the plasma flow \mathbf{u} [43]. For example, any two plasma fluid elements that are connected by a magnetic field line continue to be connected by magnetic field lines in an ideal plasma. The magnetic helicity and related field-line linking numbers, global quantities that depend on the topology of the magnetic field, are also conserved [44, 45]. Processes that break these topological constraints include Taylor relaxation [46] (which breaks the first constraint, but conserves helicity) and reconnection (which breaks both). By breaking the frozen-in law, these phenomena involve plasma evolution towards lower energy states that are inaccessible through ideal motions. During reconnection, particularly in collisionless plasmas, the breaking of the frozen-in condition is tied to small-scale electron dynamics. The modeling of reconnection in this case is difficult because reconnection couples kinetic, non-ideal electron-scale processes to the global plasma evolution.

An immediate consequence of Eq. 1.1 is that the electric field parallel to the magnetic field $E_{\parallel} = \mathbf{E} \cdot \mathbf{B}/|\mathbf{B}| = 0$. A necessary condition for reconnection in an open field line system without neutral points (where $\mathbf{B} = 0$) is that the parallel potential,

$$\Phi_{\parallel}(\mathbf{x}) = \int_{\mathbf{x}}^{\infty} \mathbf{E} \cdot d\mathbf{l} \quad , \quad (1.2)$$

not be everywhere zero [47, 48]. In 1.2, the integral is taken along the magnetic field line out to an ambient ideal plasma where $E_{\parallel} = 0$. This result follows directly from Maxwell's equations, and it makes no assumptions about how E_{\parallel} is supported by the plasma. As will be shown in the next chapter, Φ_{\parallel} arises naturally in a different context when considering the adiabatic motion of magnetized electrons near sites of reconnection. In fact, Φ_{\parallel} typically becomes far larger during reconnection than required simply by Maxwell's equations and the change of magnetic field topology.

The existence of a parallel electric field and a non-vanishing Φ_{\parallel} in a plasma is strongly tied to the electron dynamics. Recasting the electron fluid momentum conservation equation in the form of a generalized Ohm's law gives, for a quasi-neutral hydrogen plasma,

$$\mathbf{E} + \mathbf{u} \times \mathbf{B} = \eta \mathbf{J} + \frac{1}{ne} \mathbf{J} \times \mathbf{B} - \frac{1}{ne} \nabla \cdot \mathbb{P} + \frac{m_e}{ne^2} \delta_t \mathbf{J}, \quad (1.3)$$

where \mathbf{u} is the mean flow speed of the ions. The non-ideal terms on the right-hand side are neglected in the ideal MHD approximation. They take into account resistivity, the Hall effect, the divergence of the electron pressure tensor \mathbb{P} , and electron inertia. Resistivity can support a parallel electric field, and Ohmic heating will occur. As shown below, collisional resistivity alone is typically far too small to account for observed reconnection rates. The Hall effect reflects the fact that the electrons and ions move separately, and it is the electrons that typically carry most of the current. This alters the magnetic field structure of the reconnection region [49-52]. But Hall physics neither allows the magnetic topology to change, because the field remains frozen into the electron flow, nor is it necessary for reconnection to be fast [53]. Electron pressure tensor effects are very important during collisionless reconnection, and the equations of state of this thesis describe the main anisotropy of the electron pressure tensor during magnetic reconnection. Under most of the conditions considered in the following chapters, the pressure does not in itself allow the magnetic topology to change. It is found, however, that electron pressure gradients balance large parallel potentials Φ_{\parallel} , and parallel electron heating accounts for a substantial portion of energy gained by the plasma. The electron inertia in Eq. 1.3 is often negligible, but it can play a role in small-scale reconnection that seeds other instabilities [54].

Although the focus of this thesis is on reconnection in collisionless plasmas ($\eta = 0$), it is worth considering some models for reconnection based on breaking the frozen-in law through resistivity alone. The resistive models were the earliest models for reconnection, and they highlight some of the complexity of modeling reconnection that carries over into the collisionless regime. A useful parameter for quantifying the

importance of resistivity is the Lundquist number,

$$S = \mu_0 L V_{Alfven} / \eta. \quad (1.4)$$

Physically, S compares the time for an Alfvén wave to cross a plasma system of size L to the resistive diffusion time scale. A diffusive process would therefore occur over a time $\propto 1/S$. The Lundquist number can range from $\sim 10^2$ to $\sim 10^7$ in high-temperature laboratory plasmas, and it can exceed 10^{20} in astrophysical plasmas. Reconnection observed in weakly collisional, high Lundquist number plasmas is generally much faster than diffusive scaling would imply. This is true even if the classical collisional resistivity is replaced by a reasonable anomalous resistivity induced by turbulence [55].

An early mechanism for resistive reconnection faster than diffusion was proposed by Sweet and Parker [56]. They suggested that reconnection could occur between solar coronal loops, as sketched in Fig. 1-7 reproduced from Parker’s original paper. The Sweet-Parker model combines an assumption about the magnetic geometry with dimensional arguments to arrive at a reconnection rate faster than purely resistive diffusion. The reconnection rate, defined as the plasma inflow speed normalized to the upstream Alfvén speed, was found to scale as

$$V_{in} / V_{Alfven} = 1 / \sqrt{S}. \quad (1.5)$$

For high Lundquist number S plasmas, this is significantly faster than a purely diffusive $\propto 1/S$ process. For typical solar parameters, however, it is still several orders of magnitude too slow. The Sweet-Parker time for typical solar flares, for example, is on the order of months, whereas solar flares may release the majority of their energy in minutes. The geometry imposed by the model is illustrated in Fig. 1-7. The Sweet-Parker reconnection rate is limited by a bottleneck effect because the inflowing plasma is released as exhaust in a thin outflow channel. The Sweet-Parker current sheet is very narrow and elongated, with an aspect ratio that also scales as $\delta/L = V_{in} / V_{Alfven} = 1 / \sqrt{S}$. The Petschek model [57] attempts to overcome the geo-

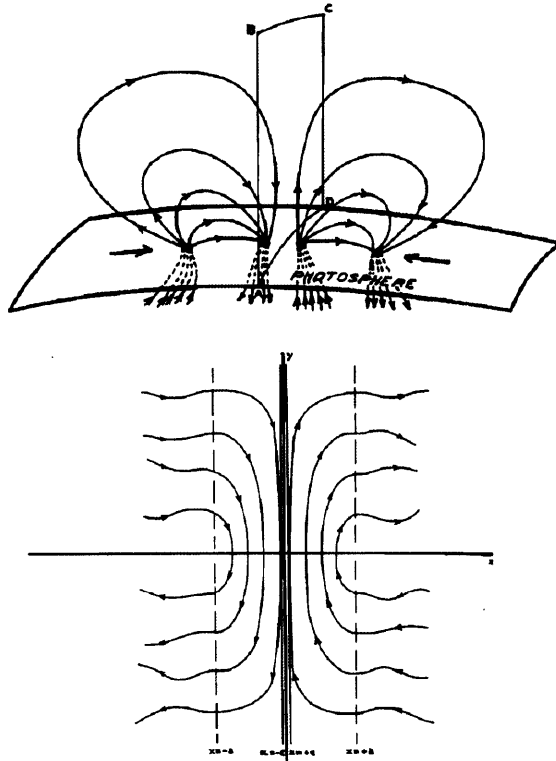


Figure 1-7: Parker's picture of Sweet's mechanism on the Sun [56].

metric constraints of the Sweet-Parker model, but as originally formulated it requires a somewhat delicate configuration of multiple slow mode shocks to accelerate the plasma.

Another influential contribution to reconnection theory within the resistive MHD framework was analytical work on tearing modes [58]. A tearing mode is an exact linear instability of a resistive plasma. Tearing modes release the stored global magnetic energy of the plasma configuration through a motion that would lead to singularities in the ideal case. Resistivity becomes dominant in a narrow boundary layer, while the external bulk plasma motion is nearly ideal. The parameter that characterizes stability is Δ' , which measures the curvature of the magnetic field perturbation as the difference in $(\tilde{B}_n)^{-1}(d\tilde{B}_n/dx)$ across the resistive boundary layer. Instability requires $\Delta' > 0$. This parameter depends on the boundary conditions, global plasma equilibrium, and especially on gradients in the current density. The reconnection rate

is limited by the small scales of the resistive layer in which magnetic diffusion may occur. Similar to the Sweet-Parker model, tearing modes grow on a hybrid time scale, with a growth rate $\gamma \propto S^{-3/5}$. Several of the results in the following chapters are based on reconnection in a thin current sheet with a strongly peaked current density profile, and the current density gradients act as the source of free energy. Although reconnection in those cases is not resistive, the parameter Δ' is made large because it remains a good measure of the free magnetic energy available to drive reconnection [59].

Moving beyond purely analytical results, numerical simulations have been able to study how reconnection evolves non-linearly. Early simulations were based on fluid models, and the results are somewhat limited by the scope of the modeling assumptions. These fluid simulations included models of the sawtooth oscillation in tokamaks [60]. Some results from these 2D resistive fluid simulations are plotted in the top of Fig. 1-8. The reduced fluid model found qualitative agreement with the Kadomtsev picture, but improved numerical models better resolved the discrepancies between simulation and experiment [61, 62]. For collisionless reconnection where inherently kinetic effects are important, particle-in-cell (PIC) codes are a useful tool for solving the full Vlasov-Maxwell system of equations. The PIC method is closer to a first-principles model, but it is computationally extremely demanding. Nevertheless, with present computing resources, it is now possible to study the evolution of reconnecting current sheets in 3D. An example of 3D PIC output from Ref. [63] is included in the bottom of Fig. 1-8. A broad comparative study of various simulation methods was undertaken by multiple groups in the Geospace Environmental Modeling (GEM) magnetic reconnection challenge [64]. These studied reconnection in a current sheet geometry applicable to Earth's magnetic tail. The general conclusions were that single-fluid, two-fluid, and kinetic codes found fast reconnection rates that were relatively insensitive to the dissipation mechanism and $V_{in}/V_{Alfven} \sim 0.1$. The resistive MHD codes, however, required a localized or current-dependent resistivity.

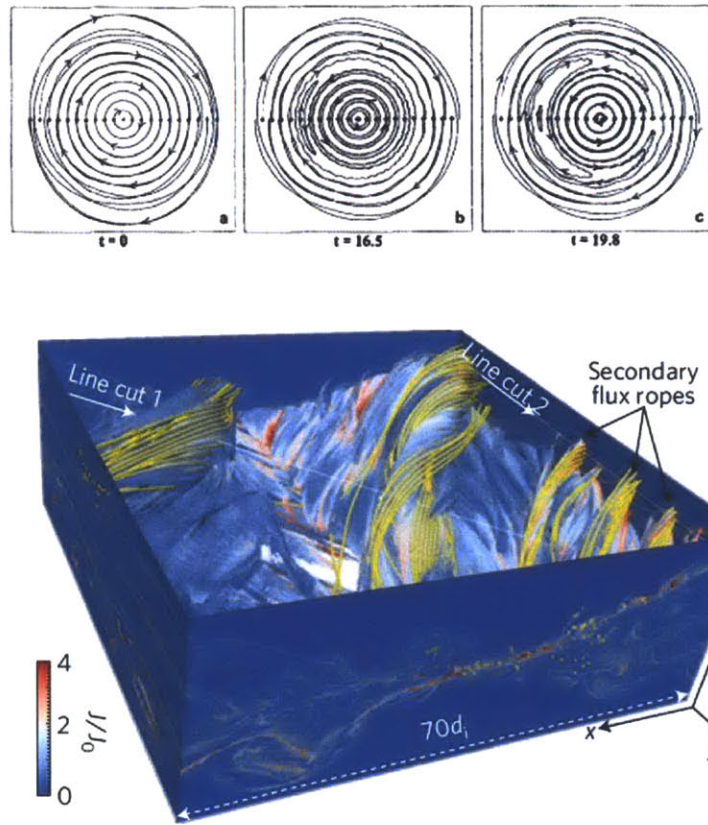


Figure 1-8: Top: An early fluid simulation of the $m = 1$ mode in a tokamak (Ref. [60]). Bottom: A recent fully-kinetic, three-dimensional simulation of a reconnecting current sheet (Ref. [63]).

Outline of the Following Chapters. Chapter 2 reviews derivations for the electron phase space density including the important effect of electron trapping, which plays a major role in modifying the electron anisotropy. This model is due to Egedal [65, 66]. The remaining chapters introduce the new results that constitute the core of this thesis. Equations of state based on the solution of the kinetic equation are derived in Chapter 3. The equations of state are then applied to an analysis of fully kinetic PIC simulations carried out on the code VPIC, provided by Daughton and other collaborators [67]. The simulations treat reconnection with a strong guide field (Chapter 4) and zero guide field (Chapter 5). Chapters 3-5 are based on papers by Le *et al.* [68-70]. Chapter 6 covers intermediate regimes, including an important new one that is observed in simulations that implement the true physical proton-to-electron mass ratio. These results have not yet been published elsewhere. Chapter 7 extends the application of the new equations of state to geometries beyond 2D Harris sheet reconnection. In particular, density asymmetries, 3D evolution, and island merging topologies are considered. The application of the equations of state to asymmetric geometries is detailed in a paper by Egedal, Le, *et al.* [71], and a manuscript on electron heating during island merging is under preparation by Le *et al.* Chapter 8 is a summary that emphasizes new results obtained during research for this thesis.

Appendices treat new analyses of (A) CGL temperature fluctuations induced by magnetic island merging and (B) the inclusion of collisions in PIC simulations of reconnecting current sheets, and Appendix C reviews some basic principles underlying the PIC simulation scheme.

Chapter 2

Electron Distributions

During collisionless reconnection, electron kinetic effects dominate in a localized diffusion region. The gradient length scales in this region typically fall below the ion inertial length $d_i = c/\omega_{pi}$, roughly the smallest scale at which the MHD formulation is valid. On these scales, electron and ion dynamics decouple. A hallmark of the electron diffusion region is anisotropy of the electron phase space distribution, which usually becomes highly elongated in the velocity direction parallel to the magnetic field. This chapter reviews a model that accounts for the main anisotropy of the electron distribution. A principal contribution to the anisotropy comes from an electric field parallel to the magnetic field. The parallel electric field E_{\parallel} creates an effective potential that traps most thermal electron guiding centers. This is accounted for in an approximate analytical solution of the Vlasov equation, which was originally derived to describe Wind spacecraft measurements and was motivated by analysis of experiments on the VTF device [65, 72].

Because the distribution serves as a foundation for the equations of state of the following chapters, two different derivations will be presented. The first makes use of an analogy with 1D dynamics and emphasizes the general phenomenon of adiabatic particle trapping as applied to solutions of the kinetic equation (see, e.g., Ref. [73]). The second begins with a generic reconnection geometry and describes how the populations of trapped and passing electrons fill out the particle phase space. This is the picture presented in Ref. [66], and it shows more concretely how the processes of

electron acceleration and trapping occur during reconnection.

The framework relies on a few assumptions about the time and length scales. These assumptions are often well-satisfied for electrons during reconnection. First, the magnetic field is assumed to be sufficiently strong to validate the guiding-center approximation. This implies the results will hold when there is a strong guide magnetic field and away from the neutral sheet in anti-parallel reconnection. The guiding center approximation requires gradient scales to be smaller than the particle Larmor radius and time variation to be slower than the cyclotron frequency. In the context of reconnecting current sheets, the most stringent requirement is usually that $\kappa \gg 1$, where the parameter κ is defined in Ref. [74] as

$$\kappa^2 = R_{min}/\rho_{e,max} \quad , \quad (2.1)$$

for a minimum magnetic field line radius of the curvature R_{min} and a maximum electron gyroradius $\rho_{e,max}$. When the condition $\kappa \gg 1$ is met, the perpendicular energy is determined by the conservation of the first adiabatic invariant $\mu = mv_{\perp}^2/2B$.

It is the parallel motion that requires a more careful treatment and is more sensitive to the details of the reconnection process. The parallel motion of a single electron follows from an effective Hamiltonian [75, 76]

$$H_{\parallel} = \frac{1}{2}mv_{\parallel}^2 + \mu B + \Phi, \quad (2.2)$$

where Φ is a potential. Because the parallel motion follows from an effective 1D Hamiltonian, it is completely analogous to 1D particle motion. The 1D case will be presented first because it is relatively simple and it highlights the physics of adiabatic particle trapping in a kinetic equation. A second demonstration of the mechanism will focus on a more concrete reconnection geometry.

The essential complication is that electrons become trapped by a time-varying effective potential. Trapping here means that the particle parallel velocity v_{\parallel} reverses sign at bounce points. Magnetic trapping results from the usual mirror force associated with the conservation of μ in the presence of magnetic field gradients. More

importantly, substantial trapping occurs due to the magnetic field-aligned electric field E_{\parallel} . This is parametrized by the parallel potential of Eq. 1.2 reproduced below:

$$\Phi_{\parallel}(\mathbf{x}) = \int_{\mathbf{x}}^{\infty} \mathbf{E} \cdot d\mathbf{l}. \quad (2.3)$$

Again, the integral is taken along the instantaneous magnetic field lines from a point inside the reconnection region to the ambient ideal plasma where $\mathbf{E} \cdot \mathbf{B} = 0$. The effective potential Φ_{\parallel} contains contributions from inductive electric fields for which $\nabla \times \mathbf{E} \neq 0$, and it should not be confused with the ordinary electrostatic potential. Physically, $e\Phi_{\parallel}$ measures the work done by the electric field on electrons that exit or enter the reconnection region in a single shot along a magnetic field line. The parallel potential Φ_{\parallel} seen by the electrons is time-varying, both due to explicit time dependence of the electromagnetic fields and because electrons will sample different spatial regions as they convect with field lines through a reconnecting current sheet.

In general, the motion of a particle in a time-varying potential is not integrable, and the trajectory can only be determined numerically. For applications to reconnection, however, the time variation is in practice slow compared to an electron transit time. The adiabatic approximation is therefore often applicable for the parallel motion as well as the perpendicular motion. Under conditions typical of reconnection, the requirement for applicability of the adiabatic approximation for the parallel motion is that the electron thermal speed be greater than the Alfvén speed, $v_{the} > v_{Alfvén}$. In this case, the parallel motion is also determined by an adiabatic invariant [77],

$$J_{\parallel} = \oint m v_{\parallel} dl, \quad (2.4)$$

where the integral follows a trapped particle guiding center along the magnetic field between consecutive bounces. Assuming the adiabatic limit for trapped electrons allows a general approximate solution of the Vlasov equation.

To begin, consider particle trapping in a one-dimensional, time-dependent potential well of depth $U(x, t)$, such as the generic potential $-U(x)$ at a time t plotted in Fig. 2-1. This theory is concisely outlined in Ref. [73] and is perfectly analogous to

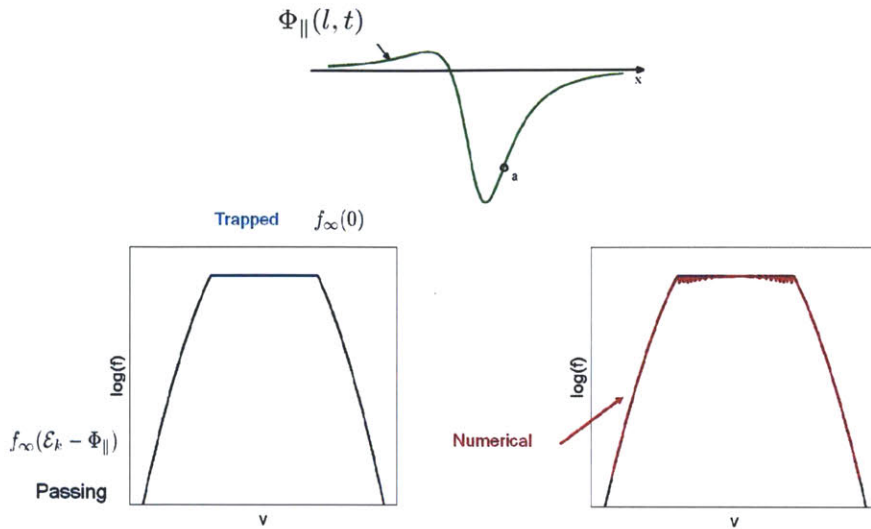


Figure 2-1: One-dimensional distribution function for particles trapped in a potential that varies slowly in time.

electron guiding center parallel trapping in the adiabatic limit. The characteristics of the Vlasov equation,

$$\left(\frac{\partial}{\partial t} + v \frac{\partial}{\partial x} + \frac{1}{m} \frac{\partial U}{\partial x} \frac{\partial}{\partial v}\right) f(t, x, v) = 0, \quad (2.5)$$

are particle orbits in the potential $-U(t, x)$. Assume for simplicity that the initial distribution depends only on kinetic energy, $f_\infty(\mathcal{E})$. Then the distribution function at a time t is given by $f(x, v) = f_\infty(\mathcal{E}_\infty)$, where $\mathcal{E}_\infty(x, v)$ is the initial energy of a particle that arrives at the point x with velocity v at time t . Assume also the potential develops on a time scale slow compared to the bounce or transit frequency of thermal particles across the well, so that the adiabatic approximation applies. The initial energy of a particle \mathcal{E}_∞ then does not depend on the details of the time-evolution or spatial structure of the potential well, and the Vlasov equation admits a relatively simple solution.

Two classes of particles are treated separately. Passing particles have sufficient energy to escape from the potential well. In the adiabatic limit, their motion is not affected by the time variation of the potential. Because the transit time of a passing

particle is so short, the potential may be treated as effectively static. Therefore, passing particles gain a fixed energy U while in the potential well, and $\mathcal{E}_\infty = \mathcal{E} - U$. Trapped particles, on the other hand, have motion determined by the adiabatic invariance of J_\parallel . Consider the case where the potential is initially absent, and it then grows slowly. Just as the potential begins to develop, the well is extremely shallow. Only particles with very low energy will therefore be trapped. In the limiting case where the potential varies very slowly, the trapped particles must have initially been very nearly at rest with zero kinetic energy. Based on this consideration, the trapped portion of the distribution will be flat and have a value of $f_\infty(0)$, corresponding to the fact that trapped particles must have all initially had negligible energy ($\mathcal{E}_\infty = 0$). The distribution thus takes the form:

$$f(x, v) = \begin{cases} f_\infty(\mathcal{E} - U) & , \quad \mathcal{E} - U > 0 \text{ (passing)} \\ f_\infty(0) & , \quad \mathcal{E} - U < 0 \text{ (trapped)} \end{cases} \quad (2.6)$$

To verify the analytical expression of Eq. 2.6, the distribution of particles in the generic well illustrated in Fig. 2-1 is evaluated by numerically computing a large sample of particle orbits. The initial distribution $f_\infty(\mathcal{E})$ is taken as Maxwellian for this specific example. The theoretical distribution function and the numerically computed one are plotted in Fig. 2-1. Following Eq. 2.6, the distribution is flat up to the trapped-passing boundary, which corresponds to a particle kinetic energy equal to U . It then falls off as a Maxwellian shifted by the energy U . The oscillations in the numerically computed distribution result from the finite bounce frequency of the trapped particles, and the deviations from the adiabatic solution become smaller as the time variation of the potential gets slower.

Analogous electron trapping occurs during collisionless reconnection for the electron motion parallel to the magnetic field. A generic reconnection geometry near an X line is illustrated in Fig. 2-2. The reconnection region is assumed to be embedded in an ambient plasma with fairly uniform density and magnetic field strength. Assuming in addition that the electron distribution in the ambient plasma is isotropic in velocity

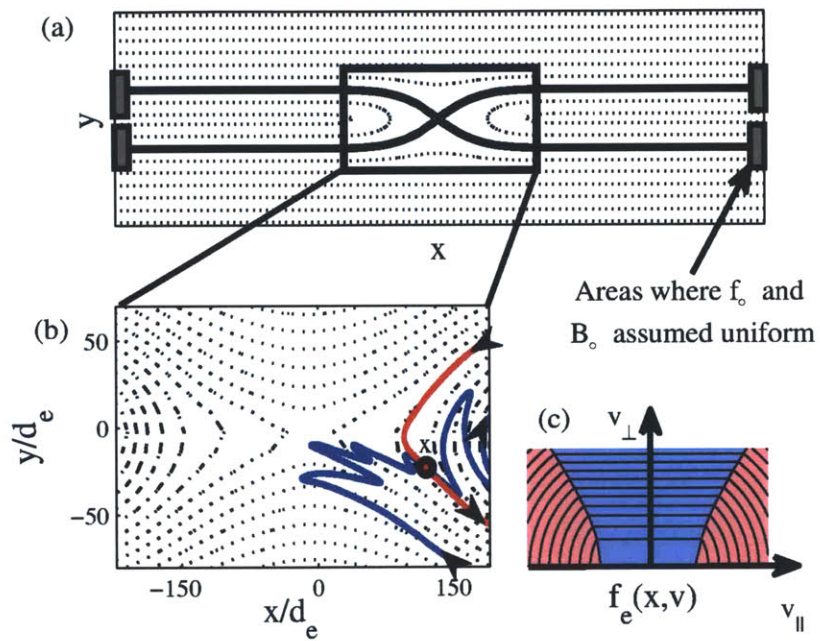


Figure 2-2: Reconnection geometry with typical passing (red) and trapped (blue) electron orbits and the phase space density f_e .

space, so that $f_\infty = f_\infty(\mathcal{E})$, it is only necessary to track changes in an electron's energy as it moves through the reconnection region. The phase-space density at a point near the X line will then be $f(x, v) = f_\infty(\mathcal{E}_\infty)$, where \mathcal{E}_∞ is the initial total kinetic energy an electron in the ambient plasma before it reaches the point x with velocity v . Assuming the electrons are magnetized, the magnetic moment $\mu = mv_\perp^2/(2B)$ is conserved and an electron's perpendicular energy decreases proportionally to B as it approaches the diffusion region. The electrons gain energy from the parallel electric field, the direction of which tends to accelerate electrons towards the reconnection region [78].

As in the 1D case, trapped and passing electrons must be treated separately. A typical passing orbit is illustrated in red in Fig. 2-2(b). It enters and exits the reconnection region essentially along a single magnetic field line in a single pass. A typical trapped electron orbit [like the blue one in Fig. 2-2(b)], on the other hand, repeatedly bounces in its parallel motion along the field line and v_\parallel changes signs. The passing electrons convect into the reconnection region with the field lines as reconnection proceeds and draws magnetic flux in from the top and bottom of the figure and out from the X line along the sides.

To illustrate how the trapped and passing electrons fill out phase space, a flux tube is highlighted in Fig. 2-3. This flux tube contains three electron populations: two populations of passing electrons that enter the reconnection from the left and the right in a single shot along the magnetic field lines, and the trapped electrons that convect into the region with the magnetic field lines as they reconnect. The energy gain of a passing electron moving along single field line into the region is given by the acceleration potential and is $e\Phi_\parallel$. The trapped electrons, meanwhile, are characterized by the fact that they initially have negligible parallel energy. The following form of the electron distribution function results:

$$f(\mathbf{x}, \mathbf{v}) = \begin{cases} f_\infty(\mathcal{E} - e\Phi_\parallel) & , \text{ passing} \\ f_\infty(\mu B_\infty) & , \text{ trapped} \end{cases} \quad (2.7)$$

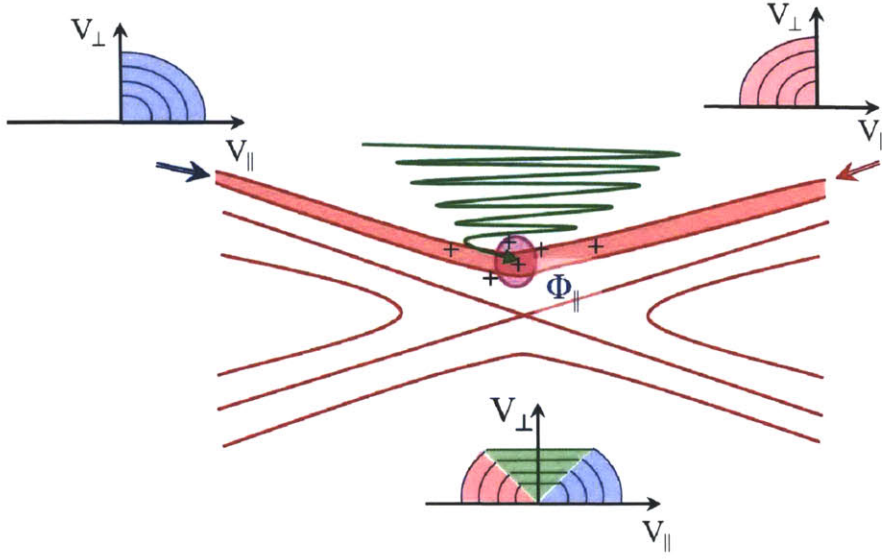


Figure 2-3: Trapped and passing particles in a flux tube populate different regions of velocity space.

The trapped-passing boundary is given by

$$\mathcal{E} - e\Phi_{\parallel} - \mu B_{\infty} = 0 \quad , \quad (2.8)$$

which expresses the physical condition that marginally trapped electrons deplete their parallel energy ($\mathcal{E}_{\parallel\infty} \sim 0$) as they barely escape along the flux tube away from the reconnection region. The parallel energy is lost to both the magnetic mirror force and the electric force along a magnetic field line. In this model, the passing particles exhibit a Boltzmann-like response to the potential Φ_{\parallel} .

Contours of f from Eq. 2.7 are plotted in Fig. 2-2, where the trapped (blue) and passing (red) contributions are color-coded. The asymptotic opening angle of the trapped region in velocity space grows wider as the magnetic field strength decreases compared to the upstream value. The passing region is similar to the standard loss cone in a magnetic mirror, and the angle is

$$\cot(\theta) = \frac{v_{\parallel}}{v_{\perp}} = \sqrt{1 - B/B_{\infty}}. \quad (2.9)$$

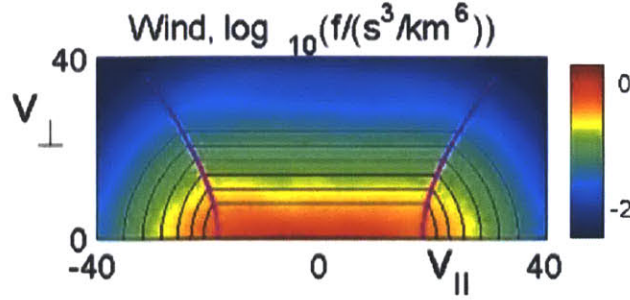


Figure 2-4: Electron distribution observed by Wind during reconnection.

As the parallel potential Φ_{\parallel} varies, the distribution also becomes more elongated in the parallel direction, reflecting the heating and acceleration due to the parallel electric field. The trapped-passing boundary intersects the v_{\parallel} -axis where

$$|v_{\parallel}| = \sqrt{\frac{2e\Phi_{\parallel}}{m}}. \quad (2.10)$$

The value of the parallel potential may be inferred from observed electron distributions. For example, the theoretical form for f was originally derived to account for the anisotropy observed in the electron distribution during reconnection by the Wind spacecraft [65, 66]. An example electron distribution observed during magnetotail reconnection is depicted in Fig. 2-4. The theoretically predicted contours of the phase space density are overlaid in black. They are based on an inferred parallel potential of $\sim 1kV$. The elongation is consistent with this value, and the corresponding trapped-passing boundary is given by the magenta lines.

Summary. This chapter reviewed previous results mainly by Egedal. An adiabatic solution of the Vlasov equation describes the main anisotropy of the electrons during magnetic reconnection. The central feature is the trapping of electrons due to the magnetic mirror force and, more importantly, a parallel potential Φ_{\parallel} . Electron distributions measured by spacecraft during magnetospheric reconnection agree with the theoretical model.

Chapter 3

The Equations of State

In order to understand how the electron anisotropy feeds back on the structure of the diffusion region, it is helpful to incorporate the anisotropy into a fluid model. Corresponding to the elongation of the particle distribution described in the previous chapter, the electron pressure tensor \mathbb{P} develops strong anisotropy. In particular, the parallel pressure component $p_{\parallel} = \mathbf{B} \cdot \mathbb{P} \cdot \mathbf{B} / |\mathbf{B}|^2$ often becomes many times larger than the perpendicular components. A fluid closure based on the solution of the Vlasov equation is derived here. The fluid model yields equations of state for the parallel and perpendicular electron pressure components that depend only on the plasma density and magnetic field strength.

Obtaining a fluid closure for a plasma generally requires assumptions about the plasma parameters and the relevant time and length scales. In the collisional regime, where particle mean free paths are shorter than gradient length scales, the Braginskii closure may be appropriate [79]. The Braginskii equations form a closed set of fluid evolution equations, but they rely fundamentally on the short mean free path assumption. Collisions tend to drive the particle distribution towards a Maxwellian in velocity space and to smooth out velocity space gradients. The main concern of this thesis is collisionless plasmas, where the mean free path is formally infinite. The collisionless regime is relevant especially to high-temperature, low-density plasmas found naturally in space. Discrete binary particle interactions become less important as the number of particles per Debye volume becomes larger, which scales as

$n\lambda_D^3 \propto T_e^{3/2}/n^{1/2}$. In laboratory fusion experiments $n\lambda_D^3$ is typically $\sim 10^7 - 10^9$, while in space plasmas it can greatly exceed 10^{10} .

An accurate fluid description based on equations of state does not exist in general, but rather it depends on additional constraints on the dynamics. One method of obtaining a fluid closure in the collisionless regime is to extend linear theoretical results [80]. The main advantage of this method is to capture, at least qualitatively, Landau damping and other inherently kinetic plasma effects. While this approach leads to a consistent model, it cannot correctly capture strongly non-linear evolution. Another pair of equations of state for a collisionless plasma were derived by Chew, Goldberger, and Low [81]. One assumption of that model is that the magnetic field is strong, so that a formal expansion in $1/\omega_{ci}$ is justifiable, where ω_{ci} is the ion cyclotron frequency. More crucially, the CGL model closes the fluid equations by assuming that there is no parallel heat conduction, an assumption that is not typically justified. The CGL equations of state give the parallel and perpendicular pressure components of the plasma pressure tensor in terms of the density and the magnetic field strength. They take the form

$$\frac{d}{dt} \left(\frac{p_{\parallel} B^2}{n^3} \right) = 0 \quad (3.1)$$

$$\frac{d}{dt} \left(\frac{p_{\perp}}{nB} \right) = 0 \quad (3.2)$$

As described below, the equations of state derived in this thesis for the electron pressure approach the CGL scaling in the deeply-trapped limit where most electrons follow trapped orbits.

From a solution for the particle phase-space density, any fluid quantity may be found. For the slightly simpler 1D case of particles adiabatically trapped in a well of depth U , the lowest order even moments of the distribution f of Eq. 2.6 for the density and pressure are

$$\tilde{n}(x, v) = \frac{1}{n_{\infty}} \int f dv = e^{\tilde{U}} \Psi(\tilde{U}^{1/2}) + \frac{2}{\sqrt{\pi}} \tilde{U}^{1/2} \quad (3.3)$$

$$\tilde{p}(x, v) = \frac{1}{n_\infty T_\infty} \int m v^2 f(x, v) dv = e^{\tilde{U}} \Psi(\tilde{U}^{1/2}) + \frac{2}{\sqrt{\pi}} \tilde{U}^{1/2} + \frac{4}{3\sqrt{\pi}} \tilde{U}^{3/2} \quad (3.4)$$

where $\tilde{U} = U/T$, $\tilde{n} = n/n_\infty$, $\tilde{p} = p/n_\infty T_\infty$ and $\Psi(\zeta)$ is the complementary error function,

$$\Psi(\zeta) = \frac{2}{\sqrt{\pi}} \int_\zeta^\infty e^{-z^2} dz. \quad (3.5)$$

The functions $n(U)$ and $p(U)$ are plotted in Fig. 3-1. It is worth noting also that the density and pressure are consistent with steady-state fluid momentum balance, and they exactly satisfy the relation

$$0 = -\frac{\partial p}{\partial x} + n \frac{\partial U}{\partial x}. \quad (3.6)$$

In a collisional plasma where the velocity space distribution relaxes to a Maxwellian, both the density and pressure would scale as $\exp(\tilde{U})$. For collisionless adiabatic trapping, on the other hand, the density asymptotically scales as $n \propto U^{1/2}$, which is a far weaker dependence. One result is that very large potentials U are required to build up the particle density. This will explain why, in the following treatment of reconnection geometries, much larger parallel electric fields and parallel potentials develop in collisionless plasmas than previously thought possible.

The density and pressure thus depend only on the local value of the potential $-U$. It often proves useful to eliminate the potential $-U$ and work only with the fluid quantities n and p . Each relationship is one-to-one and, in particular, a given value of U corresponds to a unique density n . The pressure is therefore implicitly a function only of the density, $p = p(n)$. The inversion $n(U) \Rightarrow U(n)$ used to eliminate the potential $-U$ in favor of the density n cannot be performed analytically, but the relation is readily inverted numerically. The final relationship $p(n)$ is plotted in Fig. 2-1, and it is the desired equation of state in the one-dimensional case.

The qualitative dependence of the pressure on density may be understood as

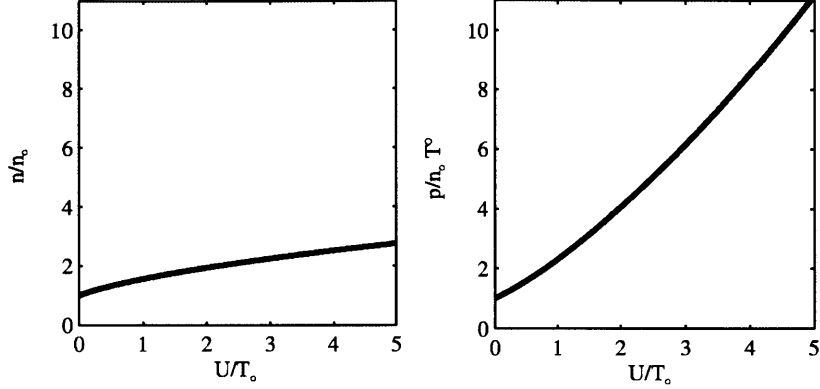


Figure 3-1: One-dimensional pressure p and density n as functions of potential U .

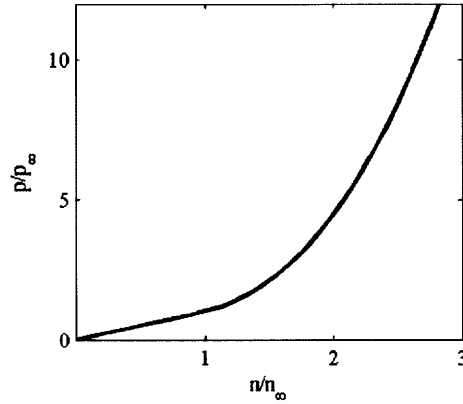


Figure 3-2: One-dimensional equation of state: pressure p as a function of density n .

follows. When U is negative (a potential hill), there are no trapped particles and the equation of state becomes the usual isothermal one: $p = nT_\infty$. The fast passing particles effectively transport heat, and there can be no gradients in the temperatures. In the other extreme, for a large U that traps a significant fraction of the particles, $p(n)$ approaches up to a multiplicative factor the adiabatic equation of state for a one-dimensional gas: $p/p_\infty \approx \pi/6 \times (n/n_\infty)^3$. This adiabatic equation of state (where adiabatic here means that there is negligible heat flux) is reached because the trapping of particles effectively limits their ability to transport thermal energy. Essentially the same limits hold for the parallel electron pressure in the guiding center approximation.

Following methods similar to the 1D case, moments of the guiding center distribution of Eq. 2.7 may be used to yield equations of state. For the guiding center motion, the perpendicular energy is tied to conservation of the adiabatic invariant $\mu = mv_{\perp}^2/2B$, while parallel motion is affected by the magnetic mirror force and the parallel potential Φ_{\parallel} . Because the electron pressure is assumed to be symmetric around the magnetic field direction to a good approximation, the electron pressure tensor has only two independent components. If $\hat{\mathbf{b}} = \mathbf{B}/B$ is the unit vector in the direction of the magnetic field, the electron pressure tensor is $\mathbb{P} = p_{\perp}\mathbb{I} + (p_{\parallel} - p_{\perp})\hat{\mathbf{b}}\hat{\mathbf{b}}$. In a reference frame with the first axis aligned with the magnetic field, it takes the form

$$[\mathbb{P}] = \begin{pmatrix} p_{\parallel} & 0 & 0 \\ 0 & p_{\perp} & 0 \\ 0 & 0 & p_{\perp} \end{pmatrix}, \quad (3.7)$$

where

$$p_{\parallel} = \int m_e v_{\parallel}^2 f d^3v \quad (3.8)$$

$$p_{\perp} = \int \frac{m_e}{2} v_{\perp}^2 f d^3v. \quad (3.9)$$

Besides the distribution f_{∞} in the ambient plasma, the expression for f in Eq. 2.7 depends only on B and Φ_{\parallel} . Its moments are therefore also functions of these two quantities. For example, assuming a Maxwellian ambient plasma with temperature T_{∞} and density n_{∞} , the density moment of Eq. 2.7 is explicitly given by

$$\frac{n}{n_{\infty}} = \frac{2}{\sqrt{\pi}}(1-b)\sqrt{u} + e^u\Psi(\sqrt{u}) - b^{\frac{3}{2}}e^{u/b}\Psi\left(\sqrt{\frac{u}{b}}\right) \quad (3.10)$$

for $u \equiv e\Phi_{\parallel}/T_{\infty} > 0$ and $b \equiv 1 - B/B_{\infty} > 0$, and Ψ is again the complementary error function. Likewise, the two pressure moments p_{\parallel} and p_{\perp} are functions of only the local values of Φ_{\parallel} and B .

Similar to the 1D example, the relationship between n and Φ_{\parallel} can be inverted, at least numerically. This yields Φ_{\parallel} as a well-defined implicit function of n and B . The function $\Phi_{\parallel}(n, B)$ then serves to eliminate Φ_{\parallel} numerically in favor of the

more convenient variable n . The result of re-expressing the parallel pressure p_{\parallel} and perpendicular pressure p_{\perp} in terms of the density is a pair of equations of state. Schematically, the procedure is to make the following inversions and substitutions:

$$n(\Phi_{\parallel}, B) \rightarrow \Phi_{\parallel}(n, B) \quad (3.11)$$

$$p_{\parallel}(\Phi_{\parallel}, B) = p_{\parallel}(\Phi_{\parallel}(n, B), B) \rightarrow p_{\parallel}(n, B) \quad (3.12)$$

$$p_{\perp}(\Phi_{\parallel}, B) = p_{\perp}(\Phi_{\parallel}(n, B), B) \rightarrow p_{\perp}(n, B) \quad (3.13)$$

The end result is a pair of CGL-like [81] equations of state that give p_{\parallel} and p_{\perp} of the electrons as functions only of the local plasma density n and magnetic field strength B [68].

The qualitative aspects of the new equations of state are similar to the 1D case. For few or no trapped particles at low densities, the equations of state approach the isothermal approximation $p = nT$, which is the equation of state for infinite heat conductivity. This reflects the fact that passing electrons rapidly transport heat along the field lines. Meanwhile in the deeply trapped regime at higher densities, the equations of state approach the CGL scalings $p_{\parallel} \propto n^3/B^2$ and $p_{\perp} \propto nB$. The CGL equations of state assume zero heat conductivity, and this limit is approached in the new equations of state because trapped electrons do not move freely along the field lines. Fig. 3-3 illustrates how the equations of state interpolate smoothly between these two regimes.

Weakly collisional plasmas are generally excellent electrical conductors along the magnetic field owing to the high mobility of the electrons. Therefore, although field-aligned potentials are a generic feature of magnetic reconnection [47], it is surprising from a theoretical perspective that parallel electric fields can accelerate electrons to high energies. It follows from the model presented that the parallel electric field is balanced by gradients in the electron pressure. Associated with the elongated phase

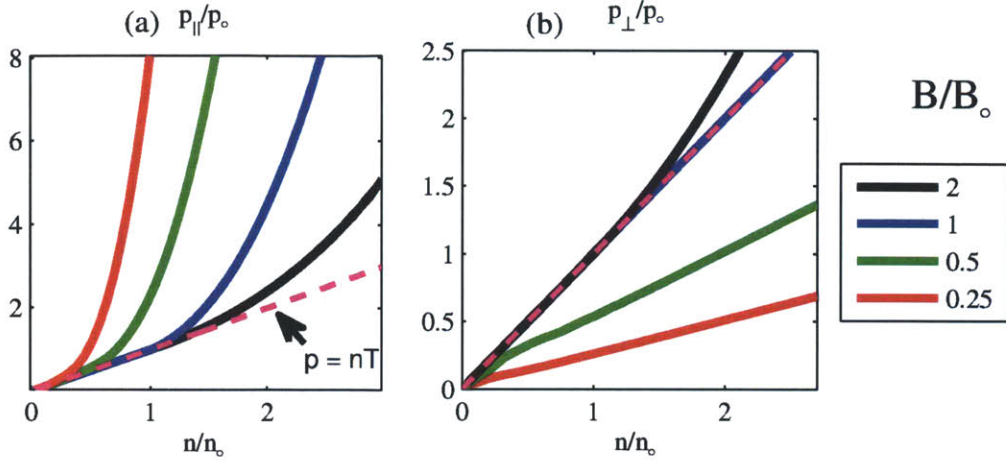


Figure 3-3: The equations of state.

space distributions, the electron pressure becomes highly anisotropic, generally with the parallel pressure $p_{||}$ several times larger than the perpendicular pressure p_{\perp} .

The substantial pressure anisotropy, which results from the combined effects of $E_{||}$ and the gradients in B , alters the electron momentum equation and the resulting generalized parallel Ohm's law. Within the model, the parallel electric field $E_{||}$ is balanced by the electron pressure tensor \mathbb{P} :

$$-neE_{||} = -\nabla \cdot \mathbb{P} = -\nabla_{||} p_{||} + (p_{||} - p_{\perp}) \nabla_{||} \ln B \quad (3.14)$$

where $\nabla_{||} = (\mathbf{B}/B) \cdot \nabla$. The strong density dependence of the trapped electron pressure, $p_{||} \propto n^3/B^2$, allows significant parallel electric fields to develop: for a doubling of the density and a magnetic field strength reduced to half its boundary value, there is roughly a factor of twenty-four enhancement in $dp_{||}/dn$ over the isothermal or adiabatic approximations that are used extensively in other fluid models [62, 82, 83]. Furthermore, the pressure anisotropy provides an additional contribution.

The dependence of the pressure components $p_{||}$ and p_{\perp} on the density is plotted in Fig. 3-3 for a few values of the magnetic field. Note that for $B/B_{\infty} = 1$ the parallel

pressure curve $p_{\parallel}(n, B = B_{\infty})$ is identical to the one-dimensional pressure curve $p(n)$ of Fig. 3-2. Most thermal particles are passing when Φ_{\parallel} is small or negative and $B/B_{\infty} \sim 1$, and the perpendicular and parallel pressures both approach isothermal forms, $p_{\parallel} = p_{\perp} = nT_{\infty}$. In the opposite limit when a large fraction of particles are trapped (large Φ_{\parallel} and $B/B_{\infty} < 1$), the equations of state approach CGL-like double-adiabatic scalings. This is evident in the following approximate form of the equations of state assuming a Maxwellian f_{∞} (given as Eq. 4 of Ref. [68]):

$$\begin{aligned}\tilde{p}_{\parallel} &= F(\alpha/2) \times \tilde{n} + F(\alpha^{-1}/2) \times \frac{\pi \tilde{n}^3}{6\tilde{B}^2} \quad , \\ \tilde{p}_{\perp} &= F(\alpha) \times \tilde{n} + F(\alpha^{-1}) \times \tilde{n}\tilde{B} \quad ,\end{aligned}\tag{3.15}$$

where $\tilde{n} = n/n_{\infty}$, $\tilde{B} = B/B_{\infty}$, $\tilde{p}_{\parallel} = p_{\parallel}/p_{\infty}$, $\tilde{p}_{\perp} = p_{\perp}/p_{\infty}$, $\alpha = \tilde{n}^3/\tilde{B}^2$, and $F(x) = (1+x)^{-1}$. In the following chapters, the equations of state serve as basis for studying the electron diffusion region in magnetic reconnection with and without a guide magnetic field in both open and closed field line topologies.

Summary. Originally published by Le *et al.* in Ref. [68], new equations of state based on the solution for the electron phase-space density are described. The equations of state interpolate between an isothermal condition when there are no trapped electrons to CGL-like scalings when most electrons are trapped. Due to the strong density dependence of the parallel pressure $p_{\parallel} \propto n^3$, strong electron pressure anisotropy is expected to develop during magnetic reconnection with $p_{\parallel} > p_{\perp}$.

Chapter 4

Strong Guide Field Regime

A guide magnetic field is a component of magnetic field out of the reconnection plane. If there is a sufficiently strong guide field, the equations of state derived in the previous chapter describe the electron pressure tensor throughout the reconnection region. It should be pointed out, however, that gyrophase-dependent terms that fall outside the scope of the theory are observed in kinetic simulations in a small region measuring a few d_e across directly near the X line. These terms are typically important for breaking the frozen-in condition [84].

Details of how the equations of state operate in the strong guide field regime are discussed in this chapter. First, it is found that the parallel potential Φ_{\parallel} develops to control the electron density and maintain quasi-neutrality. Due to electron heating in the parallel electric field that produces Φ_{\parallel} , the electron pressure then becomes anisotropic following the equations of state. The parallel electron pressure often becomes several times greater than the perpendicular pressure. Finally, the electron flows required by the model are found, including electron currents induced by the strongly anisotropic pressure.

To verify the theoretical predictions, fully kinetic particle-in-cell (PIC) simulations were carried out on the VPIC code by Daughton at Los Alamos [67]. PIC codes allow a numerical solution of the equations of motion for a collisionless plasma. VPIC solves the relativistic electromagnetic Vlasov-Maxwell system of equations with relatively few *ad hoc* modeling assumptions. Some details of the numerical methods are

described in Appendix C. All of the kinetic simulation data presented in this thesis were provided by Daughton or his collaborators, and the simulations were all carried out using the VPIC code. The code was run on several different machines, including Roadrunner at Los Alamos, Jaguar at Oak Ridge, NASA's Pleiades, and Kraken at NICS.

The initial conditions of the simulations presented in this chapter contain a Harris sheet [85]. This is an exact Vlasov-Maxwell equilibrium, and it also served as the basis for the simulations performed during the GEM challenge [64]. The Harris configuration depends on only a single spatial coordinate, and both the electron and ion velocity space distributions are drifting Maxwellians. The original Harris sheet consists of a magnetic field that reverses direction 180° due to current in the plasma layer. In the frame where $\mathbf{E} = 0$, which is where the electron and ion drift speeds are equal in magnitude and opposite in direction when $T_e = T_i$, the magnetic field and density are given by

$$\begin{aligned}
 B_x &= B_0 \tanh(z/\lambda) \\
 B_y &= B_g \\
 B_z &= 0 \\
 n &= \frac{n_0}{\cosh^2(z/\lambda)} + n_b,
 \end{aligned}
 \tag{4.1}$$

where n_b is a uniform background density, B_g is a uniform out-of-plane guide field, and the scale length λ is typically taken around the order of an ion inertial length d_i so that reconnection will be in the kinetic regime. Thin sheets tend to be more unstable because the tearing mode Δ' parameter from the Introduction is larger. The addition of the background guide field B_g will mean that magnetic field shears through an angle less than 180° , unlike in the original Harris formulation.

The simulation is translationally symmetric in the z -direction and has a total domain of 3072×3072 cells $= 569d_e \times 569d_e$, where $d_e = c/\omega_{pe}$ is the electron inertial skin depth. The initial Harris sheet is characterized by the following parameters: $m_i/m_e = 360$, $T_i/T_e = 2$, $B_g = 0.5B_0$, $\omega_{pe}/\omega_{ce} = 2$, background density $= 0.3n_0$ (peak

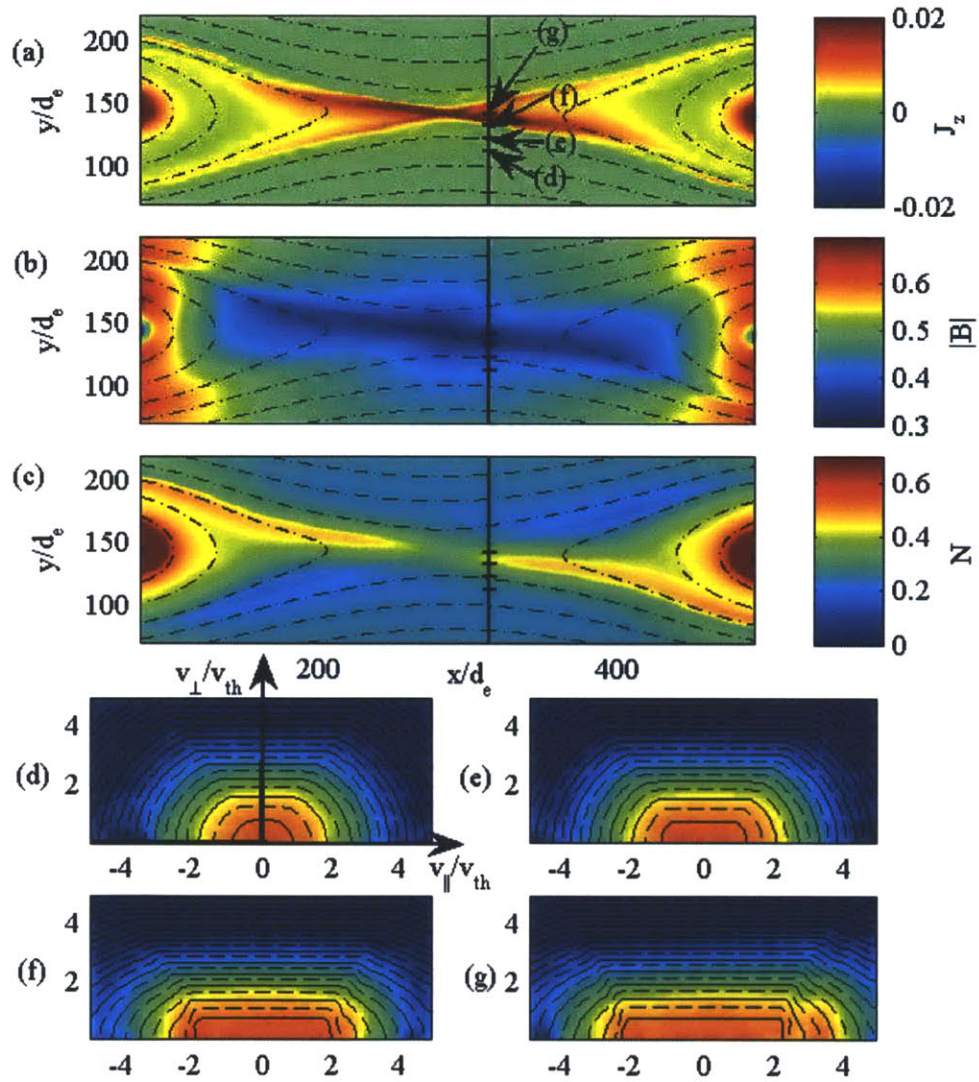


Figure 4-1: Profiles from a PIC simulation of reconnection with a strong guide field along with sample particle distributions.

Harris density), and $v_{th,e}/c = 0.2$. The code uses open boundary conditions for the particles and fields [67]. Magnetic reconnection with a single X line evolves from a small initial perturbation. The data presented are from a time-slice with quasi-steady reconnection when the fields are evolving slowly. The out-of-plane current density J_z , the plasma density n , and the magnetic field strength B from this time-slice are plotted in Fig. 4-1(a-c).

The parallel electric field E_{\parallel} is usually small in a plasma, and the parallel component of the electric field in the simulations is roughly an order of magnitude weaker than the perpendicular component. Even so, when integrated over the ion-scale lengths of the density structures, E_{\parallel} forms an parallel potential Φ_{\parallel} (Fig. 4-2) that reaches nearly $\Phi_{\parallel} \sim (4 - 5)T_e/e$. This implies that the majority of thermal electrons follow trapped orbits. The PIC code tracks roughly 2×10^9 electrons, allowing the full electron phase-space distribution to be reconstructed. Except in a small region directly around the X-line, the distribution is gyrotropic to within $\sim 5\%$. In Fig. 4-1(d-g), the gyro-averaged distributions are plotted as functions of v_{\parallel} and v_{\perp} at the four points marked in Fig. 4-1(a). The distributions become increasingly anisotropic as the region of large Φ_{\parallel} is approached. This broadening of the electron distribution in the parallel direction is well-described by the model and follows closely the predicted dependence on the local values of Φ_{\parallel} and B .

Comparison with the superimposed level lines of the analytic solution for $f(n, B)$ of Eq. 2.7 shows that the model correctly predicts the broadening and flattening of the distribution. Note that while the model for f assumes the current sheet is embedded in a uniform ambient plasma, computational constraints limit the size of the region that can be simulated. Therefore, while the original model in Ref. [66] used a uniform f_{∞} far from the X-line (in the shaded boxes in Fig. 2-2(a)), the PIC code allows f at the edges of the simulation box to vary in order to eliminate gradients in the density, flow, and pressure tensor at the boundary. To approximate the PIC code's boundary values for f , f_{∞} is taken as a Maxwellian in the inflow region and, for passing electrons that originate in the outflow region, f_{∞} a bi-Maxwellian with $n = 0.33n_0$ and $T_{\parallel} = 2T_{\perp} = 2T_e$.

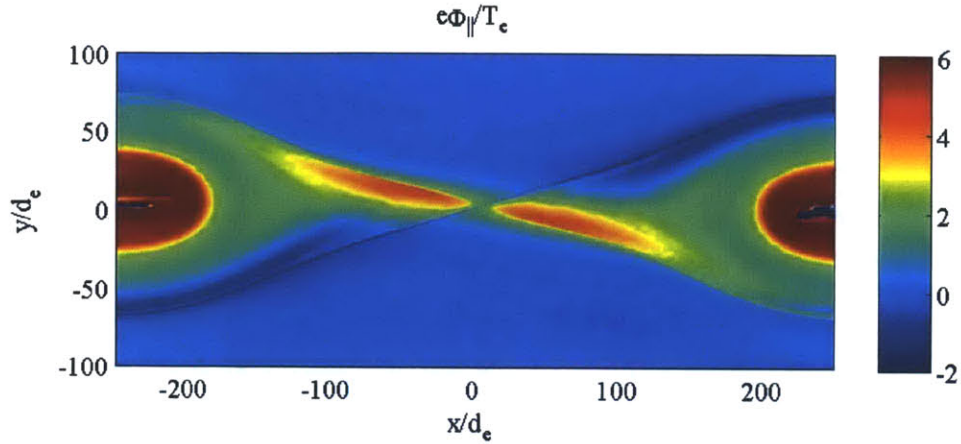


Figure 4-2: Parallel potential in a PIC simulation of reconnection with a guide magnetic field.

Fig. 4-1(c) shows that during magnetic reconnection with a guide field regions of enhanced plasma density develop along two of the separators. The density perturbations typically form at length scales over which the ions and electrons are decoupled. In order to maintain quasi-neutrality, an electric field parallel to the magnetic field accelerates electrons (which are magnetized on these scales) into regions with enhanced density of ions (which are not magnetized) and traps electrons in those regions. It follows from the first moment of Eq. 2.7 that the electron density scales as $n \propto (e\Phi_{\parallel}/T_e)^{1/2}$ for large $\Phi_{\parallel} \gg T_e/e$ neglecting magnetic effects. This is a relatively weak response compared, for example, to a collisional Boltzmann gas in which the density increases exponentially with a potential $-U$ as $n \propto \exp(U/T)$. Given the new equations of state, very large parallel potentials are therefore required to accommodate increases in density. The role of Φ_{\parallel} in regulating the electron density is reflected in the fact that Φ_{\parallel} (Fig. 4-2) is localized to the regions of enhanced density [Fig. 4-1(c)]. Due to the open boundary conditions, Φ_{\parallel} need not vanish at the simulation edge, so the integration constant is fixed by matching to $\Phi_{\parallel}(n, B)$ at the midway point of each field line. $e\Phi_{\parallel}$ reaches a maximum of $4 - 5T_e$, implying that the majority of electrons in regions of enhanced density are electrically trapped.

As shown in the previous chapter, in addition to regulating the electron density,

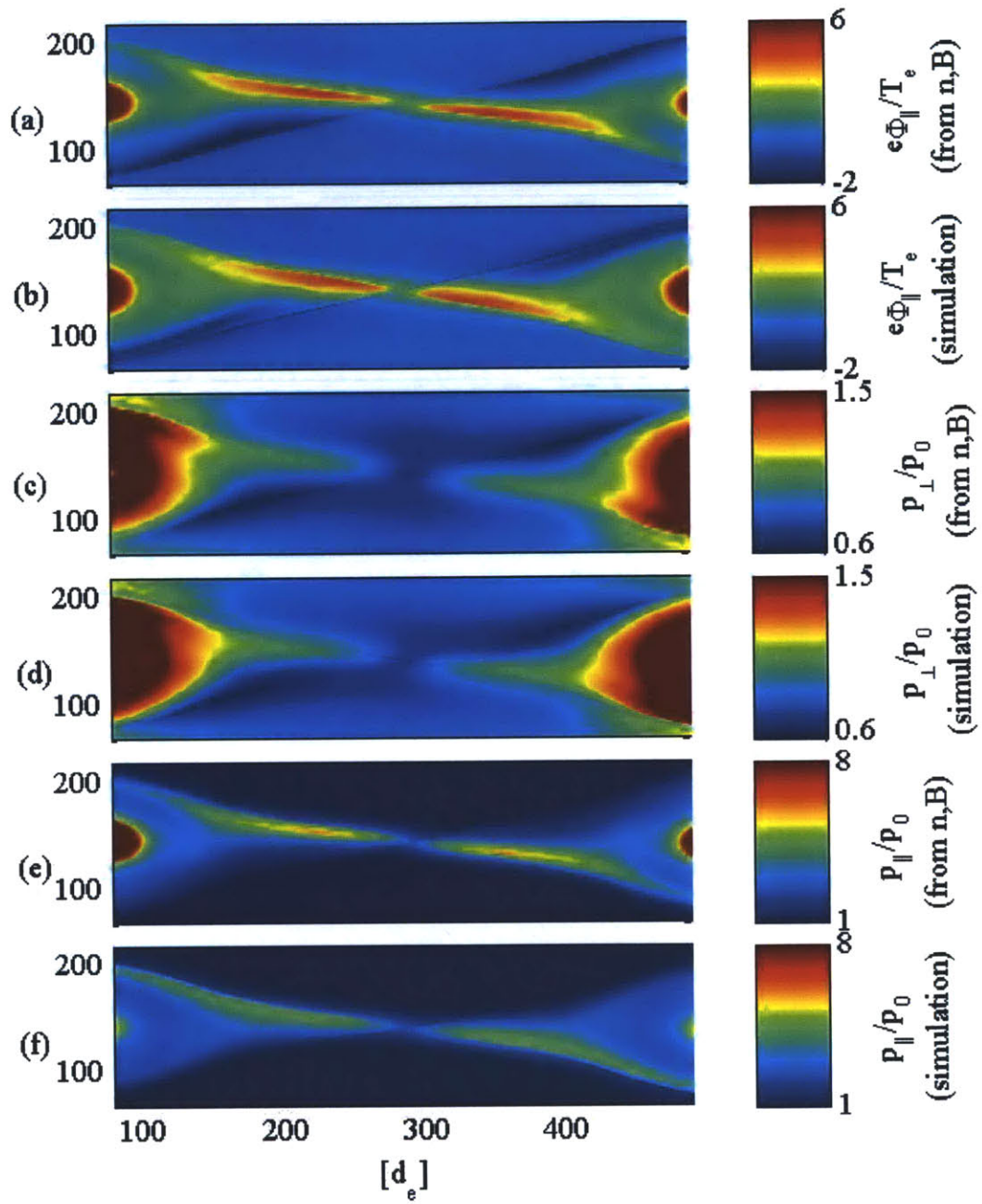


Figure 4-3: Comparison of direct PIC simulation results to the equations of state, which predict the pressure and parallel potential profiles based on the PIC density and magnetic field strength.

the parallel electric field heats the electrons in the parallel direction. Because the guide field is strong enough to magnetize the electrons nearly everywhere, this parallel heating should be captured by the equations of state. In fact, both the parallel and perpendicular components of the gyrotropic pressure tensor are well-described by the equations of state. To show that the parallel potential Φ_{\parallel} is consistent with the model, its computed profile is compared to the predicted profile based on n and B in Figs. 4-3(a,b). Also in Fig. 4-3 are similar comparisons of the parallel and perpendicular pressure profiles, both from the PIC code and predicted by the equations of state based on the values of n and B from the simulation. The parallel and perpendicular pressure profiles, calculated using $\Phi_{\parallel}(n, B)$, agree well with the pressures obtained directly from the PIC simulation. In the outflow region, the parallel pressure reaches nearly five times its boundary value, yet our fluid model differs from the PIC simulation by less than $\sim 20\%$ throughout the simulation domain. This pressure corresponds to a parallel temperature of $\sim 4T_e$, and it agrees with a scaling predicted by our model, $T_{\parallel} \sim (2/3) \times (e\Phi_{\parallel} + T_e)$, valid for large Φ_{\parallel} . Similarly, while the perpendicular pressure drops to half its boundary value, the numerical results and our model agree everywhere to within a few percent. The parallel heating by E_{\parallel} , along with the adiabatic perpendicular cooling associated with the conservation of μ in a decreasing magnetic field, leads to the pressure anisotropy $p_{\parallel}/p_{\perp} \sim \pi\tilde{n}^3/12\tilde{B}^2$ predicted by the equations of state. In this case, the electron pressure becomes strongly anisotropic and the maximum ratio of nearly $p_{\parallel}/p_{\perp} \sim 5$ predicted by the equations of state is reached in the simulation.

The parallel pressure from the PIC simulation and from the new fluid model are plotted in Fig. 4-4 as functions of y along a cut $30d_e$ to the right of the X-line (the same cut used in Fig. 4-1(d-g)). For comparison, Fig. 4-4(b) presents similar plots based on data from another PIC simulation with a mass ratio of $m_i/m_e = 180$, but otherwise identical. Most notably, agreement between the fluid model and the PIC simulation improves for the higher, more physically realistic mass ratio. As the mass ratio increases, the electron bounce and transit times become comparatively shorter, and it approaches the limit in which the fluid model is exact.

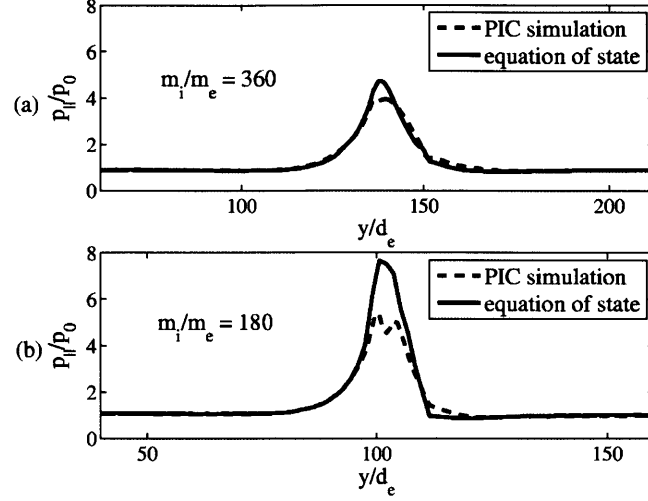


Figure 4-4: Comparison of equation of state for the parallel pressure to simulation results at two different mass ratios.

As noted in Ref. [68], the distribution function of Eq. 2.7 is formally only the zero-order term in an expansion $f = f^{(0)} + f^{(1)}(u/v_{the}) + f^{(2)}(u/v_{the})^2 + \dots$, where u is the mean flow speed. Even moments, such as the density, $n = \int f d^3v$, the parallel pressure, $p_{\parallel} = \int m v_{\parallel}^2 f d^3v$, and the perpendicular pressure, $p_{\perp} = (1/2) \times \int m v_{\perp}^2 f d^3v$, can be obtained by direct integration. On the other hand, the fluid flow \mathbf{u} , an odd moment, must be found using another method. The flow may be deduced from the momentum conservation equation, which relates the first-order flows to the zero-order pressure. The perpendicular electron current $\mathbf{j}_{e\perp} = -ne\mathbf{u}_{e\perp}$ is obtained by considering force balance in given electric and magnetic fields. Neglecting inertia and assuming a gyrotropic pressure tensor, momentum balance requires a perpendicular electron current given by

$$\mathbf{j}_{e\perp} \approx -ne \frac{\mathbf{E} \times \mathbf{B}}{B^2} + \frac{1}{B} \hat{\mathbf{b}} \times \nabla p_{\perp} + \frac{1}{B} \hat{\mathbf{b}} \times (p_{\parallel} - p_{\perp}) \kappa, \quad (4.2)$$

where $\kappa = \hat{\mathbf{b}} \cdot \nabla \hat{\mathbf{b}}$ is the magnetic field curvature vector. The perpendicular electron current is thus composed of three pieces: the first term in Eq. 4.2 stems from the

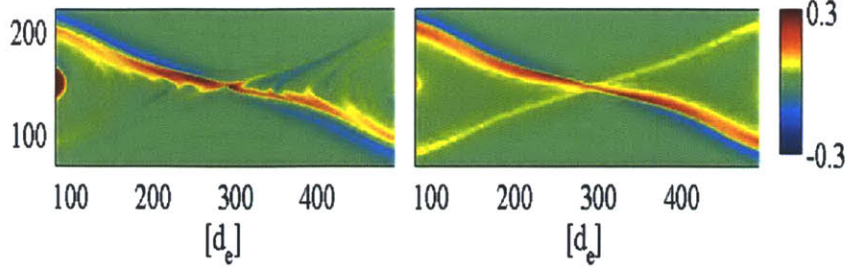


Figure 4-5: Prediction for the parallel electron current compared to PIC results.

$\mathbf{E} \times \mathbf{B}$ drift, and the remaining currents arise from grad-B and curvature drifts and the magnetization current. The last term is especially important near the X-line, where the magnetic field lines are tightly curved and the parallel pressure is often several times greater than the perpendicular pressure (again, reaching $p_{\parallel}/p_{\perp} \sim 5$ in the above simulation). Once the perpendicular electron currents are known in a given magnetic geometry, the parallel current $j_{e\parallel} = \mathbf{j}_e \cdot \hat{\mathbf{b}}$ follows from the steady-state electron continuity equation. Along each magnetic field line, the continuity equation $\nabla \cdot \mathbf{j}_e = 0$ becomes the following differential equation for $j_{e\parallel}$:

$$\frac{d}{dl} j_{e\parallel} = -j_{e\parallel} \nabla \cdot \hat{\mathbf{b}} - \nabla \cdot \mathbf{j}_{e\perp}, \quad (4.3)$$

where l parametrizes the length along the field line. The result of integrating this equation is compared to the parallel current directly computed by the PIC simulation (Fig. 4-5). The boundary condition is fixed by matching to the PIC values at the point where each field line enters the simulation domain.

Because the new fluid closure applies nearly everywhere during reconnection with a strong guide field, it can be incorporated into fluid codes that model guide field reconnection. Ohia of the VTF group has already implemented the new equations of state in two-fluid simulations performed on the HiFi framework developed by Lukin of NRL. By including the strong pressure anisotropy predicted by the equations of state, the new fluid code agrees much better with PIC simulation results. The pressure anisotropy is necessary to reproduce the elongated, narrow current layers that form

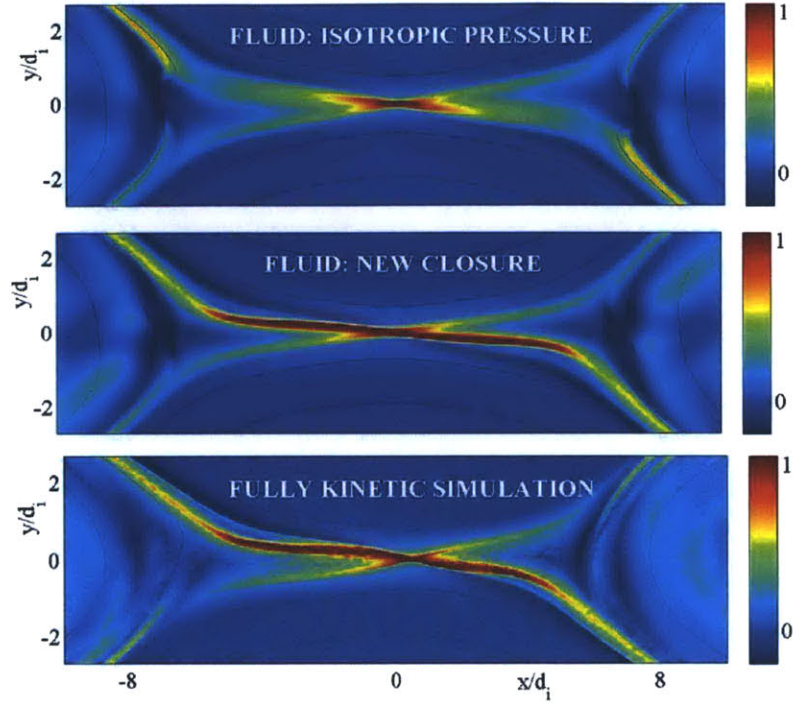


Figure 4-6: Comparison of kinetic simulation to fluid simulations, with and without the new equations of state.

in kinetic simulation. Fig. 4-6 compares results of a PIC simulation of reconnection with a strong guide field to fluid code runs with and without the new equations of state. The out-of-plane current forms an elongated channel in the PIC simulation and the code that uses the new fluid closure, but the current profile is very different in the run that employs a simple isotropic, isothermal fluid closure for the electrons.

Summary. The equations of state hold nearly everywhere during reconnection with a strong guide field, as shown by *Le et al.* in Ref. [68]. In the kinetic regime, ions and electrons decouple at small scales (below d_i), and a parallel potential Φ_{\parallel} develops to maintain quasi-neutrality. Besides trapping electrons in regions of enhanced density, Φ_{\parallel} heats the electrons in the parallel direction and leads to strong pressure anisotropy with $p_{\parallel} \gg p_{\perp}$. The pressure anisotropy drives strong, but localized, electron currents. All of the predictions are borne out in fully kinetic PIC simulations carried out on the VPIC code by Daughton [67].

Chapter 5

Neutral Sheet Reconnection

Neutral sheet, or anti-parallel, reconnection refers to the situation where the magnetic field shears through 180° across a plasma current layer, and the total magnetic field \mathbf{B} therefore passes through zero. Reconnection in this configuration has long served as a model for the dynamics of the plasma sheet in Earth's magnetic tail [12]. One characteristic of the electron dynamics during anti-parallel reconnection is strong electron temperature anisotropy with $T_{\parallel} > T_{\perp}$ that develops in the inflow region. Another feature is a system of electron-scale Hall currents that produce a signature magnetic field structure observed in spacecraft measurements, numerical simulation, and laboratory experiments [16,37,38,52,67,86]. In kinetic simulations, a jet of outflow electrons [88-90] streaming faster than the $\mathbf{E} \times \mathbf{B}$ speed produces a quadrupolar Hall magnetic field. It is shown in this chapter how the electron temperature anisotropy, which is described by the equations of state, and the Hall magnetic field sustain each other and that both are functions of the upstream β_e (the ratio of electron fluid and magnetic pressures).

An important difference from guide field reconnection is that in anti-parallel reconnection the magnetic field goes to zero, so that electron orbits cannot be treated as magnetized within the neutral sheet. Even as reconnection proceeds, regions of very weak magnetic field persist around neutral points. In principle, this precludes the use of the equations of state, which assume that the electrons remain magnetized. Upstream from the neutral sheet, however, the electrons are magnetized. Because

this geometry contains regions where the electron are magnetized and where they are not, this configuration provides a test of the limits of validity of the equations of state. Furthermore, it turns out that the electron temperature anisotropy predicted by the equations of state just outside the neutral sheet, where the electrons are still magnetized, imposes useful relationships between the upstream electron pressure and the Hall magnetic fields.

To explore the application of the equations of state to anti-parallel reconnection, PIC simulations were performed to study the electron diffusion region around an X point [69]. Fig. 5-1 shows field profiles from one such simulation. As in the simulations with guide field, magnetic reconnection with a single X-line evolves from a small initial perturbation, and the data are shown a time after the reconnection rate has saturated and reached a quasi-steady state. The PIC code is translationally symmetric in the z -direction and has a total domain of 2560×2560 cells = $400d_e \times 400d_e$. The initial state is a Harris neutral sheet ($B_{\text{guide}} = 0$) with gradients in the y direction and is characterized by the following parameters: $m_i/m_e = 400$, $T_i/T_e = 5$, $\omega_{pe}/\omega_{ce} = 2$, and background density = $0.3 n_0$ (peak Harris density).

The density n is fairly uniform in the vicinity of the X-line, while the value of B becomes very low (Fig. 5-1(a,b)). The quadrupolar out-of-plane Hall magnetic field B_z is shown in Fig. 5-1(c). The focus here is on the inner electron diffusion layer near the X-line where strong electron currents out of the plane j_z and in the outflow direction j_x (Fig. 5-1(d,e)) move in a narrow channel. The electrostatic potential Φ in Fig. 5-1(f) is negative throughout the outflow region, consistent with perpendicular electric field measurements of a reconnecting current sheet in the magnetotail [91]. This in-plane potential tends to accelerate ions into the outflow. The parallel potential Φ_{\parallel} , on the other hand, is more important for the electron dynamics and contains a contribution from the out-of-plane inductive reconnection electric field E_z . As seen in Fig. 5-1(g), Φ_{\parallel} is therefore positive, reaching nearly $\Phi_{\parallel} \sim 4T_e/e$, and it traps a large fraction of the inflow electrons.

As mentioned above, the equations of state derived for guide-field reconnection also apply in the anti-parallel case to the inflow region where the electrons are mag-

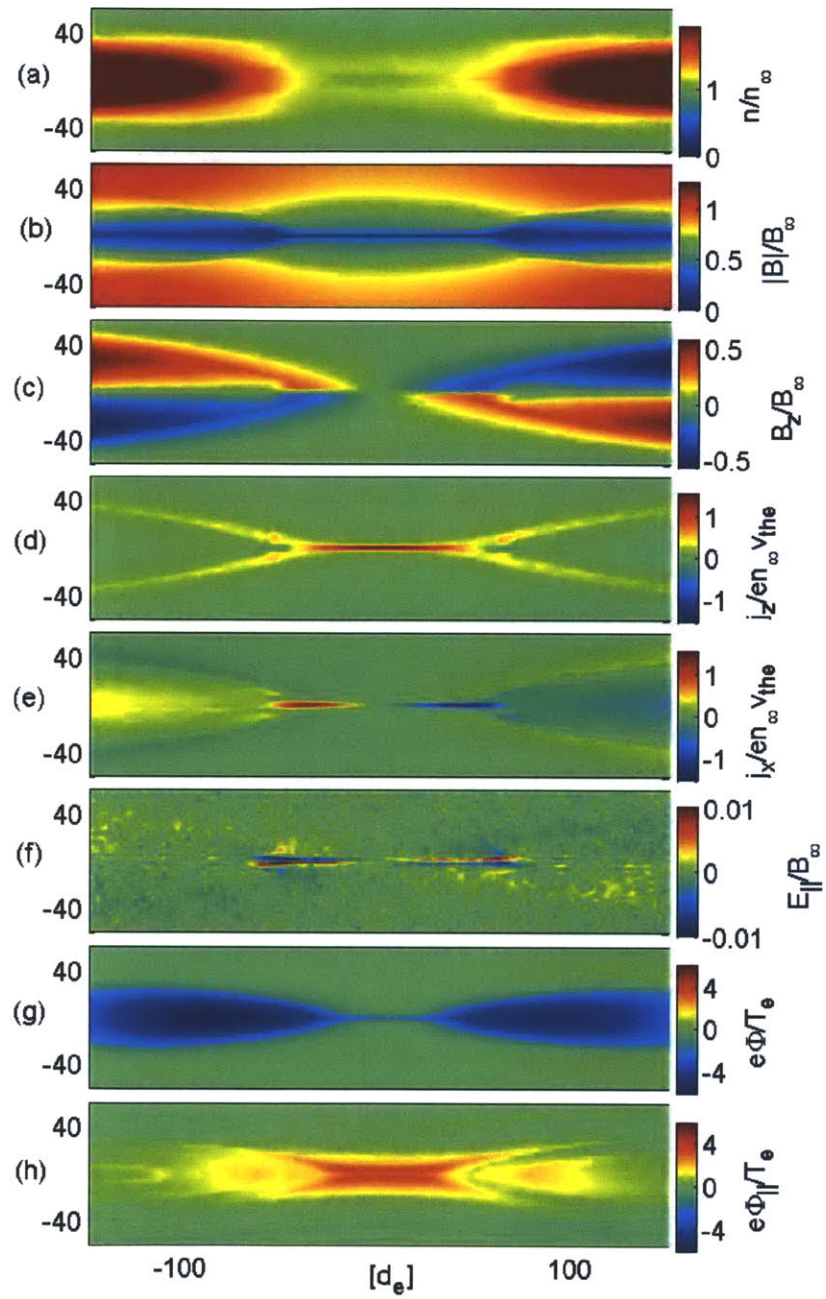


Figure 5-1: Profiles from a PIC simulation of neutral sheet reconnection.

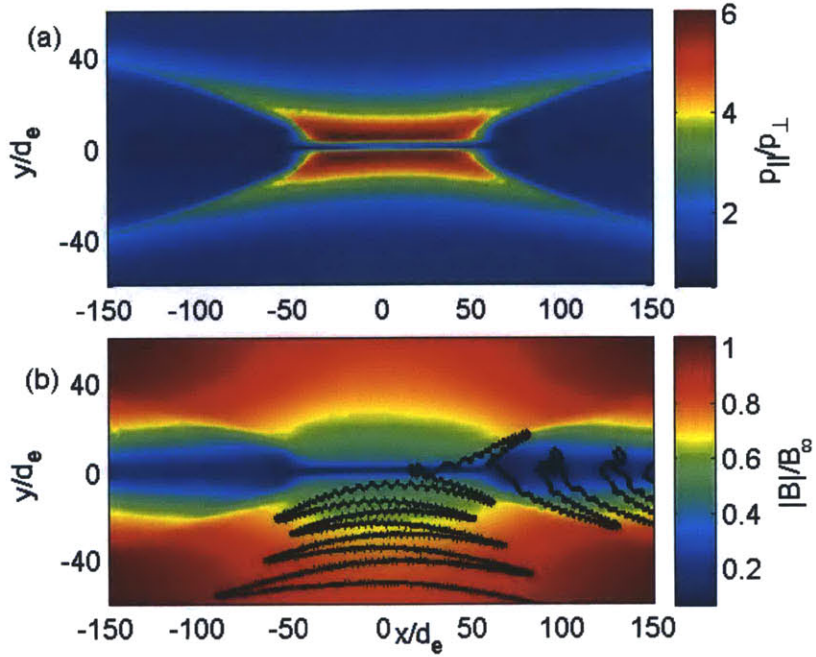


Figure 5-2: Pressure ratio and magnetic field strength with a typical trapped electron orbit.

netized. They agree with the PIC simulation to within $\sim 10\%$ up to a layer a few $d_e = c/\omega_{pe}$ wide. The temperature anisotropy in the inflow region is substantial: for the present simulation, the maximum upstream temperature ratio is almost $T_{\parallel}/T_{\perp} \sim 7$ (see Fig. 5-2(a)). In the outflowing exhaust where the equations of state are inapplicable, however, the temperature becomes nearly isotropic. The velocity-space isotropy results from electrons effectively being pitch-angle scattered during their passage through the very weak magnetic field. The magnetic field strength B is plotted in Fig 5-2(b) along with an example trapped electron orbit. The electrons repeatedly cross the region of weak magnetic field where μ is not conserved, and this loss of pitch angle coherence leads to a nearly isotropic pressure tensor.

In the Sweet-Parker and other resistive models, the reduced Ohm's law $\mathbf{E} + \mathbf{u} \times \mathbf{B} = \eta \mathbf{J}$ is essential for determining the reconnection rate. By analogy, it has been typical in reconnection research to focus on electron momentum balance in the direction

of the reconnection electric field due to its role in breaking the frozen-in condition. To understand the structure of the electron jets and diffusion region in anti-parallel reconnection, it proves most fruitful to instead consider perpendicular momentum balance. In the electron diffusion region, the electrons carry essentially all of the current and therefore nearly all of the $\mathbf{J} \times \mathbf{B}$ force exerted on the plasma. Due to the substantial current in the electron jets, the magnetic field lines are tightly curved. This corresponds to a strong perpendicular magnetic tension force, indicated schematically in Fig. 5-3. It turns out this is the largest electromagnetic force on the electrons by at least an order of magnitude, and it is balanced by the electron pressure anisotropy.

The importance of the temperature anisotropy is highlighted by steady-state electron momentum balance written in the form

$$0 = \nabla_i \{ (B^2/2\mu_0 + p_\perp) \delta_{ij} + (p_\parallel - p_\perp - B^2/\mu_0) b_i b_j \} + F_i, \quad (5.1)$$

where the electron pressure tensor P_{ij} is used to define $p_\perp = \frac{1}{2} \{ P_{ij} (\delta_{ij} - b_i b_j) \}$ and F_i contains the electric field, non-gyrotropic pressure, and inertia contributions. Because the field lines are sharply curved, $\nabla_i b_i b_j$ is large. The corresponding tension is balanced by the anisotropic electron pressure, such that just outside the extended electron jets $(p_\parallel - p_\perp - B^2/\mu_0) \approx 0$. In fact, a similar condition must hold immediately outside any steady-state, one-dimensional current layer with a normal magnetic field [92, 93].

For the present geometry, consider x -momentum balance for a differentially narrow fluid element extending $\sim 4d_e$ across the outflow jet (for example, the small shaded box in the top of Fig. 5-4). Eq. 5.1 is integrated over the electron layer using the divergence theorem for the terms in brackets. The largest contributions come from $B^2 b_x b_y$ and $(p_\parallel - p_\perp) b_x b_y$ evaluated immediately outside the jet and are plotted in Fig. 5-5. Also plotted are smaller contributions from x gradients in the stress tensors and flow velocity integrated across the layer (along the sides of the shaded box), where the full non-gyrotropic electron pressure tensor is taken from the code. Although

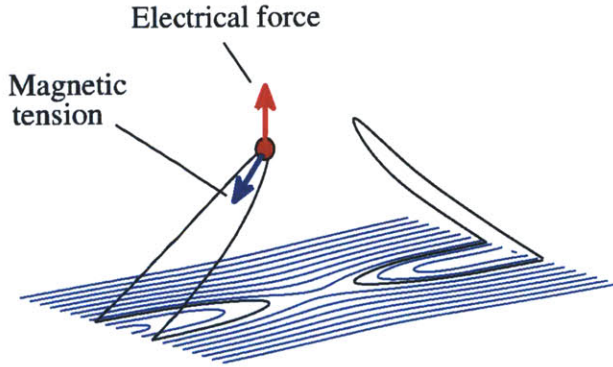


Figure 5-3: The magnetic tension and electrical forces acting on an electron fluid element in an outflow jet.

relatively small, inertia and the (comparable) electric force influence the internal structure of the electron jets, and they become important where the flows peak and then terminate roughly $40d_e$ downstream from the X-line.

Thus, although the electrons acquire a significant outflow velocity within the jets, which can exceed the upstream thermal speed v_{the} , it is clear from Fig. 5-5 that the tension portion of the $\mathbf{J} \times \mathbf{B}$ force associated with $B^2 b_i b_j$ (sketched in bottom of Fig. 5-4) is much greater than the force required to accelerate the electrons. The magnetic tension force is largely balanced by the anisotropic electron pressure, and the relevant outside terms approximately cancel: $p_{\parallel} - p_{\perp} \approx B^2/\mu_0$. This level of pressure anisotropy with $p_{\parallel} > p_{\perp}$ is also the threshold for the electron fire hose instability.

Several scaling laws may be derived from the main result from force balance considerations, that $p_{\parallel} - p_{\perp} \approx B^2/\mu_0$ immediately upstream from the electron jets. Combined with the equations of state $p_{\parallel}(n, B)$ and $p_{\perp}(n, B)$, this condition determines parameters of the electron diffusion region. Fig. 5-6 shows $p_{\parallel} - p_{\perp}$ and B^2/μ_0 as functions of y along a typical cut $15d_e$ to the right of the X-line using both the simulation data and the equations of state. The solution to $p_{\parallel}(n, B) - p_{\perp}(n, B) = B^2/\mu_0$ (where the blue and green lines in Fig. 5-6 intersect) gives the value of the magnetic field strength immediately outside the electron jet, denoted here by B_H .

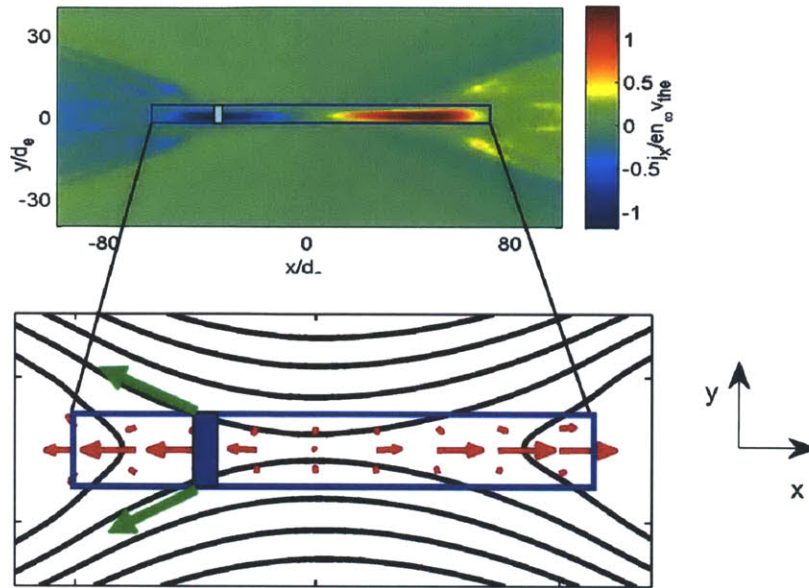


Figure 5-4: The magnetic tension force (green arrows) on an electron fluid element is balanced by anisotropic pressure gradients.

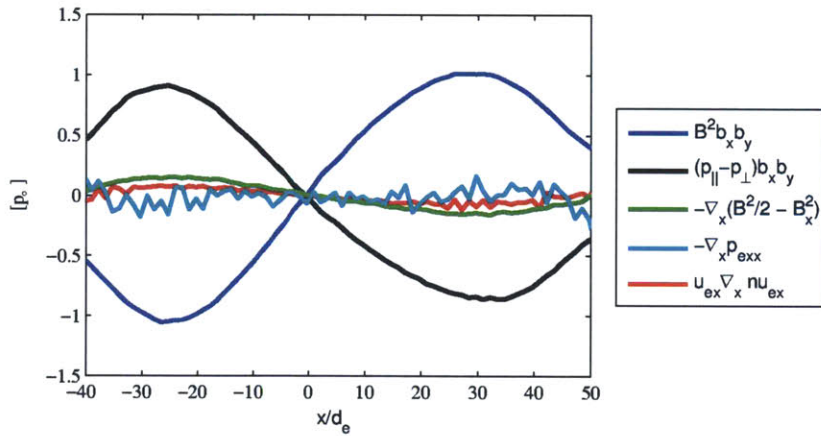


Figure 5-5: Magnetic tension and anisotropic pressure dominate x momentum

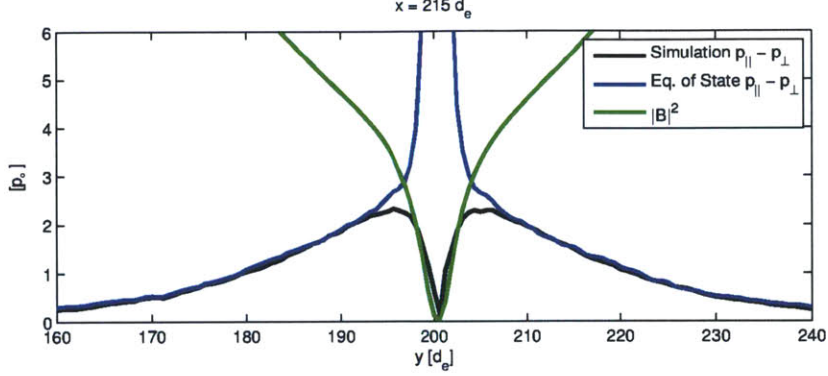


Figure 5-6: Pressure anisotropy and magnetic tension along a simulation cut.

In each of the simulations, the density is approximately uniform with $\tilde{n} \approx 1$. Using this result, B_H is then only a function of the ratio of electron to magnetic pressure at the inflow boundary, $\beta_{e\infty} = 2\mu_0 p_{e\infty}/B_\infty^2$. This relation is shown in Fig. 5-7(a). Following from the asymptotic limits of the equations of state, an approximate form valid for small \tilde{B}_H is

$$\frac{B_H}{B_\infty} \approx \left(\frac{\pi \tilde{n}^3 \beta_{e\infty}}{12} \right)^{1/4}. \quad (5.2)$$

Kinetic simulations confirm the above relationship. The scaling law is compared to three PIC simulations of reconnecting current sheets, each using a mass ratio of $m_i/m_e = 400$, but with varying electron $\beta_{e\infty}$. B_H is evaluated where the out-of-plane electron current reaches 40% of its maximum (roughly $(2 - 4d_e)$ from the peak) and is marked in Fig. 5-7(a) for the three numerical studies. The middle simulation is a run on the code P3D with fully periodic boundary conditions [88], and the others implement open boundary conditions on VPIC [67].

Similarly, the equations of state provide an estimate for the maximum electron temperature ratio T_{\parallel}/T_{\perp} . As visible in Fig. 5-6, the equations of state break down slightly before B reaches the predicted value of B_H . Empirically, it is found that evaluating the equations of state at $1.25B_H$ (which corresponds to a point where the equations of state are still valid) gives a good estimate for the maximum T_{\parallel}/T_{\perp} in agreement with the three simulations. The scaling plotted in Fig. 5-7(c) is approxi-

mately

$$\left(\frac{T_{\parallel}}{T_{\perp}}\right)_{max} \approx \left(\frac{1}{4\tilde{n}\beta_{e\infty}^3}\right)^{1/4}. \quad (5.3)$$

The temperature anisotropy in the inflow region is largely due to particle trapping by the parallel electric field, or equivalently Φ_{\parallel} . Fig. 5-7 plots the prediction for Φ_{\parallel} at the point of maximum temperature anisotropy upstream from the electron outflow jets, obtained from the relationship $\Phi_{\parallel} = \Phi_{\parallel}(n, B)$ with $n = n_{\infty}$ and $B = 1.25B_H$. Note that for low $\beta_{e\infty}$, the low value of B_H induces a large Φ_{\parallel} , scaling roughly as

$$\left(\frac{e\Phi_{\parallel}}{T_{e\infty}}\right)_{max} \approx \frac{1}{2} \left[\left(\frac{4\tilde{n}}{\beta_{e\infty}}\right)^{1/4} - \frac{1}{2} \right]^2, \quad (5.4)$$

and the majority of inflow electrons are trapped. Because β_e is often very low in Earth's magnetotail, electrical trapping in the inflow region is likely a crucial mechanism for creating the upstream electron temperature anisotropy with $T_{\parallel} > T_{\perp}$ observed by both the Cluster and Wind spacecraft near reconnecting current sheets [94]. The plasma beta is also often very low above active regions of the solar corona [95]. Large parallel potentials could therefore possibly generate the electrons with large parallel energies associated, for example, with Type III radio bursts during solar flares [96]. The model, however, requires some generalizations for $\beta_{e\infty} < 0.01$ to account for effects of a very large $\Phi_{\parallel} > 10T_e/e$ [97].

Based on the scaling of Φ_{\parallel} with β_e derived above, Egedal proposed in Ref. [98] that kinetic simulations run at lower β_e more typical of the magnetotail would better match the strong electron heating observed, for example, by the Cluster spacecraft during a reconnection even on October 1st, 2001 [94, 99]. The pressure in that event became extremely anisotropic, and the details of the electron distribution in Fig. 5-8 are consistent with a parallel potential of $\sim 100T_e$. To test the proposal that more realistic values of β_e are necessary to reproduce the observed heating, a PIC simulation with an upstream value of $\beta_e \sim 0.003$ has been carried out. In order to eliminate boundary effects, the simulation domain is very long in the outflow direction. The profiles of the density n , parallel electric field E_{\parallel} , and parallel potential Φ_{\parallel} are plotted

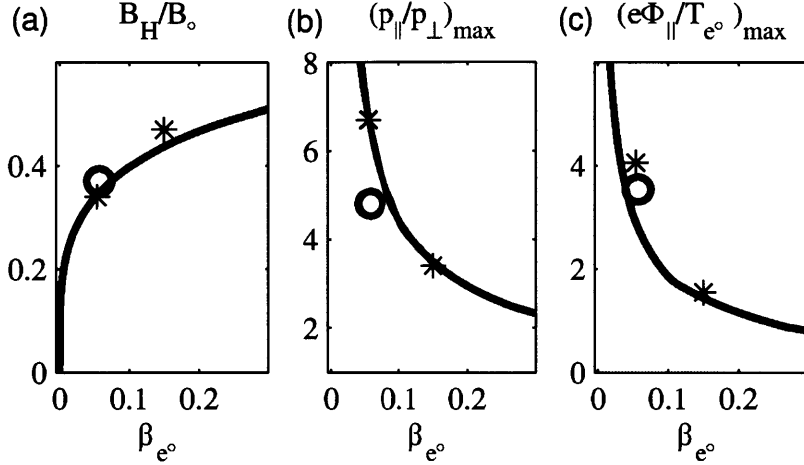


Figure 5-7: Predicted scaling laws and values from three simulations.

in Fig. 5-9. The parallel electric field E_{\parallel} exhibits substantial fluctuations, including bipolar electrostatic structures that are most likely electron holes. These fluctuations are superposed on a large-scale coherent field that integrates up to a significant parallel potential Φ_{\parallel} . In fact, the simulation confirms that the parallel potential becomes extremely large ($e\Phi_{\parallel} \sim 100T_e$) under these plasma conditions. Surprisingly, Φ_{\parallel} extends over much longer length scales than previously thought possible, and it is not limited to localized d_e scales. This mechanism can therefore populate large volumes of the magnetotail with energetic electrons.

For a given β_{e^∞} , the equations of state predict a unique value for B_H . In turn, this value of B_H imposes the value the net current in the electron layer through Ampere's law. This implies another result consistent with the simulations: the magnetic field strength is nearly uniform along the current sheet. While its magnitude is roughly constant, the magnetic field's direction rotates along the outflow jet, producing the characteristic Hall field B_z , in agreement with earlier descriptions [52]. This result is somewhat surprising because the total electron current is therefore independent of the reconnection electric field. Unlike the current density in resistive models, where $J = E/\eta$, the electron current at the X line and in the electron jets in this kinetic regime is insensitive to the strength of the electric field. This has been verified in

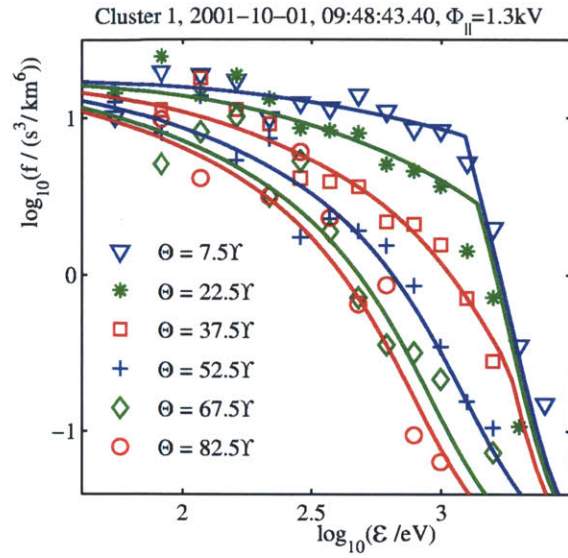


Figure 5-8: Cluster spacecraft observations of electron distributions are consistent with a parallel potential of $e\Phi_{\parallel} \sim 100T_e$.

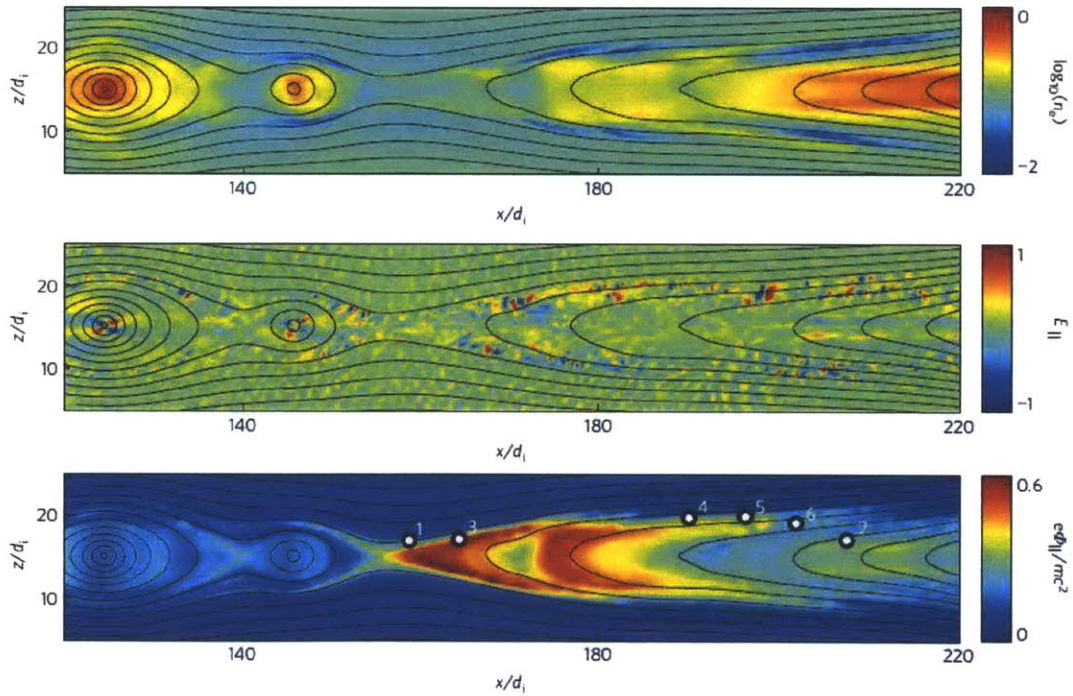


Figure 5-9: Density, parallel electric field, and parallel potential in a large PIC simulation.

Ref. [100] by artificially varying the reconnection electric field within the narrow electron layer in PIC simulations. When the field E_y is doubled or set to zero within the layer, the current density profile changes somewhat. On the other hand, the total integrated electron current remains the same, and it is determined by the level of external anisotropy.

Based on the known total current, a simple model describes the currents in the electron jets. Approximate the outflow jet as a sheet with current density $2\mathbf{K}$ and with the magnetic field immediately outside given by $\mathbf{B} = \mathbf{e}_y \times \mu_0\mathbf{K} + B_y\mathbf{e}_y$. Along the outside of the jet, $|B_y|^2 \ll |K|^2$ for tens of d_e , and the uniformity of B_H (and n_e) thus imply that

$$u_{ex}^2 + u_{ez}^2 \sim (B_H/ne\delta)^2 = u_j^2 = \text{const.} \quad (5.5)$$

where \mathbf{u}_e is the electron flow in the sheet and δ is the current layer half width.

The simulation suggests that this inflow velocity is roughly constant along the layer, which allows a solution for the outflow velocity components. To determine u_{ex} , we first consider mass conservation:

$$\delta \frac{\partial}{\partial x} u_{ex} \sim u_{ey} \sim \text{constant}, \quad (5.6)$$

from which it follows that $u_{ex} = u_j(x - x_0)/L$. Using Eq 5.5, we then find $u_{ez} \sim u_j \sqrt{1 - ((x - x_0)/L)^2}$, where $x = x_0$ corresponds to the X-line. The characteristic length L is not predicted by the model, and it depends on the reconnection rate and other external factors.

The equations of state thus yield a relatively simple fluid model for the gross features of the electron layer during anti-parallel reconnection. The internal structure of the layer, however, is determined by the complex structure of the electron phase space distribution. While global momentum balance is ensured by the external pressure, electron kinetic effects, including highly non-gyrotropic pressure, govern local momentum and energy balance. Below are results obtained by Ng *et al.* in Ref.[100]. In that paper, high-resolution electron distributions are calculated in the electromagnetic fields from the PIC simulation by tracing many (a few million) sample electron

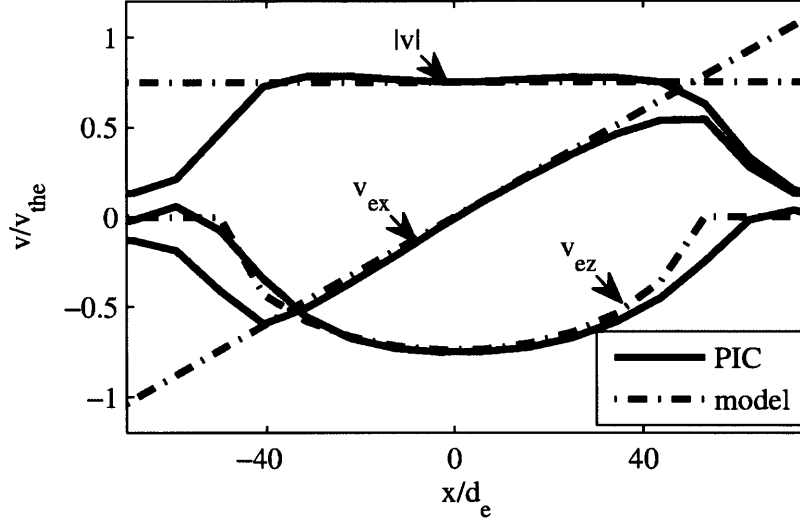


Figure 5-10: Simple model for the electron currents in a jet.

orbits from points within the electron layer [100]. The resolution is enhanced over the PIC results, and it has been verified that the calculated distributions reproduce the lowest-order moments, namely density and current, that act as sources for the electromagnetic fields.

As mentioned above, the electron distribution outside the electron layer is given by Eq. 2.7, and it is highly elongated parallel to the magnetic field. Within the layer, the electron distribution is more complicated. Isosurfaces in 3D velocity space of the electron distribution plotted in Fig. 5-11(a) are reproduced from the paper by Ng *et al.* [100]. The distribution is separated into two distinct populations, formed by electrons with positive or negative velocity across the layer in the z direction. It also becomes filamented into a series of fingers, which maintain the elongated character of the external distribution. The fingered structure is related to the bouncing motion of electrons within the inner layer. Trajectories of electrons with zero (red), one (blue), and two (magenta) bounces are plotted in Fig. 5-12, superposed on contours of the Hall electric field E_z that borders the electron layer. Electrons that bounce more times pick up energy in the out-of-plane y direction, and the energetic tail of the

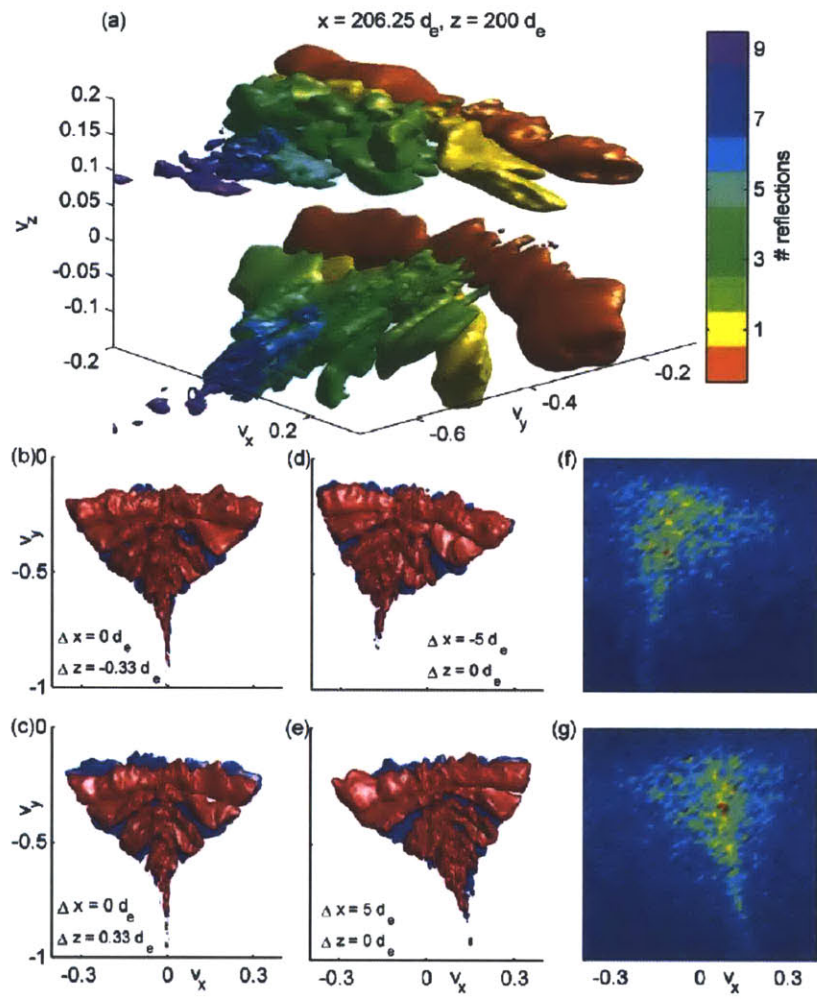


Figure 5-11: High-resolution electron phase space distributions from the paper by Ng *et al.* [100]

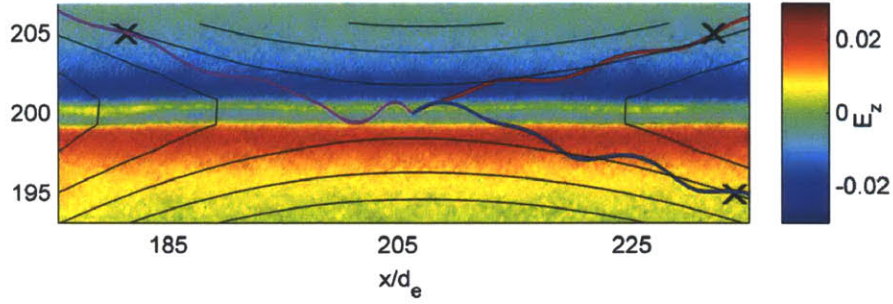


Figure 5-12: Electron bouncing motion generates finger-like phase space structures.

triangular distribution is composed of electrons that bounce many times within the layer and are accelerated out of the plane. The fingers in Fig. 5-11(a) are color-coded, and the color corresponds to the number of bounces within the layer.

In addition to a rich velocity space structure, the electron distributions have spatial gradients that are especially important for understanding local momentum balance within the electron layer. The distributions in Figs. 5-11(b,c) are from points slightly above and below ($0.33d_e$ away from) the X line. The small shift between the two populations of electrons leads to pressure gradients that balance the local electric field. Similarly, pressure tensor gradients are present due to the relative orientations of the distributions at points the left and right, plotted in Figs. 5-11(d,e) at $5d_e$ from the X line. For comparison, distributions from the PIC code are plotted in Figs. 5-11(f,g). While they have the same density, velocity, and pressure moments as the orbit tracing results, there are too few sample particles in the PIC code to resolve the detailed finger-like structures that arise in the electron phase space.

Summary. The equations of state originally derived for guide-field reconnection apply to the inflow region of the anti-parallel case. As described by Le *et al.* in Refs. [69] and [70], the equations of state link the electron pressure outside the reconnection region to the characteristic strength of the Hall magnetic field B_H through a momentum balance condition, $p_{\parallel} - p_{\perp} \approx B_H^2$. Following from the dominant terms

of the electron momentum balance equation integrated across the electron layer,

$$\int dV(\mathbf{J}_\perp \times \mathbf{B}) \approx \oint d\mathbf{A} \cdot (p_\parallel - p_\perp)\mathbf{bb}, \quad (5.7)$$

the volume-averaged perpendicular electron current is significant. Upstream temperature anisotropy and the curvature of the Hall magnetic field drive perpendicular electron currents beyond the $\mathbf{E} \times \mathbf{B}$ drift speed, and these currents in turn generate the Hall magnetic field. The equations of state set the parameters of this model in terms of the upstream magnetic field and electron pressure. An important new prediction is that the parallel potential scales as $\Phi_\parallel \propto \beta_{e\infty}^{-1/2}$, and electron heating is therefore greatest in low- β_e plasmas.

Chapter 6

Guide Field and Mass Ratio Scans

Previous chapters dealt with the cases of a strong guide field and zero guide field. A strong guide magnetizes electron orbits, and the pressure tensor is well-described by the equations of state throughout the reconnection region. In anti-parallel reconnection, on the other hand, the inflowing electron pressure becomes marginally firehose unstable and drives a collimated jet of outflowing electrons. Meanwhile, the exhaust electron pressure is nearly isotropic because pitch angle coherency is lost as electrons repeatedly pass through a region of very weak magnetic field where the orbits are chaotic and μ is not conserved. Models of reconnection in Earth's magnetic tail often assume that the initial magnetic field lines in the plasma sheet are precisely anti-parallel [12, 101]. Generic configurations, however, include a finite guide component of the magnetic field, meaning that the magnetic field shears through an angle less than 180° and does not pass through zero. The presence of even a small guide field component in realistic configurations calls into question the relevance of exactly anti-parallel models. This chapter explores how the fully evolved reconnection geometry depends on the strength of the guide field in configurations that range from the anti-parallel to the strong guide field regime.

Studies of reconnection with varying guide fields have previously been performed, both in Hall MHD fluid simulations [102] and in kinetic PIC simulations [103]. More recent kinetic simulations, however, demonstrate that the results are sensitive to the ion-to-electron mass ratio that is implemented numerically [104]. Due to the neces-

sity of greater spatial and temporal resolution for a fixed system size and simulation length measured on ion scales, the computational time required for an explicit PIC simulation in d spatial dimensions scales as $(m_i/m_e)^{(d+2)/2}$ [105]. To limit computational requirements, many previous PIC studies use mass ratios $m_i/m_e < 100$ [106]. Because they are so computationally intensive, large simulations at the physical proton-to-electron mass ratio of $m_i/m_e = 1836$ have only recently become feasible even in 2D. The simulations of Ref. [104] were performed on an implicit code (which sacrifices some accuracy at small scales for reduced computation time), and explicit simulations performed on VPIC and presented in this chapter have confirmed some of those findings.

A series of PIC simulations provided by Daughton vary both the guide field strength and the numerically implemented ion-to-electron mass ratio. Qualitatively different electron current structures evolve depending on the mass ratio. The new results help sort out which are artifacts of the numerical parameters. An example of where this may be important in making contact with observational data comes from Cluster spacecraft measurements. The Cluster spacecraft recorded evidence for an extended jet during reconnection in Earth's magnetosheath in the presence of a guide field of $\sim 16\%$ of the upstream reconnecting field. In Ref. [107], this electron jet is compared to an anti-parallel PIC simulation run that used a mass ratio of only $m_i/m_e = 25$. Based on the new scans of guide field and mass ratio presented in this chapter, it is rather unlikely that the simulation described in Ref. [107] suffices to explain the observational data. The observed jets may be more similar to an entirely new regime found in the present simulations. With intermediate guide fields at the physical proton-to-electron mass ratio, a very long ($> 15d_i$) electron current sheet driven by pressure anisotropy is embedded in the reconnection exhaust.

The new simulations vary the guide field and use three different ion-to-electron mass ratios of $m_i/m_e = 100, 400, \text{ and } 1836$. Each case is translationally symmetric in the y direction. The system sizes and the duration of each simulation are listed in Table 6.1. (Note that when m_i/m_e is varied, a system of fixed size in terms of d_i changes size measured in $d_e \propto \sqrt{m_e/m_i}d_i$. The initial conditions again contain a

Table 6.1: Simulation parameters.

Mass Ratio	Box Size			Final Time
m_i/m_e	$d_i \times d_i$	$d_e \times d_e$	cells	$1/\Omega_{ci0}$
100	40×20	400×200	2560×1280	43
400	20×20	400×400	2560×2560	25
1836	20×20	857×857	5120×5120	25

Harris sheet whose unperturbed magnetic field \mathbf{B} has components

$$\begin{aligned}
 B_x &= B_0 \tanh(z/\lambda) \\
 B_y &= B_g \\
 B_z &= 0,
 \end{aligned}
 \tag{6.1}$$

where $\lambda = 0.5d_i$ and the uniform guide field B_g is chosen from

$$B_g/B_0 \in \{0, 0.05, 0.07, 0.14, 0.2, 0.28, 0.4, 0.57, 0.8\}.
 \tag{6.2}$$

The Harris sheet plasma parameters are the same as those used in the previous chapter on anti-parallel reconnection: $T_{i0}/T_{e0} = 5$, and $\omega_{pe}/\omega_{ce} = 2$. This is superposed on a slightly cooler uniform background plasma with density $n_b = 0.22n_0$ (n_0 is the peak Harris density), $T_i/T_e = 5$, and $v_{the}/c = \sqrt{T_e/m_e c^2} = 0.13$. The density profiles in the final time slice of each simulation are plotted in Fig. 6-1.

First, it is useful to determine when the equations of state apply near the reconnection region. As described in previous chapters, the equations of state hold essentially everywhere for strong guide fields and in the inflow for zero guide field. In any case, the inflow electron pressure obeys the equations of state independent of the guide field as long as the mass ratio m_i/m_e is large enough to allow a fast electron bounce frequency. For the chosen background density and temperature, the ratio of upstream electron to magnetic pressures is $\beta_e = 2\mu_0 n_b T_e / B_0^2 \sim 3\%$. In most of the simulations, the ratio of components p_{\parallel}/p_{\perp} reaches ~ 10 upstream from the X line. This level of anisotropy is consistent with the scaling $p_{\parallel}/p_{\perp} \sim (4\beta_{e\infty}^3)^{-1/4}$ of the previous chapter. The ratio p_{\parallel}/p_{\perp} is plotted near the end of the simulation for

each of the runs in the scan in Fig. 6-2. Although the peak value varies somewhat depending on the density profile (plotted in Fig. 6-1, the equations of state are valid in the inflow region for each of the simulations.

In the reconnection exhaust, the level of electron pressure anisotropy does depend on the value of the guide field. In Fig. 6-2, there is a fairly abrupt transition between cases where the exhaust pressure is isotropic and cases where strong anisotropy develops following the equations of state. Recall that during anti-parallel reconnection, the equations of state do not hold in the exhaust because the magnetic field becomes very weak. The conservation of the adiabatic invariant μ breaks down, and the pressure becomes approximately isotropic. As a guide field component is added, the electron orbits will eventually become adiabatic. As mentioned in the introduction, the invariance of μ requires that the electron Larmor radius ρ_e be smaller than the magnetic field line radius of curvature R_B [74],

$$\frac{\rho_e}{R_B} \ll 1. \quad (6.3)$$

The ratio ρ_e/R_b , where $\rho_e = v_{the}/\Omega_{ce}$ is based on the upstream temperature, is plotted in Fig. 6-3. It is found empirically that the electron pressure becomes nearly isotropic when $\rho_e/R_b \sim 0.15$ in the central region of weak magnetic field. This falls in line with the theoretical predictions of Ref. [74]. A value of $\rho_e/R_b \sim 0.15$ corresponds to a value of the parameter $\kappa = \sqrt{R_B/\rho_e}$ introduced in Ref. [74] in the range $\kappa \sim 2 - 3$, and for this parameter regime the electron orbits are expected to become chaotic. In the kinetic regime of interest, the adiabatic or non-adiabatic nature of the electron orbits strongly influences the structure of the electron currents that develop.

Focusing on the cases with very weak guide field, the scan of parameters helps determine when the upstream pressure anisotropy may drive electron currents in an inner collimated layer near the X line during anti-parallel reconnection. Goldman *et al.* find in Ref. [104] that these inner electron jets can be deflected even for very weak guide fields. The deflection is most pronounced at higher mass ratios m_i/m_e , and guide fields of $\sim 5\%$ may nearly eliminate the inner electron jets at the physical

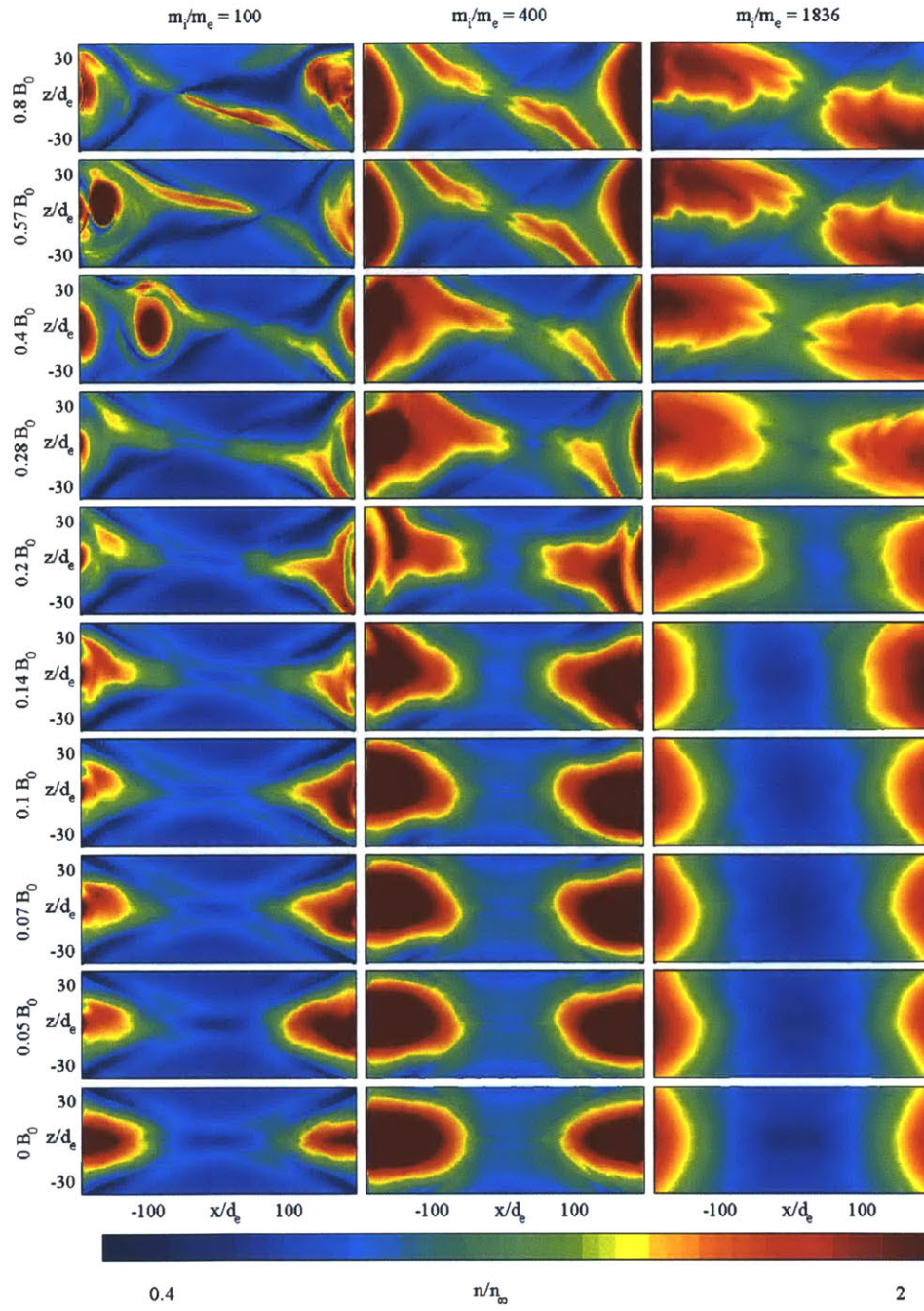


Figure 6-1: Guide field and mass ratio scan: plasma density n normalized to background density n_∞ .

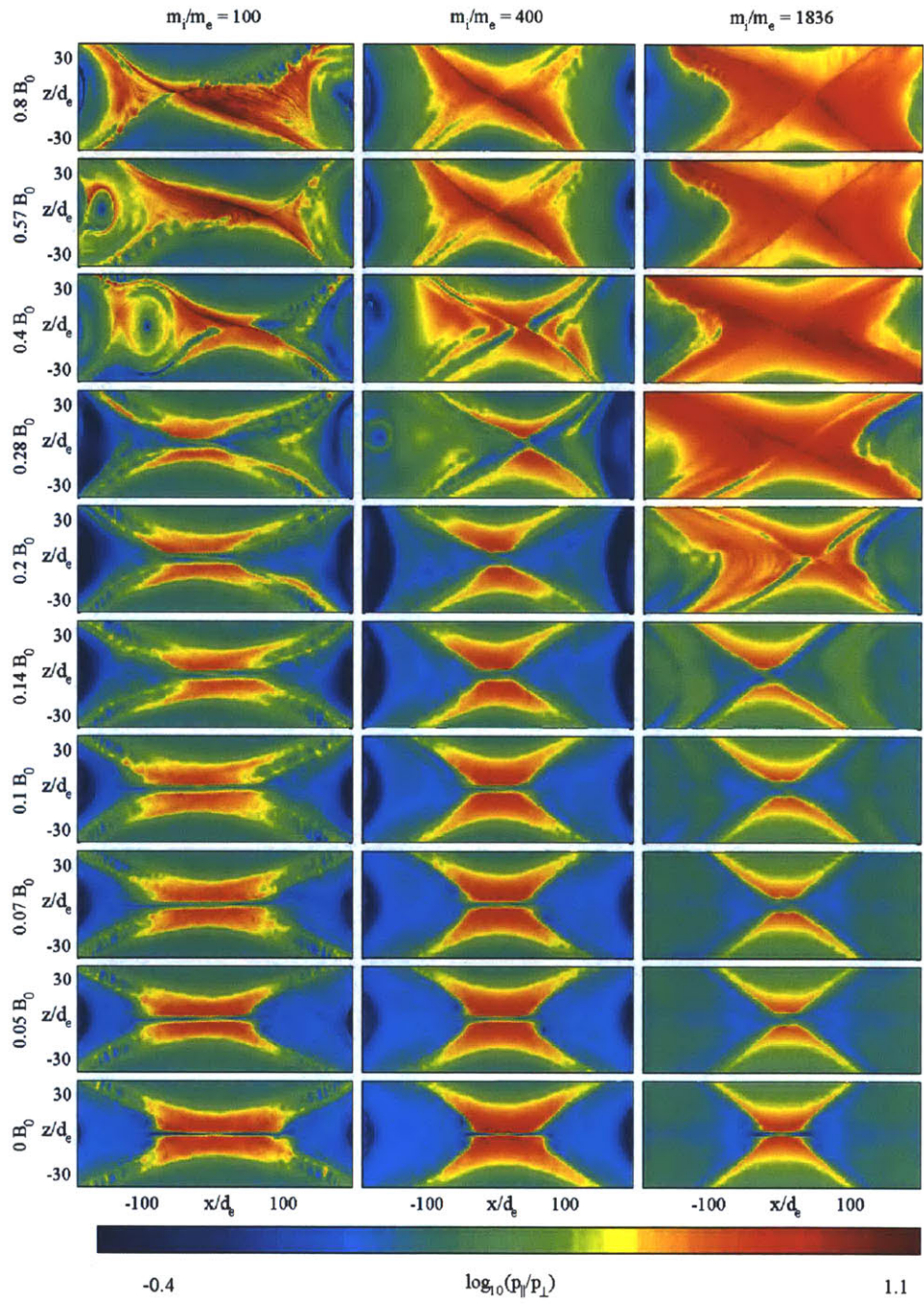


Figure 6-2: Electron pressure anisotropy p_{\parallel}/p_{\perp} .

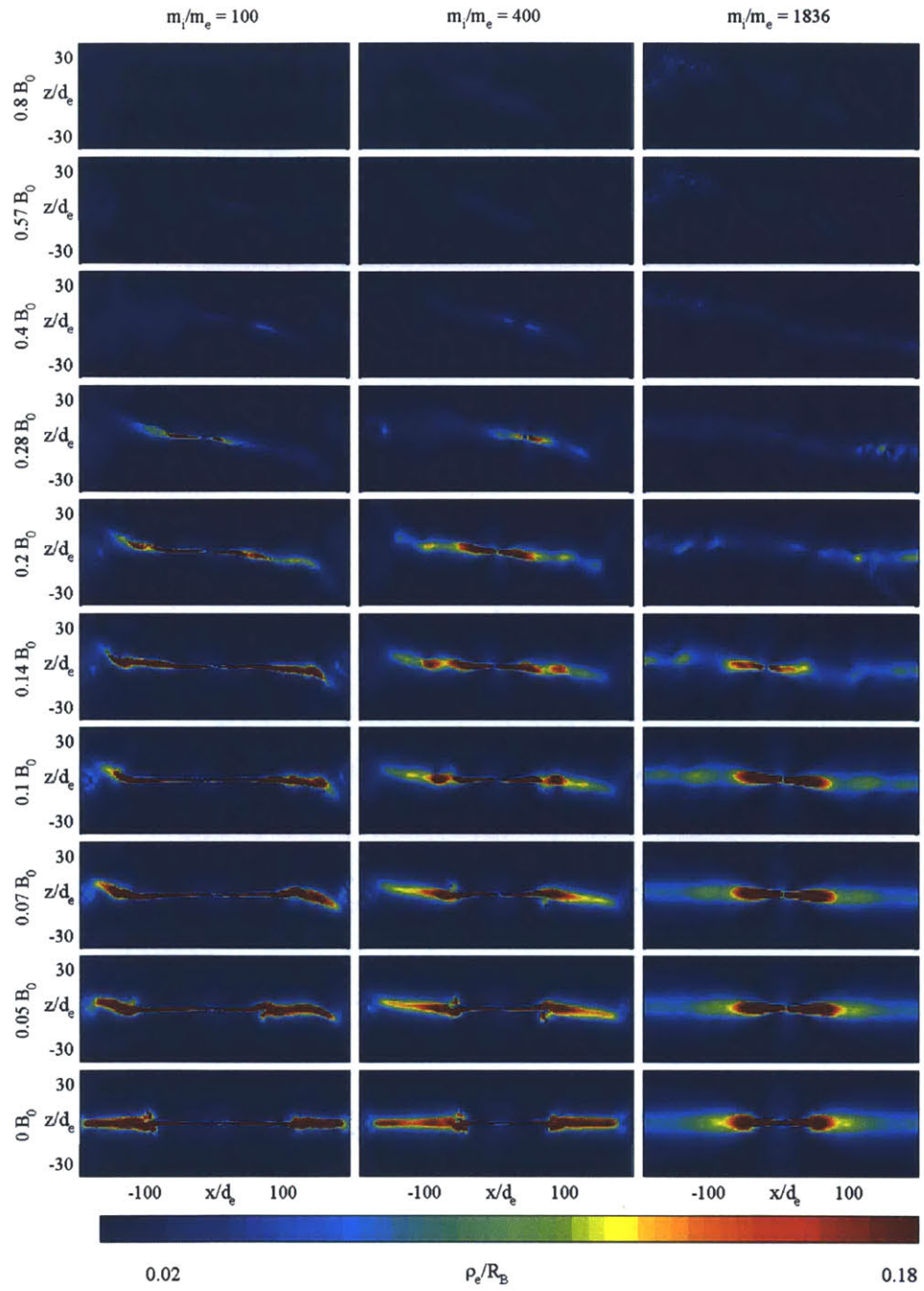


Figure 6-3: Ratio of electron Larmor radius to magnetic field radius of curvature, ρ_e/R_B .

proton mass ratio. This result is confirmed by the parameter scan performed on VPIC. The exhaust electron flow u_{ex} and out-of-plane flow u_{ey} from the simulations are plotted in Figs. 6-4 and 6-5. The inner electron jets are mostly deflected by a guide field as low as $B_g = 0.05B_0$ at the physical mass ratio $m_i/m_e = 1836$, although they form at $B_g = 0.14B_0$ even at a fairly high mass ratio of $m_i/m_e = 400$. Jets form at still higher guide fields at $m_i/m_e = 100$. Care must therefore be taken when comparing PIC results to detailed spacecraft observations, particularly because very few previous simulations employ realistic mass ratios.

As visible in Figs. 6-4 and 6-5, the inner electron jets form at very weak guide fields. Although the basic structure of the inner jets is similar to the anti-parallel case, the guide field does modify the electron currents. In particular, a portion of the guide field may be shielded from the region immediately around the X line by asymmetries in the electron current. Some details are described below, and they are based on the runs at $m_i/m_e = 400$. For this mass ratio, inner electron jets form up to a guide field of $B_g = 0.14B_0$. These runs correspond, at least qualitatively, to results at the proton mass ratio $m_i/m_e = 1836$ with guide fields $B_g \lesssim 0.05B_0$. Plotted in Fig. 6-7(a,b) is the pressure anisotropy p_{\parallel}/p_{\perp} for guide fields of $B_g = 0.05$ and $0.14B_0$. Consistent with the equations of state, it reaches $p_{\parallel}/p_{\perp} \sim 9$. The magenta contours in each case indicate where the electron pressure is nearly firehose unstable, with $p_{\parallel} - p_{\perp} - B^2/\mu_0 = \epsilon$ for ϵ chosen as 0.5% of the upstream magnetic pressure. The anisotropy drives the jets of outflowing electron current, plotted are plotted in Fig. 6-7(d,e), similarly to the exactly anti-parallel case.

In terms of the orbits of individual electrons, electrons oscillate across the inner layer when it forms. This type of bouncing trajectory, denoted a meandering orbit in Ref. [108] is similar to the ones plotted in Fig. 5-12. Following the results of Ref. [74], this class of electron orbits exists when the parameter $\rho_e/R_B \gg 1$. The values of ρ_e/R_B are re-plotted in Fig. 6-6 with the color scale altered to show runs for which ρ_e/R_B exceeds one. This condition empirically provides a good predictor for the existence of an inner electron jet.

At guide fields higher than $0.15B_0$ at $m_i/m_e = 400$, there is an abrupt transition

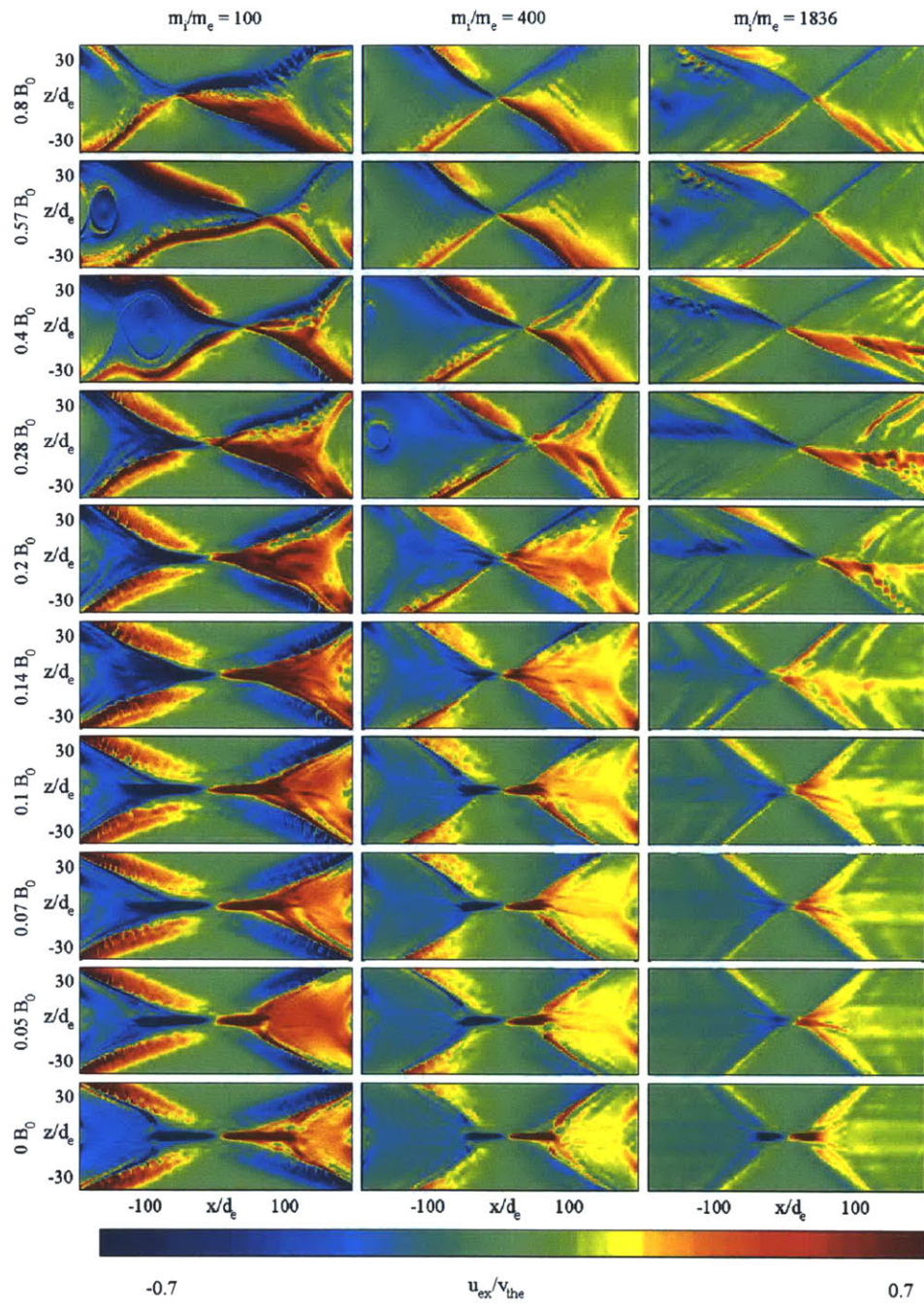


Figure 6-4: Exhaust electron flow u_{ex} normalized to thermal speed v_{the} .

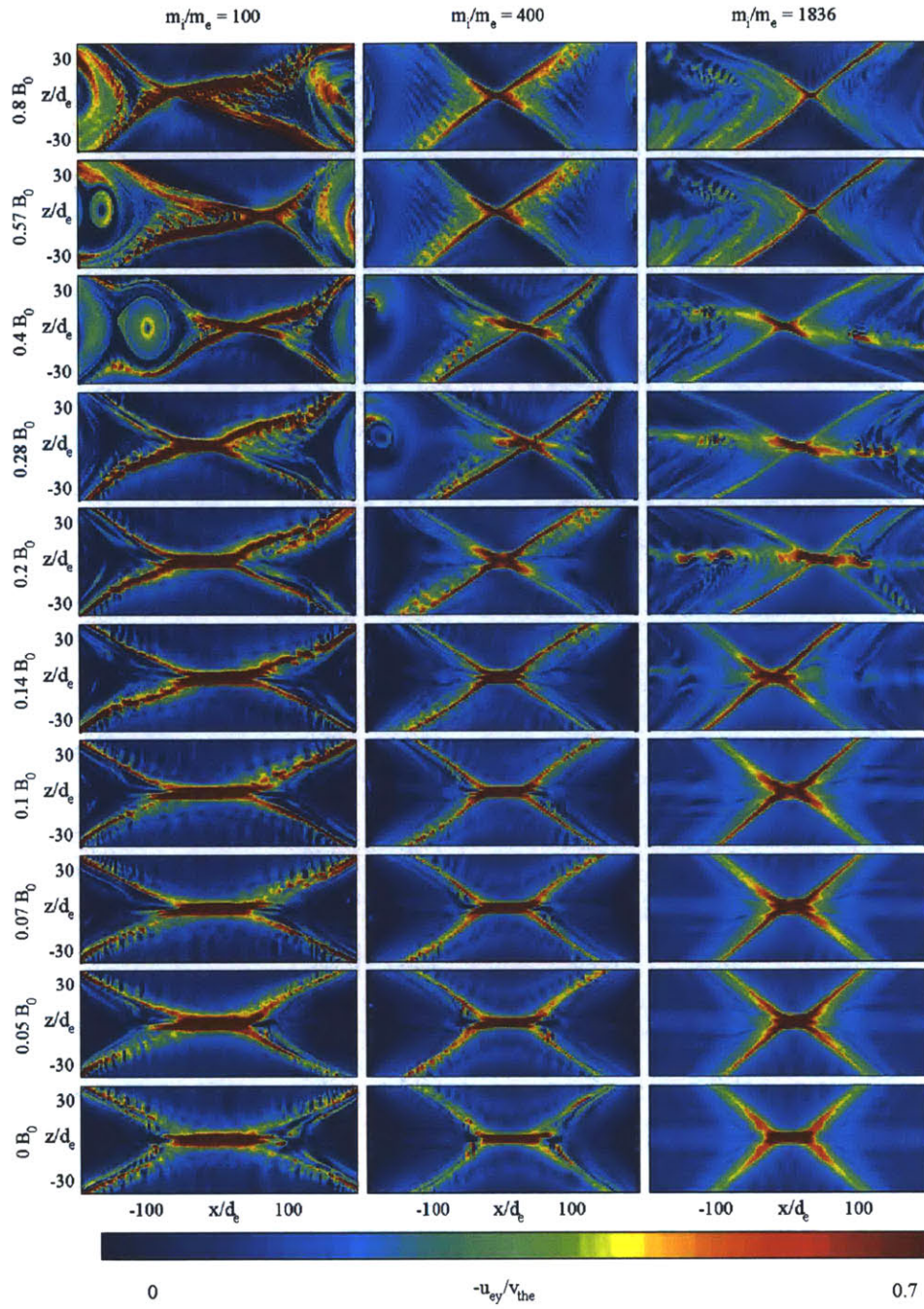


Figure 6-5: Out-of-plane electron flow u_{ey} normalized to thermal speed v_{the} .

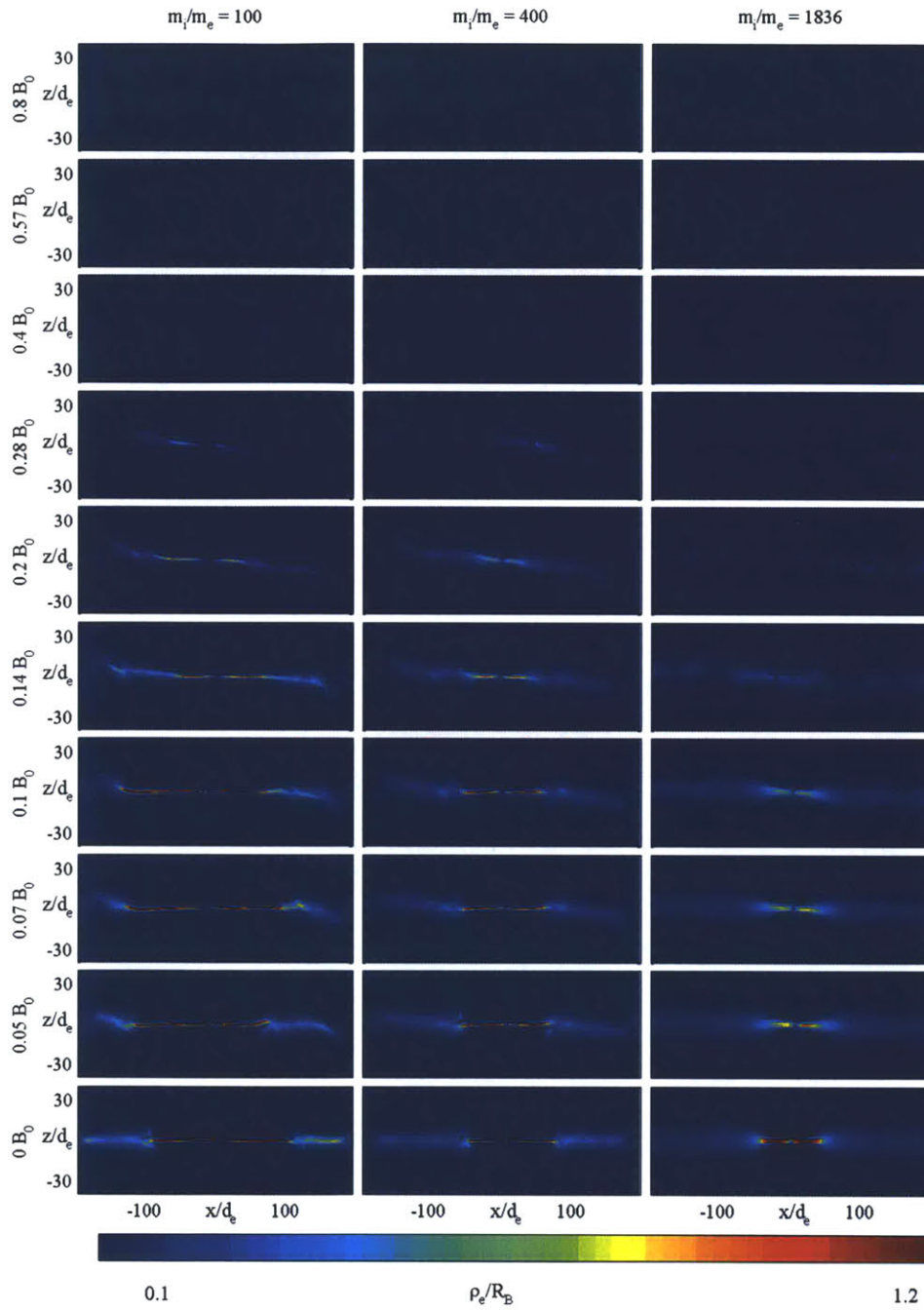


Figure 6-6: Ratio of electron Larmor radius to magnetic field radius of curvature, ρ_e/R_B . (Color scale altered.)

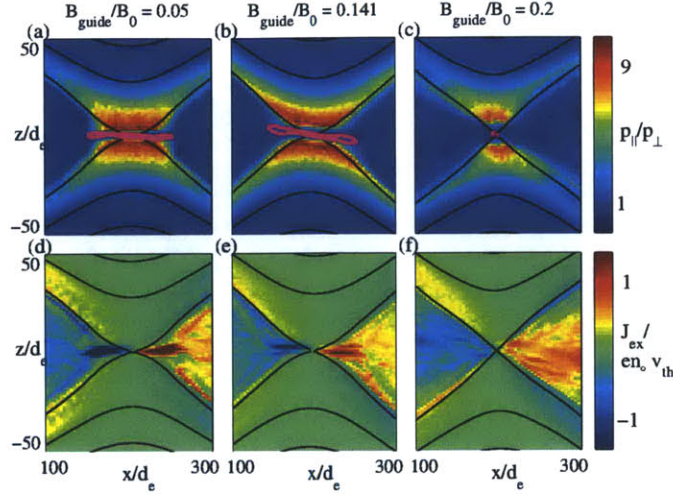


Figure 6-7: Pressure anisotropy and electron jets with varying guide magnetic fields ($m_i/m_e = 400$).

in the structure of the electron region around the X line. Specifically, the narrow inner electron layer does not form. This occurs well before the guide field is strong enough to magnetize the electron orbits at the reconnecting field reversal, as evidenced by the high values of ρ_e/R_B in Fig. 6-3. The values are not high enough, however, to enable electrons to follow bouncing orbits near the X line (See Fig. 6-6). Figure 6-7(c) shows results from the simulation with a guide field of $0.2B_0$, the lowest guide field for which an extended electron layer does not form at $m_i/m_e = 400$. Note also that the level of anisotropy is reduced, and the region of strong pressure anisotropy is shorter along the outflow and does not reach as far into the x-line region in the inflow. There is therefore practically no layer where the firehose condition is met, and there is no collimated electron outflow jet in this case [see Fig. 6-7(f)].

When they do form, the extended electron layer and jets leave observable traces in the magnetic and electric field profiles near the X line. Anti-parallel reconnection is marked by the emergence of characteristic Hall fields, in the form of a quadrupolar perturbation of the out-of-plane magnetic field B_y . If an electron jet forms, the out-of-plane magnetic field rapidly changes sign across the electron layer due to the current carried by the outflowing electrons. Indeed, the steep gradient in B_y at the center

of the electron diffusion region helped identify jets in data gathered by the Cluster spacecraft [107]. A similar magnetic field structure is observed for guide fields where an electron layer forms, as in Fig. 6-8(a) for $B_g = 0.14B_0$. In contrast, in Fig. 6-8(b) at the higher value of $B_g = 0.2B_0$ where no jets form, there is a relatively broad region of weak out-of-plane field.

In addition to a magnetic field perturbation, a strong inward pointing electric field E_z is associated with the electron region in anti-parallel reconnection. This electric field maintains quasineutrality by preventing an overabundance of electrons from accumulating within the electron layer. The electric field E_z in Fig. 6-8(a), where a guide field of $0.14B_0$ is included, has a structure almost identical to that of purely anti-parallel reconnection. At higher guide fields, however, the electron layer is absent and the electric field profiles lack the signature extended formation [Fig. 6-8(d)].

In exactly anti-parallel reconnection, the outer part of the Hall current loops J_{ex} are carried almost purely by electron flows parallel to the magnetic field. With the addition of a guide field B_y , however, there are additional electron currents in the x direction. Perpendicular $\mathbf{E} \times \mathbf{B}$ motion arises due to the out-of-plane field B_y crossed with the intense electric field normal for the electron layer E_z . The ions are unmagnetized on the length scales of the layer, and the electron $\mathbf{E} \times \mathbf{B}$ motion therefore results in a net electrical current. Figure 6-9(a) shows the electron current J_{ex} along a cut $20d_e$ to the right of the x-line in a simulation of exactly anti-parallel reconnection. The parallel component of this flow is also shown, and it accounts for essentially all of J_{ex} . With a guide field $B_g = 0.14B_0$, on the other hand, the $\mathbf{E} \times \mathbf{B}$ motion cancels some of the parallel current on one side of the electron layer as illustrated in Fig. 6-9(b). In particular, the currents that would add to the external guide field are reduced, and this is the main mechanism for expelling guide field from the x-line. The inner electron jets thus form at very weak guide fields, although a weak guide field breaks a symmetry of the layer and distorts the electron current distribution somewhat. As noted in Ref. [104], however, there are major discrepancies when the physical proton mass ratio is implemented that are hard to reconcile with

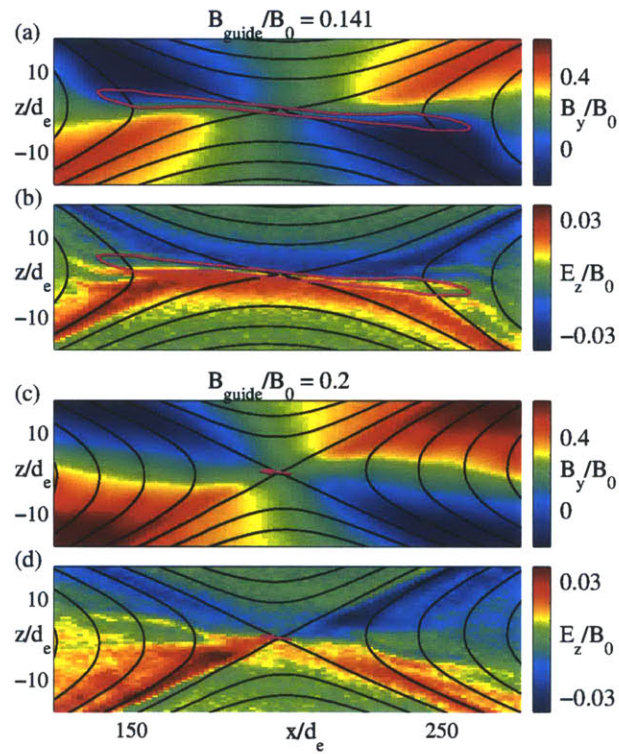


Figure 6-8: Hall electric and magnetic fields above and below the guide field threshold for jet formation.

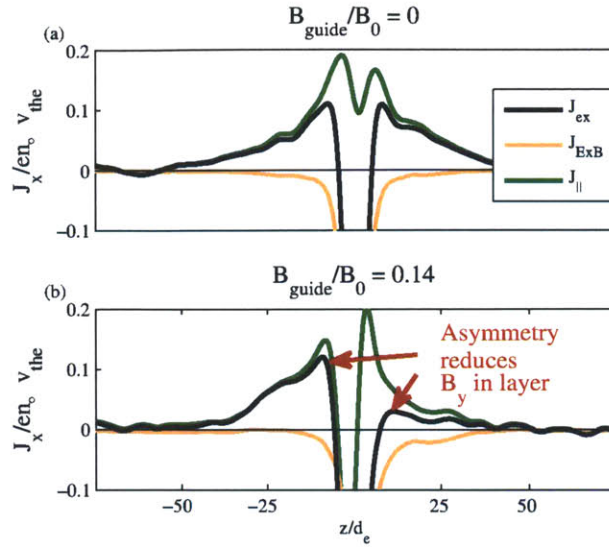


Figure 6-9: The Hall currents become asymmetric in the presence of a guide field.

Cluster observations [107] for example.

At the higher physical mass ratio, the electrons remain magnetized even for relatively weak magnetic fields. In fact, a new regime that may be more relevant to the spacecraft observations opens up when the physical proton-to-electron mass ratio is implemented. For this intermediate guide field, the reconnection exhaust includes very long magnetized electron current layers. At guide fields of $\sim 15 - 50\%$ of the upstream reconnecting field, a long electron current layer develops embedded within the exhaust. The electron outflow velocity u_{ex} and out-of-plane velocity u_{ez} from the proton mass ratio run with a guide field of $B_g = 0.28B_0$ are plotted in Fig. 6-10. While the inner electron layers are typically localized to regions $\lesssim 100d_e$ long, the new magnetized current layers at $m_i/m_e = 1836$ become $> 600d_e \sim 15d_i$ long and are limited in the present runs by the size of the simulation domain. As noted previously in this chapter, the Cluster spacecraft gathered evidence for an extended electron layer in the magnetosheath of $> 60d_i$ in length [107]. Based on the current scan of parameters, it is more likely that that current layer was of the type described here, rather than an extremely long inner electron layer.

In the regime identified here, the equations of state hold in the exhaust, and it

is therefore possible for the electron pressure to remain anisotropic where the magnetic field is relatively low. The result is an extended region where the electrons are close to the firehose stability threshold. The electron pressure anisotropy normalized to (twice) the magnetic pressure, $(p_{\parallel} - p_{\perp})/(B^2/\mu_0)$, is also plotted in Fig. 6-10. The value one corresponds to the marginal firehose condition, where electron pressure anisotropy balances magnetic field tension. Following the results of Cowley in Ref. [92], a 1D steady state current sheet with a normal magnetic field is only possible if the upstream plasma is marginally firehose unstable. Insofar as the elongated electron layer is almost 1D (with an aspect ratio of ~ 60) and quasi-steady state, it is reasonable that the current layer can only be sustained when the electrons are nearly firehose unstable. The equations of state, and the heating mechanism on which they are based, describe how this layer of strong anisotropy forms as a natural part of the reconnection process.

At stronger guide fields, the reconnection geometry takes on the features presented in the chapter devoted to the strong guide field regime. The equations of state continue to hold in the exhaust, and the electron pressure typically becomes highly anisotropic. When the guide field is strong enough, however, the electron pressure does not overtake the tension of the guide magnetic field and it does not reach the marginal firehose condition $p_{\parallel} - p_{\perp} - B^2/\mu_0 \approx 0$. This prevents the formation of an elongated electron layer embedded in the center of the exhaust. Rather, the electron outflow tends to align with a pair of diagonally opposed separators. In the lower panels of Fig. 6-4, these are the enhanced electron flows along the top left and bottom right separators. The pair of separators that exhibits enhanced currents is the one where the density is larger. (See the density profiles are plotted in Fig. 6-1.) The increased density is related to ion polarization drifts [109], and if the direction of the guide magnetic field is reversed, the opposite pair of separators will therefore have enhanced density and electron currents.

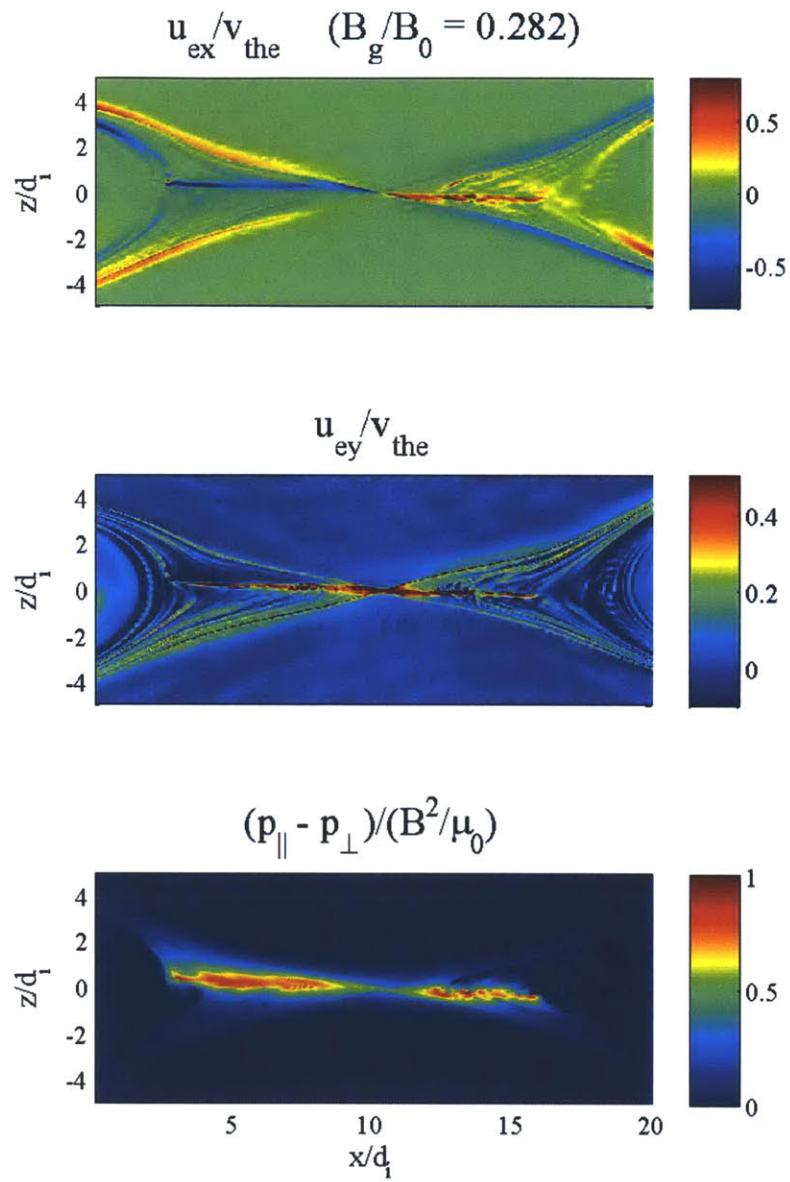


Figure 6-10: New type of magnetized electron jet driven by pressure anisotropy (at physical proton mass ratio and $B_g = 0.282B_0$).

Summary. The diagram in Fig. 6-11 summarizes schematically where the various regimes for the electrons lie in the space of guide fields and mass ratios. Four qualitatively different regimes are identified:

(1) At the lowest guide fields, inner unmagnetized electron current layers develop, and they are depicted symbolically in Fig. 6-11. Electrons may follow meandering orbits near the X line because $\rho_e \gtrsim R_B$. Note that while inner jets form even at substantial guide fields for reduced mass ratios, the inner jets only form in very nearly anti-parallel magnetic geometries at the physical proton mass ratio. The exhaust is isotropic because the electrons are not magnetized near the magnetic field reversal.

(2) At a threshold guide field that depends on the mass ratio, inner electron jets do not form. The the exhaust electron pressure, however, may continue to be isotropic.

(3) The electron Larmor radius becomes smaller relative to the current sheet width at higher mass ratios. As a result, the equations of state apply in the exhaust for lower guide fields B_g at higher mass ratios m_i/m_e . In fact, by $B_g/B_0 \sim 0.2$ the equations of state provide a good approximation of the electron pressure tensor at the proton mass ratio $m_i/m_e = 1836$. For the proton mass ratio, the electron exhaust may remain magnetized even with fairly weak guide fields. A new regime exists in which electron pressure anisotropy supports a very long magnetized current layer, near which the electron pressure approaches the firehose instability threshold.

(4) At the highest values of B_g , the electron pressure cannot compete with the tension of the guide field. The long magnetized current layers do not form, and the electron outflow tends to be concentrated along one pair of diagonally opposed separator field lines.

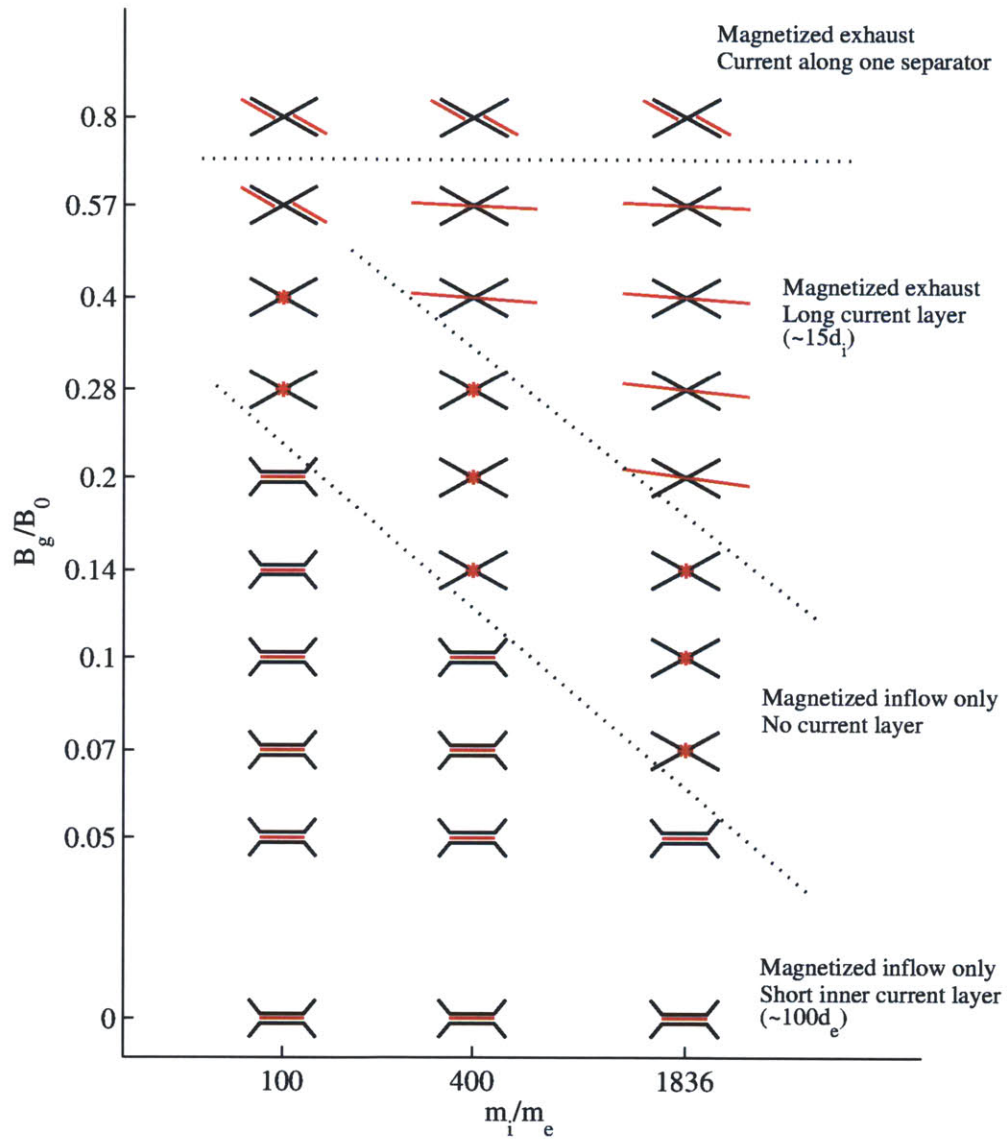


Figure 6-11: Reconnection regimes for different guide fields and mass ratios m_i/m_e .

Chapter 7

Extensions

The previous simulation results were based on the Harris sheet configuration. This configuration has symmetric plasma conditions above and below the plasma current layer. The additional 2D symmetry of the evolution is imposed so that the problem is amenable to direct computation. In this chapter, these symmetries are relaxed. First, cases with a density difference across the plasma layer are considered. Next, fully 3D evolution is allowed by moving to 3D volumetric simulation. Finally, an entirely different initial geometry is considered that is based on two magnetic islands. While the Harris equilibrium depends only on one spatial variable, the island equilibrium is 2D and the unstable current sheet forms as a natural result of island motion and merging.

The equations of state are based on fairly general electron orbit properties. Asymmetries in the plasma conditions enter in the boundary conditions placed on the electron distribution. Although this makes the application of the equations of state less straightforward, electron trapping and its resulting pressure anisotropy are important effects also in asymmetric kinetic reconnection. The equations of state also rely on assuming that magnetic field lines extend into an ambient ideal plasma. For island merging, this topological assumption is not necessarily met. It turns out, however, that the electrons in regions around the X line are still largely governed by the parallel potential. The equations of state therefore also lay a foundation for modeling anisotropy during island coalescence.

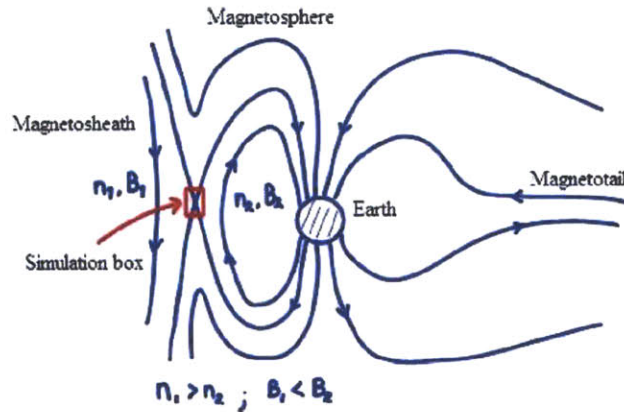


Figure 7-1: Magnetopause reconnection geometry.

7.1 Asymmetric Current Sheets

In the Harris sheet simulations in the previous chapters, the plasma conditions are identical above and below the initial current sheet. Asymmetries in the plasma density and the magnetic field strength across the plasma sheet, however, are not uncommon. At Earth's magnetopause, for example, the density is typically one or two orders of magnitude higher on the magnetosheath side than the magnetosphere side (the geometry is drawn in Fig. 7-1 reproduced from Ref. [71]). Reconnection has long been recognized to occur at the magnetopause due to the interaction of Earth's magnetic field with the variable solar wind magnetic field [110]. In a series of magnetopause crossings by the THEMIS spacecraft when reconnection signatures were detected, the magnetosheath plasma had a density of 10 – 30 times larger than the magnetospheric plasma density [111]. Also in the geotail, which is often nearly up-down symmetric near the plasma sheet, there can be significant density asymmetries. The Wind spacecraft in the distant ($\sim 90R_E$) geotail observed evidence for reconnection with a small magnetic field asymmetry of $\sim 15\%$, but a large density asymmetry of $n_{up}/n_{down} > 10$ [112].

Large asymmetries in the plasma conditions will alter the magnetic geometry and currents of the reconnection region. Some initial investigations of 2D asymmetric

reconnection within a fluid framework found that generally the X line and flow stagnation point are spatially separated. Scalings for various quantities were derived using an analysis similar to that of Sweet and Parker [113] and were generalized to include compressibility [114]. Kinetic simulations further showed that electron pressure effects are not necessarily localized to d_e length scales [115], but rather they may extend across the density gradient.

A key result for asymmetric reconnection is the fact that the electron heating and pressure anisotropy are usually larger on the magnetosphere side of the magnetopause, where the density is lower and the magnetic field strength is greater [71]. This is consistent with the general prediction of the equations of state for weak guide field reconnection that the parallel potential and the resulting electron heating are larger in small β_e plasmas. The parallel potential and the electron pressure anisotropy are plotted in Fig. 7-2. The simulations also demonstrate that the parallel potential on reconnected magnetic field lines has a net drop across the magnetopause. The parallel electric field tends to point towards the lower-density magnetosphere. This slows the flux of electrons from the high-density magnetosheath into the low-density magnetosphere.

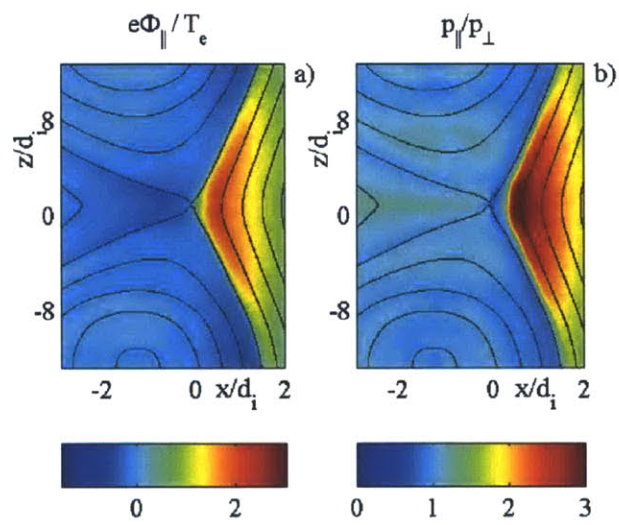


Figure 7-2: Parallel potential and electron pressure anisotropy during asymmetric reconnection.

7.2 Reconnection with Fully 3D Evolution

The previously presented PIC simulations are all 2D with an assumed translational symmetry in the out-of-plane direction. Reconnection in nature, however, is 3D. The importance of gradients in the third direction will vary depending on the plasma geometry, but in any case, accounting for 3D evolution greatly complicates descriptions of reconnection. Even defining reconnection in 3D is problematic. The topology of 3D field lines is vastly more complex than in the 2D case, where the field lines always lie on neatly arranged flux surfaces. Nevertheless, reconnection certainly occurs in 3D, and it has been studied experimentally by considering the interaction of plasma flux ropes [39]. VTF experiments demonstrated that even in a nearly-axisymmetric toroidal device, the inherently 3D structures that develop can be crucial for the onset of reconnection [33].

The magnetic field of the solar corona is 3D and rather complex, and its topology has long been studied [116]. The topology may be characterized by the magnetic skeleton, which consists of the magnetic nulls (points where the total magnetic field $\mathbf{B} = 0$) and the spine field lines that connect them [117]. These are 3D analogs of the X line, which is a 2D structure that is not stable in 3D. An isolated magnetic null has been detected in association with geomagnetic activity in Earth's magnetotail based on simultaneous data from the four Cluster spacecraft [118]. Reconnection in 3D, however, can also occur without a magnetic null. The magnetic geometry, particularly the shearing rate or how fast the magnetic field changes direction across a layer of plasma current, is at least as important as the field line topology. The notion of a quasi-separatrix layer [119] was introduced to describe layers of intense magnetic shear that are unstable to reconnecting instabilities. Quasi-separatrix layers have been identified during reconnection in linear plasma experiments [120].

PIC simulations of 3D reconnection with well-separated ion and electron masses have become feasible within the past couple of years. Kinetic electron dynamics in collisionless reconnection play a large role in determining how 3D current sheets reconnect [63]. Particularly when there is a guide magnetic field, the current sheet is

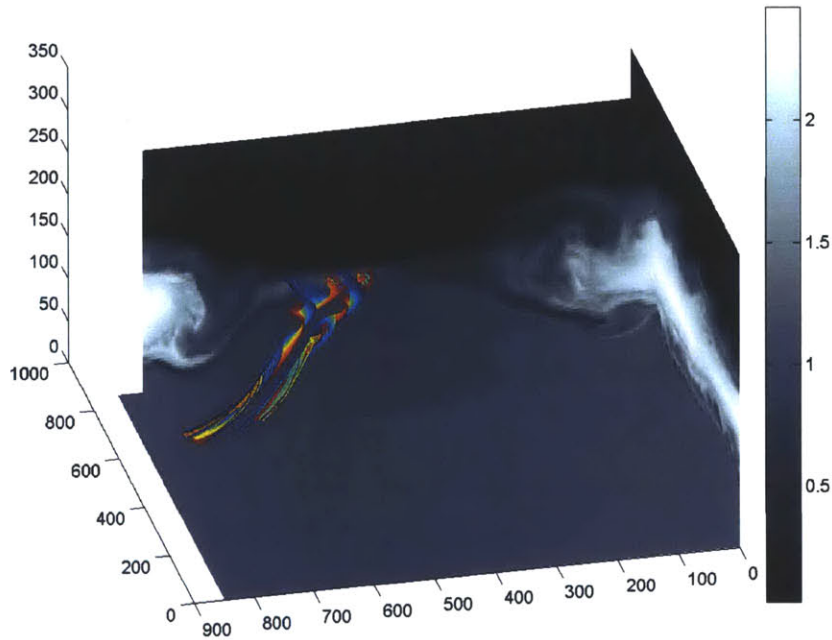


Figure 7-3: Two fluxropes in a 3D PIC simulation.

unstable to a number of reconnecting modes. In 2D, the main tearing instability will result in a set of magnetic islands around the center of the initial current sheet. In 3D, the current breaks apart into flux ropes of finite length that may lie at oblique angles to the initial current. The flux ropes are coherent vortical magnetic structures sustained by electron currents. A pair of flux ropes, from a large-scale VPIC simulation of 3D reconnection provided by Daughton, is illustrated in Fig. 7-3.

The electron current layers and flux ropes that form during 3D reconnection are affected by the electron pressure anisotropy. In the 2D case, the anisotropy drives narrow electron current channels. These may be susceptible to 3D instabilities. The equations of state make no assumption about the dimensionality of the magnetic field, and they may be expected to hold also in 3D. Two tests of the equations of state in a 3D reconnection simulation with a strong guide field are presented in Figs. 7-4 and 7-5.

This simulation uses a mass ratio of $m_i/m_e = 100$ because higher mass ratios in 3D currently require prohibitively long computation times. The mass ratio is high

enough for adiabatic electron trapping to occur, and the electron pressure becomes highly anisotropic. The ratio p_{\parallel}/p_{\perp} is plotted in Fig. 7-4 both directly from the PIC simulation and based on evaluating the equations of state using the PIC density n and magnetic field strength B as input. In either case, the ratio reaches $p_{\parallel}/p_{\perp} \sim 4$. Two different slices of the 3D simulation are plotted. The top two plots come from a slice at $y = 41d_e$ (the simulation box is a total of $700d_e$ long), and the region of strongest anisotropy is along diagonally opposed field lines similar to a 2D case. The bottom two plots are from another slice at $y = 410d_e$, and here the large flux rope structure is apparent. In 2D, the island would be of infinite extent. In this 3D case, the island has a finite length in the initial current direction and does not appear in the top slices at $y = 41d_e$. An important implication is that electrons in the flux rope structure may escape along field lines, while electrons in 2D magnetic islands are confined within the island.

As additional verification that the electron pressure obeys the equations of state, Fig. 7-5 shows p_{\parallel} and p_{\perp} evaluated on isosurfaces of magnetic field strength. Following the equations of state, each should then be only a function of the density. The PIC data from isosurfaces are two different values of the magnetic field ($B = 0.85$ and $1.15B_{\infty}$) are plotted as functions of the density n , and the predictions of the equations of state are also plotted. The PIC data are more scattered in 3D than in 2D, likely because of turbulence that is only possible in 3D and because field lines may connect regions that initially had different plasma conditions. The equations of state, however, capture the general scaling of the pressure components and provide good estimates for the total pressure anisotropy.

The above simulation is a symmetric reconnection study. The equations of state also reproduce fairly well the electron pressure anisotropy that develops in 3D simulations of asymmetric reconnection. Results from a 3D reconnection simulation with a density asymmetry of 10 are presented below. As in the 2D case, the strongest anisotropy and most significant populations of hot electrons tend to reside on the low β_e side of the current sheet. Fig. 7-6 shows a test of the equations of state in a 3D asymmetric VPIC run. Slices of the pressure ratio p_{\parallel}/p_{\perp} within the simulation

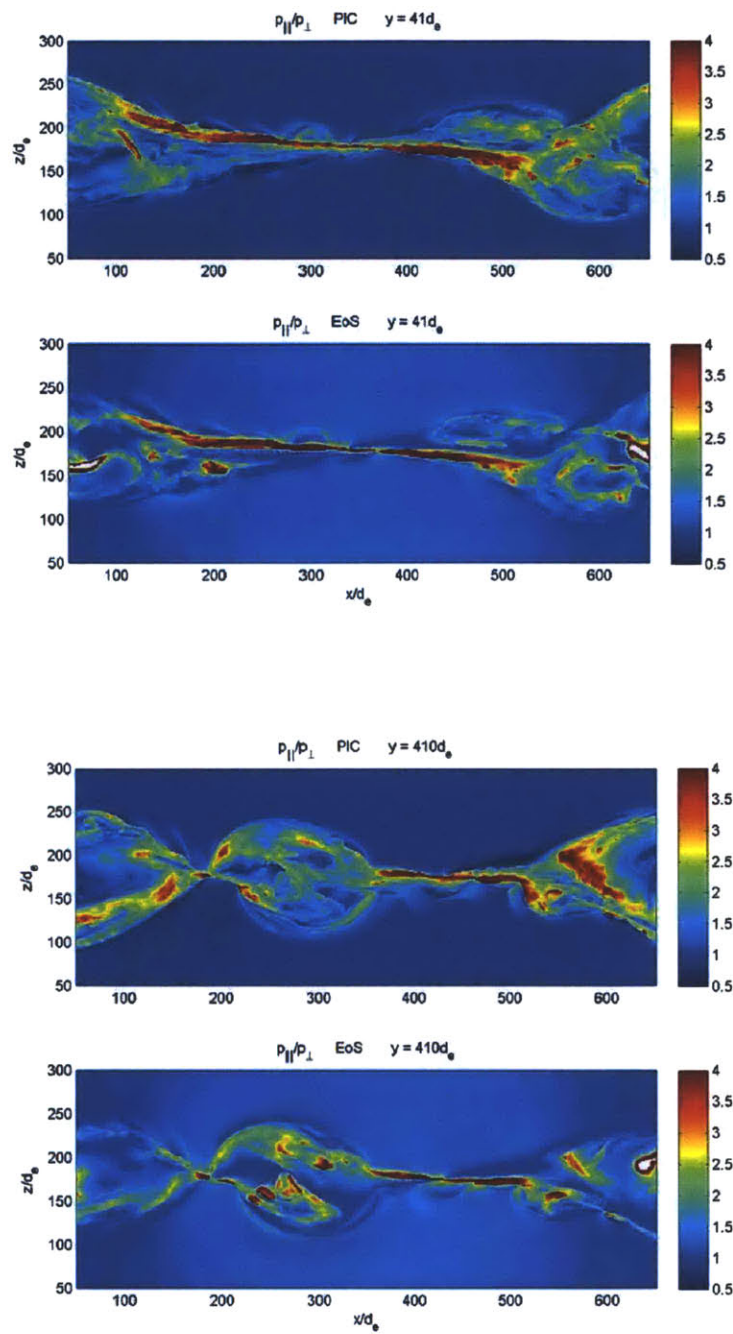


Figure 7-4: Ratio p_{\parallel}/p_{\perp} in a 3D PIC simulation.

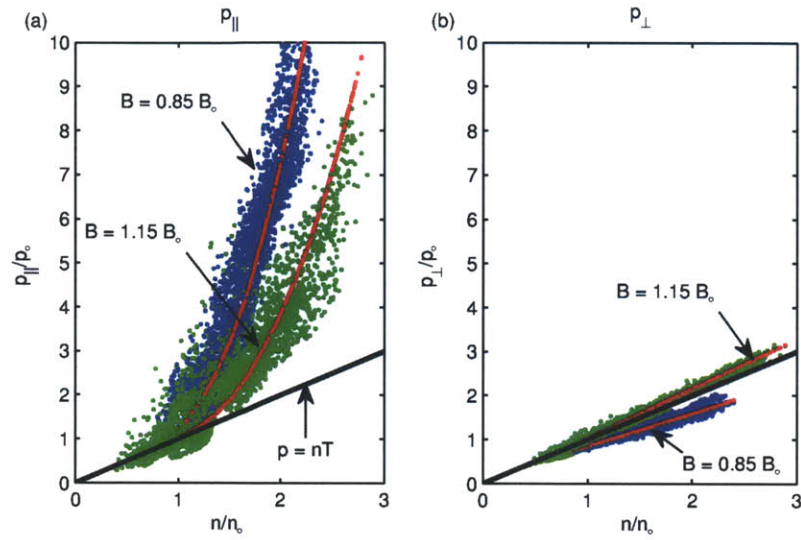


Figure 7-5: Test of the equations of state in 3D on isosurfaces of magnetic field strength. Pressure moments from the PIC data (green and blue) are compared to predictions of the equations of state based on the PIC density and magnetic field strength.

volume are drawn, and a cut through the initial symmetry direction is selected. This cut lies in the magnetospheric, low β_e portion of the domain. The predictions of the equations of state for the electron pressure tensor components based on the PIC density and magnetic field strength are plotted along this cut superimposed on the direct PIC results. In agreement with the equations of state, the parallel pressure rises to ~ 6 times its ambient magnetospheric value and the ratio of pressure components reaches $p_{||}/p_{\perp} \sim 3$.

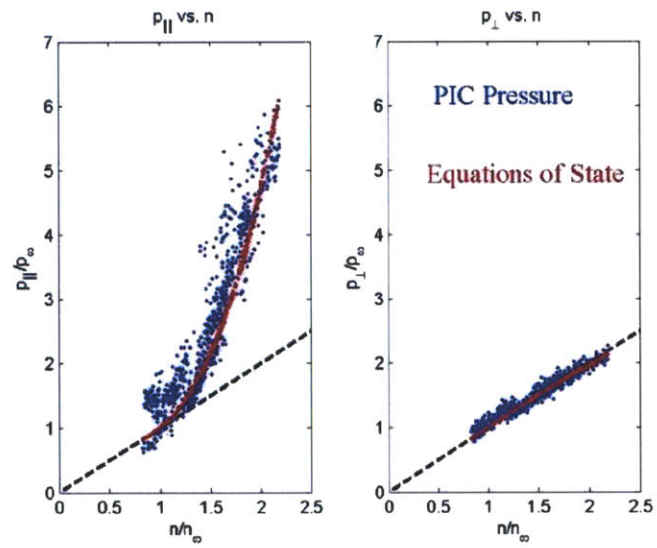
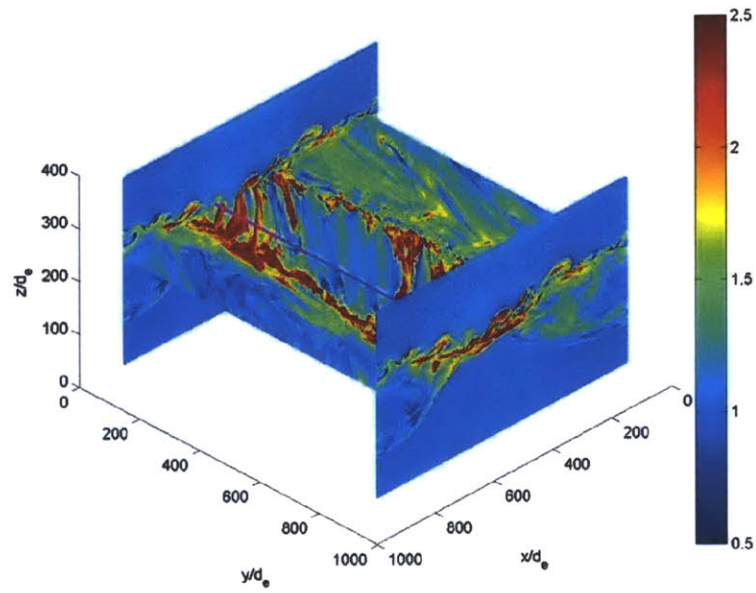


Figure 7-6: Test of the equations of state during 3D reconnection with asymmetric density.

7.3 Island Merging

In many environments, reconnection is time dependent and leads to formation of plasmoids or islands. In fact, current understanding of reconnection both in the collisionless and collisional regimes indicates formation of many interacting secondary islands [67, 121]. Observational evidence of plasmoid interaction comes from coronal mass ejections (CMEs) in the interplanetary medium. Interestingly enough, observations exhibit evidence of energetic electron generation when CMEs merge [122]. Since the plasma beta within CMEs is typically small, it was suggested that the heating mechanism captured by the equations of state are likely important for producing energetic electrons [123].

In non-ideal plasmas, magnetic islands may also merge to form larger islands. This process necessarily involves magnetic reconnection, and island merging releases magnetic energy into the plasma in the form of bulk flows and thermal energy. A large current sheet may be unstable to the plasmoid instability, which tears large systems into a series of multiple current filaments or plasmoids [124, 125]. These plasmoids may then merge, and additional electron heating takes place as the magnetic island field lines reconnect. Such large, unstable current sheets may form during solar flares. As the flare emerges, reconnection may occur at the underlying coronal loop. An observational signature of the resulting electron heating is the X-ray emission at coronal loop tops during flares [9]. The flare motion may induce a large current sheet in its wake. This current sheet may then filament into multiple magnetic islands [126], and the islands can merge as the bulk flows convect them towards one another [127]. A cartoon of this scenario is reproduced in Fig. 7-7. In addition, coronal mass ejections may collide in the interplanetary medium, and radio bursts associated with energetic electrons have been observed as the CMEs interact [122].

In applying the equations of state to island merging, a new complication arises. In the previous cases based on Harris sheet reconnection, the field line topology is open. As a result, the integral defining the parallel potential Φ_{\parallel} could be continued out to the edge of the simulation domain. The major difference is in the topology of the

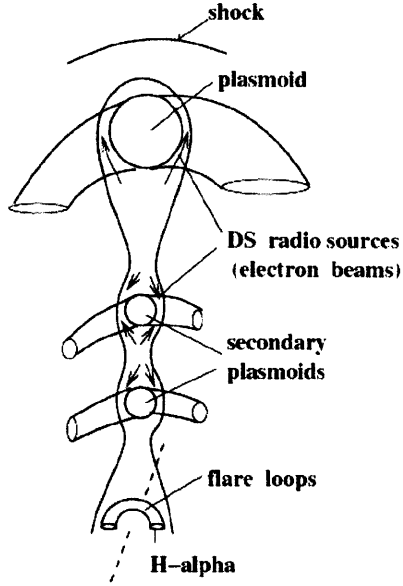


Figure 7-7: Cartoon of plasmoids formed in the corona (reproduced from Ref. [127])

magnetic surfaces, which in this case are closed and do not extend out to an ambient ideal plasma. In principle, Φ_{\parallel} is an integral along field lines and could be ill-defined in the case of closed field lines. And in fact, due to non-vanishing loop voltages, Φ_{\parallel} is formally not single-valued. It turns out, however, that localized structures develop in Φ_{\parallel} , and the adiabatic heating of trapped electrons in these local parallel potential wells plays an important role in magnetic island coalescence. A PIC simulation of island merging, performed on the code VPIC by Karimabadi [123], demonstrates that a localized acceleration potential Φ_{\parallel} can exist on closed field lines, and the heating mechanism studied previously in open topologies operates also in closed topologies.

To study island merging numerically, there are two commonly used sets of initial conditions. One is a Harris sheet with an imposed initial perturbation that causes tearing with multiple O and X points. The islands centered on the O points may then interact. The simulation presented here is initialized with a Fadeev equilibrium [128, 129], which is a 2D exact equilibrium. The magnetic field follows from a vector potential given by

$$A_y = A_{y0} \ln[\cosh(kz) + \epsilon \cos(kx)], \quad (7.1)$$

and it consists of a chain of magnetic islands along the x axis. The plasma pressure is generally higher within the islands, and pressure balance is achieved in the simulation by increasing the plasma density inside the islands. This simulation uses periodic boundary conditions in the x direction and covers two of the initial islands. They are shown in Fig. 7-8. The plasma current and density are peaked within the islands, and the current filaments attract one another and eventually merge. During this process, significant electron heating occurs at the X line between the two islands. The other time slices in Fig. 7-8 show the islands after reconnection has begun and after the islands have almost completely merged. At the end of the island merging simulation, $\sim 16\%$ of the dissipated magnetic energy goes into heating the electrons ($\sim 64\%$ goes into heating the ions, $\sim 18\%$ is carried by ion flows). Because the density of the background is low, the vast majority of this energy is gained by electrons near the islands.

To investigate whether trapping in a parallel potential Φ_{\parallel} is important during island merging, the values of Φ_{\parallel} are calculated from the electromagnetic fields of the PIC simulation. The values of Φ_{\parallel} obtained in the PIC code are plotted in Fig. 7-9(a), which shows the region around the X line between the two merging islands. The parallel potential Φ_{\parallel} is enhanced along two diagonally opposed separators, a structure characteristic of reconnection in the presence of a guide magnetic field and observed in a previous chapter on strong guide field reconnection. In these regions of higher density, $\Phi_{\parallel} \sim 5T_{e0}$, implying that nearly all of the thermal electrons here follow trapped orbits. Both the spatial structure and the magnitude of the potential are consistent with the increased parallel electron temperature, which peaks at $T_{e\parallel} \sim 4T_{e0}$ and is plotted in Fig. 7-9(b).

The phase space density of electrons as a function of energy $f(E)$ for pitch angles parallel and perpendicular to the magnetic field at the point marked by a dot in Fig. 7-9 is plotted in Fig. 7-10(a). The energy distribution is characteristic of particles trapped in a parallel potential, and it agrees with the form in Eq. 2.7. The perpendicular distribution is a Maxwellian. The parallel spectrum, meanwhile, is fairly flat up to an energy of $E \sim e\Phi_{\parallel} \sim 4T_{e0}$ and then falls off as a shifted Maxwellian.

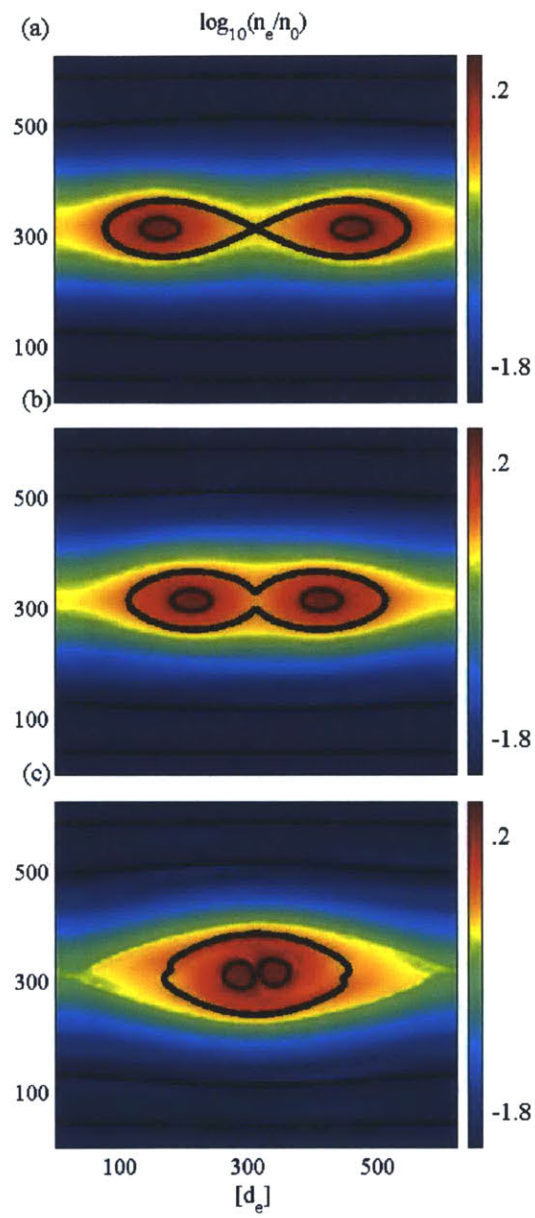


Figure 7-8: Magnetic island coalescence: density and sample field lines.

Another feature of this closed geometry is the generation of a cool core surrounded by a warmer plasma. Spectroscopic measurements suggest the presence of similar configurations during some solar CMEs [130]. Hotter plasma surrounds the cooler island in the simulation as magnetic flux is reconnected and the heated trapped electrons are convected away from the X line. Once downstream, the exhaust electrons can stream along field lines and fill the regions outside the magnetic islands. Over the course of the simulation, a thermal electron freely streaming along the magnetic field lines could encircle a single island 3 – 4 times. As visible in Fig. 7-9(b), the temperature in the volume of plasma surrounding the islands is roughly twice the island temperature.

The equations of state for the parallel and perpendicular electron pressure tensor components are also tested. In the previous Harris sheet reconnection scenarios, the electron pressure near the X line becomes anisotropic with $p_{\parallel}/p_{\perp} > 1$. This is also the case near the X line between the merging islands. The predictions of the equations of state are compared to the PIC simulation results in Fig. 7-9(c-d). Because some of the electrons were pre-heated before becoming trapped in the pictured time-slice, the ambient temperature anisotropy of $p_{\parallel}/p_{\perp} \sim 2$ was taken into account in the boundary conditions used in the equations of state. The good agreement between the equations of state and the PIC output reflects the fact that particle trapping in Φ_{\parallel} is largely responsible for the electron heating between the islands.

Following the results of [70], the value of Φ_{\parallel} and the resulting electron energies depend strongly on the upstream electron β_e . For the simulation parameters in the plasmoids upstream of the X line, this has a value of $\beta_e \sim 10\%$. Meanwhile, values of $n_e \sim 10^{10} \text{ cm}^{-3}$, $T_e \sim 10^6 \text{ K}$, and $B \sim 10 \text{ G}$ more typical of the solar corona give a lower value of $\beta_e \sim 0.1\%$. Although the precise scaling of [70] is based on reconnection without a guide field, the general trend is expected to carry over into regimes with guide fields. The peak electron parallel temperature $T_{e\parallel}$ should therefore be substantially greater at the lower values of β_e more typical of the solar corona. In fact, in recent simulations of reconnection in a low β_e plasma, bulk electron energization occurs up to $\sim 100T_{e0}$ [98]. Acting near even a single X line, this heating

mechanism could therefore heat the bulk coronal electrons into the 10s of keV range. In a multi-plasmoid scenario [131], repeated acceleration at multiple X lines could produce electrons with even higher energies.

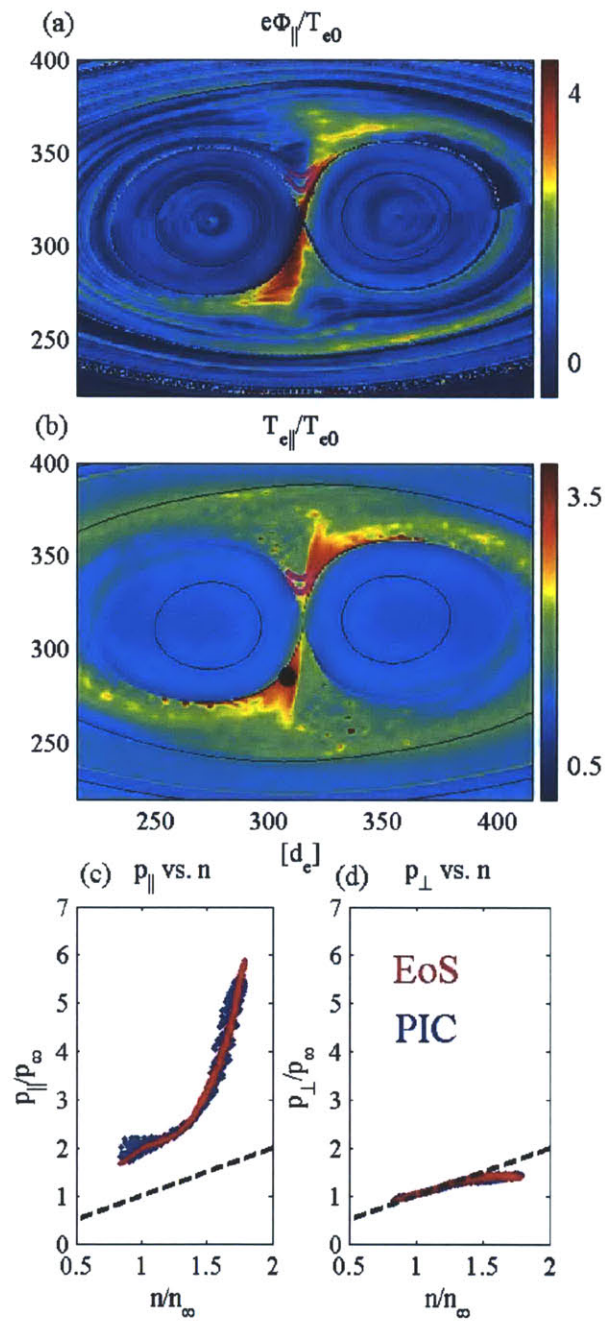


Figure 7-9: Parallel potential and temperature, and equations of state between merging magnetic islands.

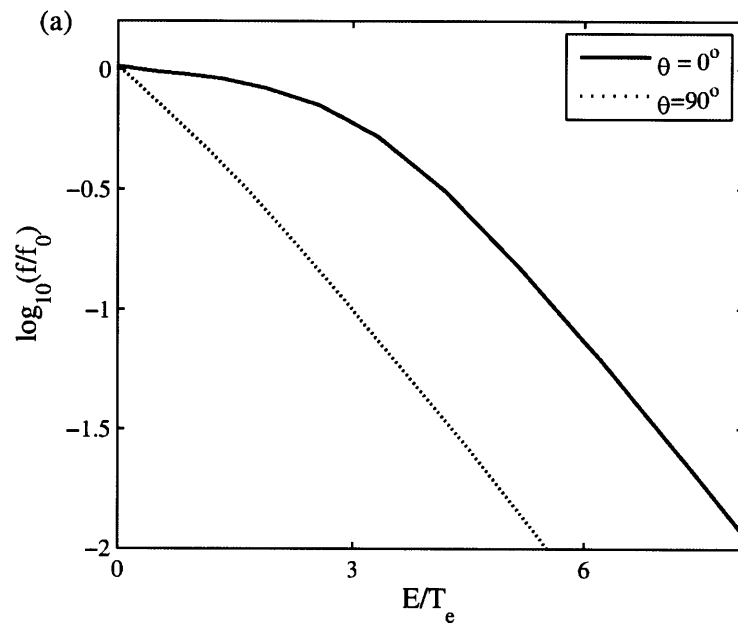


Figure 7-10: Electron distribution for pitch angles parallel and perpendicular to the magnetic field during island merging.

Summary. The theoretical framework of the equations of state may be applied even when there are asymmetries in the plasma density across the current sheet, a situation very typical of Earth's magnetopause. Electron heating tends to be greater on the low density, low β_e magnetospheric side, as demonstrated by Egedal, Le, *et al* in Ref. [71]. 3D reconnection is vastly more complex than 2D reconnection, but the equations of state apply in many 3D reconnection scenarios. The chaotic nature of fully 3D field lines prevents a simple characterization of the global topology of flux tubes, but localized parallel potentials clearly form and trap electrons. The equations of state also apply to island merging, a case where the field lines have a closed topology and do not extend out to an ambient ideal plasma. Substantial anisotropic electron heating occurs at the X line between two merging islands and may be related to electron energization during flares and other impulsive events in the solar corona.

Chapter 8

Summary of New Results

This thesis presents new equations of state for the anisotropic electron pressure tensor during collisionless magnetic reconnection. In the collisionless regime, a kinetic treatment is typically required to understand the complex dynamics of the electrons, including the generation of high-energy electrons observed in a variety of magnetized astrophysical plasmas. The equations of state provide a powerful framework for exploring a dominant effect – electron pressure anisotropy – within a simpler fluid picture. Several predictions are derived and verified in this thesis through comparison to kinetic simulations performed by collaborators. The key new results are listed below:

- **The electron pressure follows the new equations of state during collisionless reconnection with a guide field.** In line with the equations of state, the electron pressure becomes highly anisotropic, typically with $p_{\parallel} \gg p_{\perp}$ near the X line. At the physical mass ratio, the equations of state hold throughout the reconnection region even for a guide field as low as 20% of the reconnecting field. This threshold value of guide field may depend on other plasma parameters, particularly β_e , and this dependence will be explored in future work.
- **Electron pressure anisotropy drives long current layers.** For spacecraft data analysis, it is important to know the electrical current and magnetic field signatures of kinetic reconnection. Based on the results presented in this thesis,

it is clear that electron pressure anisotropy plays a key role in supporting the electron currents and the fields they generate near reconnection sites. Fluid models based on the equations of state can properly account for the electron pressure anisotropy and reproduce the long current layers observed in kinetic codes, as is shown in forthcoming work by Ohia *et al.* Eventually, it will be important to study stability of the electron current layers to secondary instabilities, especially in 3D.

- **The electrons tend to become most energetic in low β_e plasmas.** The value of β_e can be very low in the solar corona and wind, and in Earth's magnetosphere. For values of $\beta_e < 0.01$, the bulk electrons can be heated to 10s or 100s of times the ambient electron temperature. Guided by the predictions of the new equations of state, a paper by Egedal, Daughton, and Le [98] finds extreme electron heating in a kinetic code that agrees with Cluster observations gathered in the geotail during reconnection with $\beta_e \sim 0.003$.

Additional future work could include a systematic study of spacecraft data, including currently available data from the Cluster and THEMIS missions, in light of the models introduced in this thesis. In particular, the maximal energies of electrons accelerated during reconnection could be correlated with measured values of β_e . On the experimental front, Egedal *et al.* have proposed a new laboratory device optimized to study the physics of electron trapping and heating during reconnection in regimes relevant to Earth's magnetosphere. Based on the results presented in Chapter 6, it is important to have the correct ion-to-electron mass ratio. Laboratory experiment is therefore essential because 3D kinetic simulations at the physical proton mass ratio are currently unfeasible.

Appendix A

Waves Launched by Island Merging

It has been suggested that the global motion of islands or flux ropes will generate large-amplitude waves in the external plasma. Some coronal loops undergo damped oscillations, which most likely radiate energy into the ambient plasma in the form of low-frequency waves [132]. The global motion of the islands during coalescence may similarly launch low-frequency waves in the external plasma, and the electron temperature can fluctuate widely depending on the nature of the plasma modes. This phenomenon is captured by the island merging simulations presented in the previous chapter.

The global motion of the plasmoids launches large-amplitude MHD activity in the surrounding plasma. These drive fluctuations in the plasma density of $\delta n/n \gtrsim 0.3$ and in the electron temperature on the order of $\delta T_{e\parallel}/T_{e0} \gtrsim 1$. The exact spectrum of MHD modes excited by the plasmoid motion will of course depend on the plasma conditions, the magnetic field geometry, and the detailed motion of the plasmoids. In laboratory experiments, for example, magnetosonic waves were launched by plasmoid eruption and motion [133]. In the present simulation, the waves are dominated by a single mode, which has the longest parallel wavelength accessible in the periodic simulation domain. This mode is in the ion cyclotron branch, containing obliquely propagating electromagnetic waves with frequencies near the proton cyclotron frequency, $\omega_{cp} = eB/m_p c$. In the simulation, they propagate at an angle of $\sim 84^\circ$ with respect to the magnetic field with a frequency of $\omega/\omega_{cp} \sim 0.4$. The waves are well-described by

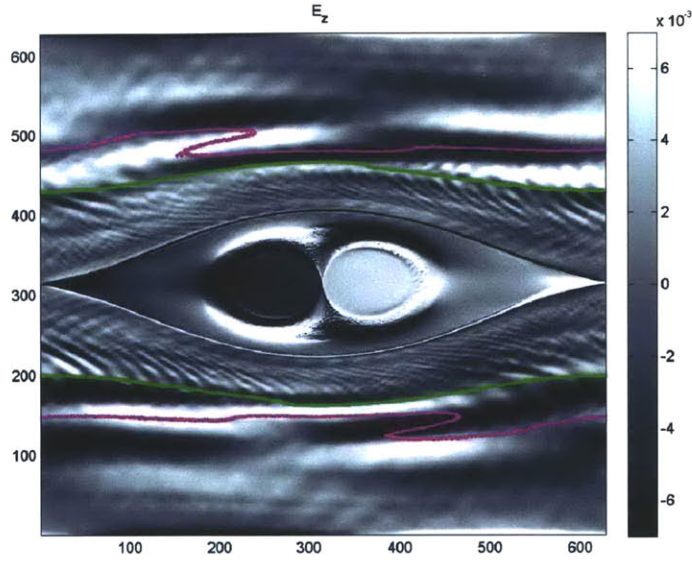


Figure A-1: Electric field component with resonance and cut-off layers.

the cold plasma wave dispersion relation (see, e.g., [134]), although the perpendicular wave number k_{\perp} is shifted $\sim 15\%$ higher due to hot plasma effects. The perpendicular wavelength is somewhat longer than the proton Larmor radius $\rho_p = \sqrt{T_p/m_p}/\omega_{cp}$, with the wave number $k_{\perp}\rho_p \sim 0.6$.

The wave structure is visible in the electric field, and the vertical E_z component (plotted in Fig. A-1) is largest for the mode's polarization. The long-wavelength modes are confined to the lower-density plasma surrounding the islands. The ion cyclotron waves cannot propagate closer to the islands due to the presence of resonance and cut-off layers in the region of varying density. In the regime considered here ($\omega < \omega_{cp} \ll \omega_{pp}$ the proton plasma frequency), these layers reside at densities of

$$n \sim (B^2/4\pi m_p c^2)(c^2 k_{\parallel}^2/\omega^2 - 1) \times F(\omega/\omega_{cp}), \quad (\text{A.1})$$

where $F(\omega/\omega_{cp}) = 1 - (\omega/\omega_{cp})^2$ gives the resonance and $F(\omega/\omega_{cp}) = 1 + (\omega/\omega_{cp})$ gives the cut-off. The resonances and cut-offs are plotted in Fig. A-1. The electron temperature becomes largest near the resonance layer, where the wave electric field

is strongest. In the region of higher plasma density between these layers, shorter wavelength electrostatic fluctuations are visible, but they have a relatively minor effect on the electron temperature.

For the large-amplitude, long-wavelength modes, the effective electron energization is different from the acceleration near the X line. From the particle perspective, the parallel electric field of the ion cyclotron mode is important for the electron motion. In this case, the fluctuations are too fast to allow adiabatic trapping. These modes have a long parallel wavelength, and the corresponding parallel phase velocity is fast compared to the electron thermal speed: $\omega/k_{\parallel} \gtrsim 3\sqrt{(T_e/m_e)}$. In this range, adiabatic trapping does not occur as it does near the X line.

The electron phase space density for a point near the resonance layer (the dot in Fig. A-2) is plotted in Fig. A-3. There are large electron flows in this region ($v_{e\parallel} \sim 0.6v_{the}$), and the distribution is plotted as a function of energy in the electron rest frame. Note that this distribution lacks the flat portion along the parallel direction associated with adiabatically trapped particles. Unlike in the previous case where passing particles all gain the same fixed energy $e\Phi_{\parallel}$, the energy gain of electrons in the wave depends on their initial energy, with slow electrons gaining the least energy. The parallel distribution therefore falls off with a more shallow slope, corresponding to a higher effective temperature.

A simpler fluid picture captures the bulk electron temperature fluctuations, which are the result of the compressional wave motion. For these low-frequency modes, the Chew-Goldberger-Low (CGL) equations of state [81] provide a good approximation for the electron pressure components. The CGL double-adiabatic equations of state may be expected to hold because the fast parallel phase velocity of the waves above the electron thermal speed implies that electron heat transport will be of limited importance. Comparisons to the CGL scalings, $p_{\parallel} \propto n^3/B^2$ and $p_{\perp} \propto nB$, are plotted in Figs. A-2(a,b) for the flux tube marked in magenta in Fig. A-2(a). The electrons are again preferentially heated in the parallel direction due to the strong density dependence of $p_{\parallel} \propto n^3$, and the ratio p_{\parallel}/p_{\perp} plotted Fig. A-2(a) reaches $\gtrsim 2$.

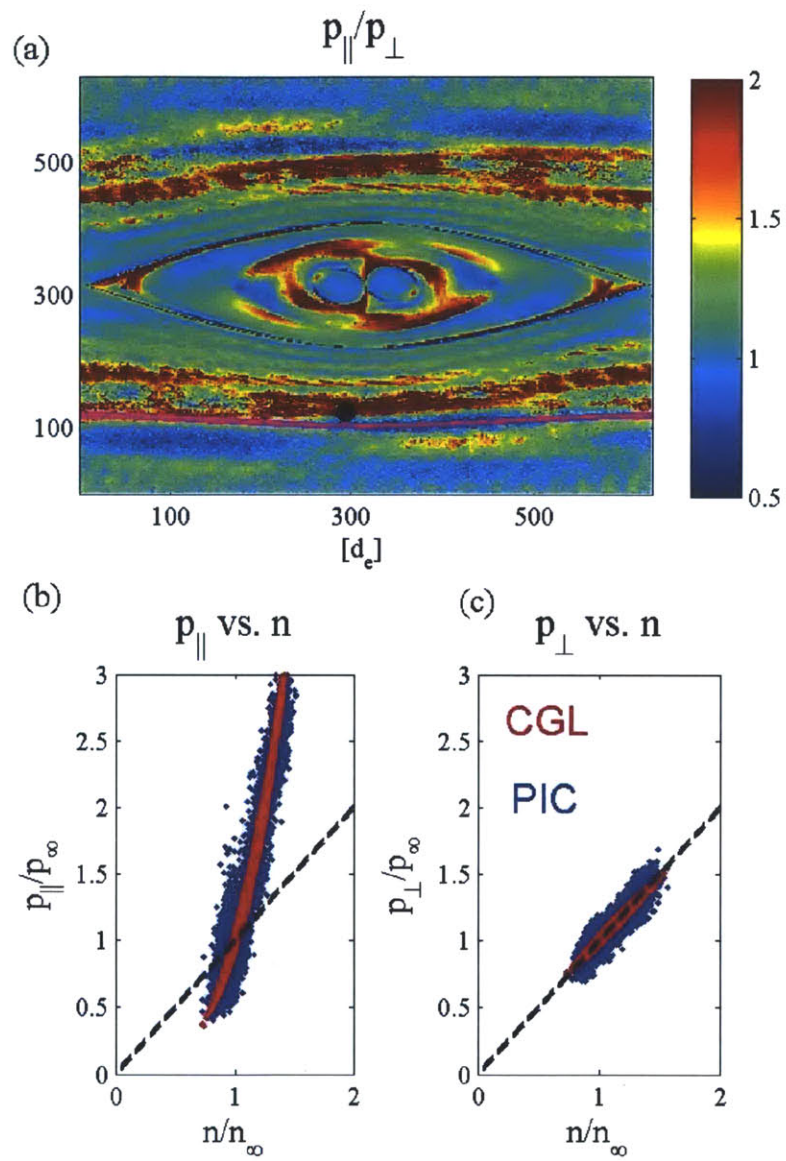


Figure A-2: CGL equations of state hold in the wave.

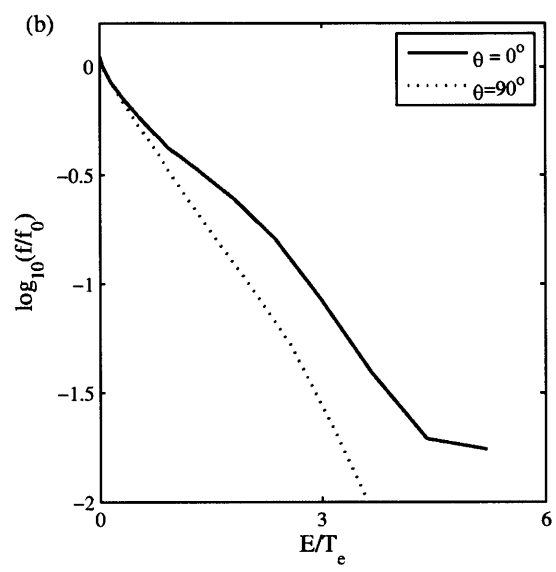


Figure A-3: Electron distribution outside the resonance layer.

Appendix B

Including Collisions

So far, the electron pressure anisotropy described by the new equations of state and its effect on reconnection has been studied in the collisionless limit. It is of interest to know how binary particle collisions alter the picture and how the anisotropy varies with the collisionality. For example, while collisions are often completely negligible for reconnection in the magnetosphere, it is difficult to reach the collisionless regime in laboratory reconnection experiments. In addition, in very dense regions of the lower solar corona, collisionality can be high enough that it competes with other processes.

Collisions can be included in PIC simulations using, for example, the Takizuka-Abe collision operator [135]. This discretized operator converges to the Boltzmann collision operator as the number of numerical particles is increased and the time step is decreased. It is a Monte Carlo method that requires pairing nearby particles and allowing them to exchange momentum with prescribed probabilities, and it is computationally expensive. Some results have been obtained on reconnection in arbitrary collisionality regimes [125].

The parallel potential Φ_{\parallel} from a set of PIC simulations of anti-parallel reconnection are presented in Fig. B-1. The top simulation was performed without collisions. The other two use the same initial plasma conditions (the Harris sheet is the same as considered in Chapter 4 except that the background ion population is cooler by a factor 2.5) and include collisions with electron collision frequencies of $\nu_e/\omega_{ce} = 0.02$ and 0.05. The collision frequency is a free parameter in the numerical model, and it

can be adjusted independently of the temperature and density. The implemented collision frequencies correspond to electron mean free paths (for 90° scattering) of $\lambda_e \sim 2$ and $5d_i$ near the neutral sheet. Because collisions scatter parallel electron energy, the electron anisotropy is reduced. The parallel pressure is smaller, and Φ_{\parallel} is correspondingly reduced at higher collisionality. The electron outflow speed u_{ex} is plotted from the three collisional simulations in Fig. B-2. The inner electron jets become broader and shorter as the collisionality increases. It is important to note that these electron kinetic effects remain significant at low, but non-negligible, collisionality, and this regime is accessible to laboratory experiment.

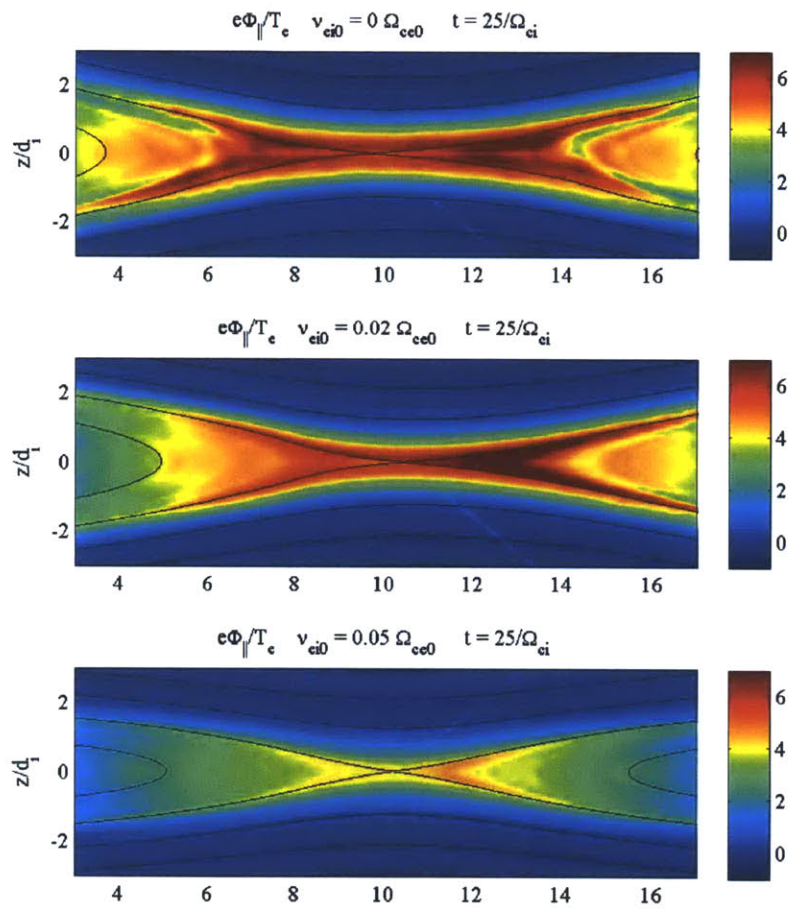


Figure B-1: Acceleration potential in weakly collisional plasmas.

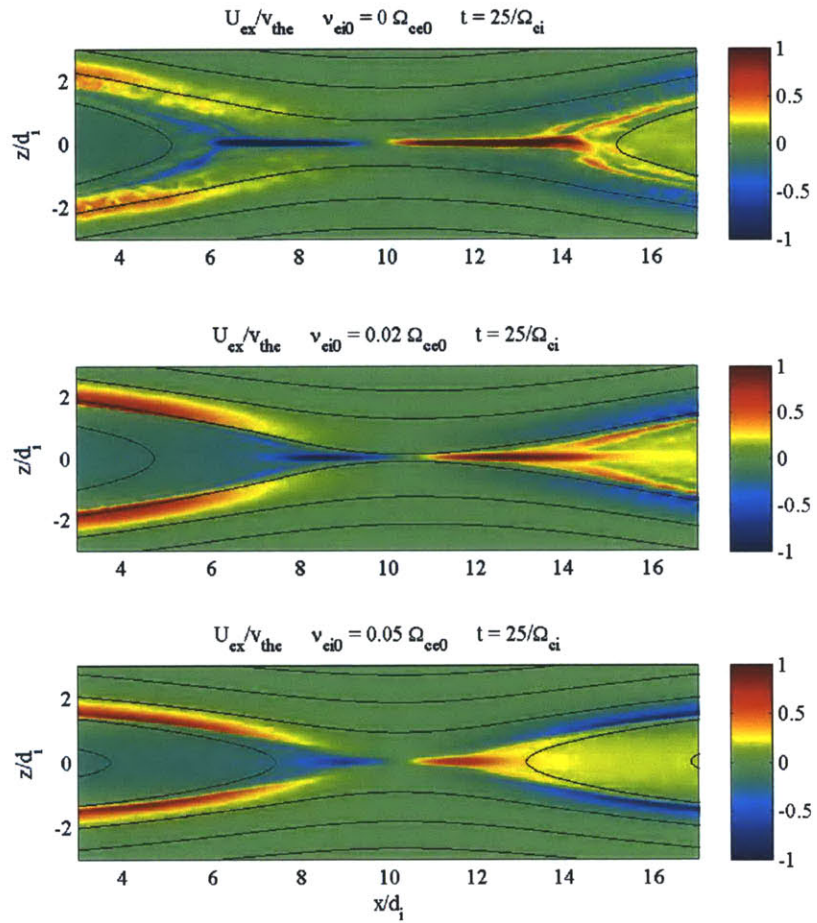


Figure B-2: Electron outflow jets.

Appendix C

Particle-in-Cell Codes

Particle codes have a long history, and some of the earliest computational simulations in the 1950s were particle simulations of electrostatic plasma discharges [136]. Two general classes of particle codes are N-body simulations, in which the interaction potential between each pair of constituent particles is calculated, and particle-in-cell (PIC) methods. PIC codes make use of the mean field approximation, and they solve the Vlasov equation for the 1-particle distribution function by sampling phase space along a large number of particle orbits in self-consistent fields. The fields are defined on a mesh of cells, and the currents and charge densities are computed from the particles within each cell. The field evolution is governed by a discretized version of Maxwell's equations (or some reduced set of Maxwell's equations relevant for a given regime). The earliest PIC codes were 1D electrostatic codes that computed only electron dynamics in a stationary ion background. Modern codes are electromagnetic and trace both electron and ion distributions in up to three spatial dimensions.

The simulations presented in this thesis are results from the code VPIC provided principally by Daughton with some additional data provided by Karimabadi. VPIC is a first-principles electromagnetic relativistic kinetic PIC code, and it is one of a handful of codes that are optimized to make full use of current supercomputers, including Roadrunner (LANL), Jaguar (ORNL), Kraken (NICS), and Pleiades (NASA) [137]. State-of-the-art VPIC simulations model plasmas using $\mathcal{O}(10^{12})$ numerical particles and $\mathcal{O}(10^9)$ voxels running on parallel computing systems with $\mathcal{O}(10^5)$ processing

cores. The 2D simulations presented in this thesis use $\mathcal{O}(10^9)$ numerical particles, while the 3D simulations are among the first to go up to $\mathcal{O}(10^{12})$. VPIC simulations have permitted studies of reconnection and laser-plasma interactions at an unprecedented level of detail [67, 137, 138].

VPIC solves the following relativistic, electromagnetic Maxwell-Boltzmann system of evolution equations:

$$\begin{aligned} \left[\frac{\partial}{\partial t} + \gamma^{-1} \mathbf{u} \cdot \nabla + \frac{q_s}{m_s} (\mathbf{E} + \gamma^{-1} \mathbf{u} \times \mathbf{B}) \cdot \nabla \right] f_s &= \frac{\delta}{\delta t} |_{coll} f_s \\ \frac{\partial}{\partial t} \mathbf{B} &= -\nabla \times \mathbf{E} \\ \frac{\partial}{\partial t} \mathbf{E} &= \epsilon^{-1} \nabla \times \mu^{-1} \mathbf{B} - \epsilon^{-1} \mathbf{J} - \epsilon^{-1} \sigma \mathbf{E}, \end{aligned} \quad (\text{C.1})$$

where f_s is the phase-space distribution of species s or charge q_s and mass m_s , \mathbf{u} is the spatial part of the four-velocity, ϵ and μ are the permittivity and permeability of the background (not necessarily vacuum), σ is a possible background conductivity (not used in any of the simulations presented), and $\delta/\delta t|_{coll}$ is a collision operator that accounts for binary Coulomb collisions or other discrete interactions. The additional Maxwell constraint equations, $\nabla \cdot \mathbf{B} = 0$ and $\nabla \cdot \mathbf{E} = \rho/\epsilon$, are also satisfied. The current density is given by

$$\mathbf{J} = \sum_s \int q_s \gamma^{-1} \mathbf{u} f_s. \quad (\text{C.2})$$

While the code is fully relativistic, for the present applications relativistic corrections to the classical mechanical results are fairly small and the formulas in the main chapters of this thesis are given in the nonrelativistic limit.

A variety of boundary conditions are used in the simulations. The simplest to implement are periodic boundaries, which are employed in the large island simulation in the direction of island merging [123] and in the outflow and initial current flow directions in the 3D simulations [63]. These simulations employed conducting boundary conditions for the electromagnetic fields ($\mathbf{E} \times \hat{\mathbf{n}} = 0$ and $\mathbf{B} \cdot \hat{\mathbf{n}} = 0$, where $\hat{\mathbf{n}}$ is the surface normal unit vector) and reflecting boundary conditions for the particles at the other spatial boundaries. A more sophisticated set of open boundaries were

implemented in most of the Harris sheet reconnection simulations [67]. The open boundaries emulate a larger system by allowing magnetic flux and new particles to enter the system in the inflow, while the plasma exhaust is free to exit the simulation domain. The particles are injected with a drifting, anisotropic multi-Maxwellian such that the lowest three moments of the particle distribution (density n , flow \mathbf{u} , and pressure tensor \mathbb{P}) have zero normal derivative at the boundaries. The field boundary conditions are chosen to allow a Poynting flux of electromagnetic energy out of the system without reflections.

Bibliography

- [1] J. Dungey, “Conditions for the occurrence of electrical discharges in astrophysical systems,” *Philosophical Magazine*, vol. 44, pp. 725–738, JUL 1953.
- [2] V. M. Vasyliunas, “Theoretical models of magnetic field line merging,” *Reviews of Geophysics*, vol. 13, pp. 303–336, FEB 1975.
- [3] E. Priest and T. Forbes, *Magnetic Reconnection*. Cambridge University Press, 2000.
- [4] M. Yamada, R. Kulsrud, and H. Ji, “Magnetic reconnection,” *Rev. Mod. Phys.*, vol. 82, pp. 603–664, Mar 2010.
- [5] R. Giovanelli, “A theory of chromospheric flares,” *Nature*, vol. 158, p. 81, 1946.
- [6] R. Lin and H. Hudson, “10-100 keV electron acceleration and emission from solar flares,” *Solar Physics*, vol. 17, no. 2, pp. 412–&, 1971.
- [7] R. A. Kopp and G. W. Pneuman, “Magnetic reconnection in the corona and the loop prominence phenomenon,” *Solar Physics*, vol. 50, pp. 85–98, 1976. 10.1007/BF00206193.
- [8] B. J. Thompson, S. P. Plunkett, J. B. Gurman, J. S. Newmark, O. C. St. Cyr, and D. J. Michels, “SOHO/EIT observations of an Earth-directed coronal mass ejection on May 12, 1997,” *Geophys. Res. Lett.*, vol. 25, pp. 2465–2468, 1998.
- [9] S. Masuda, T. Kosugi, H. Hara, and Y. Ogawaray, “A loop-top hard X-ray source in a compact solar-flare as evidence for magnetic reconnection,” *Nature*, vol. 371, pp. 495–497, OCT 6 1994.
- [10] N. Nishizuka, H. Takasaki, A. Asai, and K. Shibata, “Multiple plasmoid ejections and associated hard x-ray bursts in the 2000 november 24 flare,” *The Astrophysical Journal*, vol. 711, no. 2, p. 1062, 2010.
- [11] D. E. McKenzie, “Observational studies of reconnection in the solar corona,” *Physics of Plasmas*, vol. 18, no. 11, p. 111205, 2011.
- [12] B. Coppi, G. Laval, and R. Pellat, “Dynamics of the geomagnetic tail,” *Phys. Rev. Lett.*, vol. 16, pp. 1207–1210, JUN 1966.

- [13] G. Paschmann, I. Papamastorakis, N. Scopke, G. Haerendel, B. U. O. Sonnerup, S. J. Bame, J. R. Asbridge, J. T. Gosling, C. T. Russel, and R. C. Elphic, "Plasma acceleration at the earth's magnetopause - Evidence for reconnection," *Nature*, vol. 282, pp. 243–246, Nov. 1979.
- [14] F. S. Mozer, S. D. Bale, and T. D. Phan, "Evidence of diffusion regions at a subsolar magnetopause crossing," *Phys. Rev. Lett.*, vol. 89, p. 015002, Jun 2002.
- [15] T. D. Phan, L. M. Kistler, B. Klecker, G. Haerendel, G. Paschmann, B. U. O. Sonnerup, W. Baumjohann, M. B. Bavassano-Cattaneo, C. W. Carlson, A. M. Dilellis, K. H. Fornacon, L. A. Frank, M. Fujimoto, E. Georgescu, S. Kokubun, E. Moebius, T. Mukai, M. Oieroset, W. R. Paterson, and H. Reme, "Extended magnetic reconnection at the Earth's magnetopause from detection of bi-directional jets," *Nature*, vol. 404, pp. 848–850, APR 20 2000.
- [16] M. Oieroset, T. Phan, M. Fujimoto, R. P. Lin, and R. P. Lepping, "In situ detection of collisionless reconnection in the Earth's magnetotail," *Nature*, vol. 412, pp. 414–417, JUL 26 2001.
- [17] A. Runov, R. Nakamura, W. Baumjohann, R. A. Treumann, T. L. Zhang, M. Volwerk, Z. Voros, A. Balogh, K. H. Glassmeier, B. Klecker, H. Reme, and L. Kistler, "Current sheet structure near magnetic X-line observed by Cluster," *Geophys. Res. Lett.*, vol. 30, JUN 10 2003.
- [18] V. Angelopoulos, J. P. McFadden, D. Larson, C. W. Carlson, S. B. Mende, H. Frey, T. Phan, D. G. Sibeck, K.-H. Glassmeier, U. Auster, E. Donovan, I. R. Mann, I. J. Rae, C. T. Russell, A. Runov, X.-Z. Zhou, and L. Kepko, "Tail reconnection triggering substorm onset," *SCIENCE*, vol. 321, pp. 931–935, AUG 15 2008.
- [19] T. Nagai, I. Shinohara, M. Fujimoto, M. Hoshino, Y. Saito, S. Machida, and T. Mukai, "Geotail observations of the hall current system: Evidence of magnetic reconnection in the magnetotail," *J. Geophys. Res.*, vol. 106, pp. 25929–25949, NOV 1 2001.
- [20] M. Oieroset, R. Lin, and T. Phan, "Evidence for electron acceleration up to 300 keV in the magnetic reconnection diffusion region of earth's magnetotail," *Phys. Rev. Lett.*, vol. 89, p. 195001, NOV 4 2002.
- [21] I. I. Vogiatzis, T. A. Fritz, Q. G. Zong, and E. T. Sarris, "Two distinct energetic electron populations of different origin in the Earth's magnetotail: a Cluster case study," *Annales Geophysicae*, vol. 24, no. 7, pp. 1931–1948, 2006.
- [22] R. Nakamura, W. Baumjohann, Y. Asano, A. Runov, A. Balogh, C. J. Owen, A. N. Fazakerley, M. Fujimoto, B. Klecker, and H. Reme, "Dynamics of thin current sheets associated with magnetotail reconnection," *J. Geophys. Res.*, vol. 111, NOV 8 2006.

- [23] A. Asnes, M. G. G. T. Taylor, A. L. Borg, B. Lavraud, R. W. H. Friedel, C. P. Escoubet, H. Laakso, P. Daly, and A. N. Fazakerley, "Multispacecraft observation of electron beam in reconnection region," *J. Geophys. Res.*, vol. 113, MAY 10 2008.
- [24] Y. Asano, R. Nakamura, I. Shinohara, M. Fujimoto, T. Takada, W. Baumjohann, C. J. Owen, A. N. Fazakerley, A. Runov, T. Nagai, E. A. Lucek, and H. Reme, "Electron flat-top distributions around the magnetic reconnection region," *J. Geophys. Res.*, vol. 113, JAN 24 2008.
- [25] L. J. Chen, N. Bessho, B. Lefebvre, H. Vaith, A. Asnes, O. Santolik, A. w Fazakerley, P. Puhl-Quinn, A. Bhattacharjee, Y. Khotyaintsev, P. Daly, and R. Torbert, "Multispacecraft observations of the electron current sheet, neighboring magnetic islands, and electron acceleration during magnetotail reconnection," *Phys. Plasmas*, vol. 16, no. 5, p. 056501, 2009.
- [26] S. Curtis, ed., *The Magnetospheric Multiscale Mission...Resolving Fundamental Processes in Space Plasmas*, Dec. 1999.
- [27] M. L. Stevens, *Magnetic reconnection physics in the solar wind with Voyager 2*. PhD thesis, MIT, 2009.
- [28] J. D. Richardson, J. W. Belcher, R. S. Selesnick, M. Zhang, and G. L. Siscoe, "Evidence for periodic reconnection at Uranus?," *Geophys. Res. Lett.*, vol. 15, pp. 733–736, Aug. 1988.
- [29] S. von Goeler, W. Stodiek, and N. Sauthoff, "Studies of internal disruptions and $m=1$ oscillations in tokamak discharges with soft X-ray techniques," *Phys. Rev. Lett.*, vol. 33, pp. 1201–1203, NOV 1974.
- [30] B. B. Kadomtsev, "Disruptive instability in Tokamaks," *Soviet Journal of Plasma Physics*, vol. 1, pp. 710–715, Oct. 1975.
- [31] N. Sauthoff, S. V. Goeler, and W. Stodiek, "A study of disruptive instabilities in the plt tokamak using x-ray techniques," *Nuclear Fusion*, vol. 18, no. 10, p. 1445, 1978.
- [32] J. Egedal, W. Fox, N. Katz, M. Porkolab, K. Reim, and E. Zhang, "Laboratory observations of spontaneous magnetic reconnection," *Phys. Rev. Lett.*, vol. 98, p. 015003, JAN 5 2007.
- [33] N. Katz, J. Egedal, W. Fox, A. Le, J. Bonde, and A. Vrublevskis, "Laboratory observation of localized onset of magnetic reconnection," *Phys. Rev. Lett.*, vol. 104, p. 255004, JUN 25 2010.
- [34] W. Fox, M. Porkolab, J. Egedal, N. Katz, and A. Le, "Laboratory observation of electron phase-space holes during magnetic reconnection," *Phys. Rev. Lett.*, vol. 101, p. 255003, DEC 19 2008.

- [35] R. Stenzel, W. Gekelman, and N. Wild, “Magnetic field line reconnection experiments, 5. current disruptions and double layers,” *J. Geophys. Res.*, vol. 88, pp. 4793–4804, JUN 1983.
- [36] M. Yamada, H. T. Ji, S. Hsu, T. Carter, R. Kulsrud, N. Bretz, F. Jobes, Y. Ono, and F. Perkins, “Study of driven magnetic reconnection in a laboratory plasma,” *Phys. Plasmas*, vol. 4, pp. 1936–1944, MAY 1997.
- [37] Y. Ren, M. Yamada, S. Gerhardt, H. T. Ji, R. Kulsrud, and A. Kuritsyn, “Experimental verification of the Hall effect during magnetic reconnection in a laboratory plasma,” *Phys. Rev. Lett.*, vol. 95, p. 055003, JUL 29 2005.
- [38] M. R. Brown, C. D. Cothran, and J. Fung, “Two fluid effects on three-dimensional reconnection in the Swarthmore Spheromak Experiment with comparisons to space data,” *Phys. Plasmas*, vol. 13, p. 056503, MAY 2006.
- [39] T. P. Intrator, X. Sun, G. Lapenta, L. Dorf, and I. Furno, “Experimental onset threshold and magnetic pressure pile-up for 3D reconnection,” *Nature Physics*, vol. 5, pp. 521–526, July 2009.
- [40] W. Fox, A. Bhattacharjee, and K. Germaschewski, “Fast magnetic reconnection in laser-produced plasma bubbles,” *Phys. Rev. Lett.*, vol. 106, p. 215003, May 2011.
- [41] P. M. Nilson, L. Willingale, M. C. Kaluza, C. Kamperidis, S. Minardi, M. S. Wei, P. Fernandes, M. Notley, S. Bandyopadhyay, M. Sherlock, R. J. Kingham, M. Tatarakis, Z. Najmudin, W. Rozmus, R. G. Evans, M. G. Haines, A. E. Dangor, and K. Krushelnick, “Magnetic reconnection and plasma dynamics in two-beam laser-solid interactions,” *Phys. Rev. Lett.*, vol. 97, p. 255001, Dec 2006.
- [42] C. K. Li, F. H. Séguin, J. A. Frenje, J. R. Rygg, R. D. Petrasso, R. P. J. Town, O. L. Landen, J. P. Knauer, and V. A. Smalyuk, “Observation of megagauss-field topology changes due to magnetic reconnection in laser-produced plasmas,” *Phys. Rev. Lett.*, vol. 99, p. 055001, Aug 2007.
- [43] H. Alfvén, *Cosmical electrodynamics*. 1950.
- [44] M. A. Berger and G. B. Field, “The topological properties of magnetic helicity,” *Journal of Fluid Mechanics*, vol. 147, pp. 133–148, Oct. 1984.
- [45] V. I. Arnol’d and B. A. Khesin, “Topological methods in hydrodynamics,” *Annual Review of Fluid Mechanics*, vol. 24, pp. 145–166, 1992.
- [46] J. B. Taylor, “Relaxation of toroidal plasma and generation of reverse magnetic fields,” *Phys. Rev. Lett.*, vol. 33, pp. 1139–1141, Nov 1974.

- [47] K. Schindler, M. Hesse, and J. Birn, “General magnetic reconnection, parallel electric fields, and helicity,” *J. Geophys. Res.*, vol. 93, pp. 5547–5557, June 1988.
- [48] A. H. Boozer, “The evolution of magnetic fields and plasmas in open field line configurations,” *Physics of Fluids B*, vol. 2, pp. 2300–2305, Oct. 1990.
- [49] B. U. Ö. Sonnerup, *Magnetic field reconnection, in Solar System Plasma Physics, vol. 3.* edited by L. T. Lanzerotti, C. F. Kennel, and E. N. Parker, pp. 45–108, North-Holland, New York, 1979.
- [50] Z. Ma and A. Bhattacharjee, “Hall magnetohydrodynamic reconnection: The geospace environment modeling challenge,” *J. Geophys. Res.*, vol. 106, pp. 3773–3782, MAR 1 2001.
- [51] J. D. Huba and L. I. Rudakov, “Hall magnetic reconnection rate,” *Phys. Rev. Lett.*, vol. 93, p. 175003, Oct 2004.
- [52] J. F. Drake, M. A. Shay, and M. Swisdak, “The Hall fields and fast magnetic reconnection,” *Physics of Plasmas*, vol. 15, p. 042306, Apr. 2008.
- [53] W. Daughton and H. Karimabadi, “Collisionless magnetic reconnection in large-scale electron-positron plasmas,” *Physics of Plasmas*, vol. 14, no. 7, p. 072303, 2007.
- [54] B. Coppi and P. Detragiache, “Mesoscopic plasma modes producing magnetic reconnection,” *Annals of Physics*, vol. 225, no. 1, pp. 59 – 82, 1993.
- [55] J. D. Huba, N. T. Gladd, and K. Papadopoulos, “The lower-hybrid-drift instability as a source of anomalous resistivity for magnetic field line reconnection,” *Geophys. Res. Lett.*, vol. 4, pp. 125–126, 1977.
- [56] E. N. Parker, “Sweet’s mechanism for merging magnetic fields in conducting fluids,” *J. Geophys. Res.*, vol. 62, pp. 509–520, 1957.
- [57] H. E. Petschek, “Magnetic Field Annihilation,” *NASA Special Publication*, vol. 50, p. 425, 1964.
- [58] H. P. Furth, J. Killeen, and M. N. Rosenbluth, “Finite-resistivity instabilities of a sheet pinch,” *Physics of Fluids*, vol. 6, no. 4, pp. 459–484, 1963.
- [59] W. Daughton, “Kinetic theory of the drift kink instability in a current sheet,” *J. Geophys. Res.*, vol. 103, pp. 29429–29444, Dec. 1998.
- [60] A. Sykes and J. A. Wesson, “Relaxation instability in tokamaks,” *Phys. Rev. Lett.*, vol. 37, pp. 140–143, Jul 1976.
- [61] J. A. Wesson, “Sawtooth reconnection,” *Nuclear Fusion*, vol. 30, pp. 2545–2549, DEC 1990.

- [62] A. Y. Aydemir, “Nonlinear studies of $m=1$ modes in high-temperature plasmas,” *Physics of Fluids B-Plasma Physics*, vol. 4, pp. 3469–3472, NOV 1992.
- [63] W. Daughton, V. Roytershteyn, H. Karimabadi, L. Yin, B. J. Albright, B. Bergen, and K. J. Bowers, “Role of electron physics in the development of turbulent magnetic reconnection in collisionless plasmas,” *Nature Physics*, vol. 7, pp. 539–542, July 2011.
- [64] J. Birn, J. F. Drake, M. A. Shay, B. N. Rogers, R. E. Denton, M. Hesse, M. Kuznetsova, Z. W. Ma, A. Bhattacharjee, A. Otto, and P. L. Pritchett, “Geospace environmental modeling (GEM) magnetic reconnection challenge,” *J. Geophys. Res.*, vol. 106, pp. 3715–3719, MAR 1 2001.
- [65] J. Egedal, M. Oieroset, W. Fox, and L. R. P., “In situ discovery of an electrostatic potential, trapping electrons and mediating fast reconnection in the Earth’s magnetotail,” *Phys. Rev. Lett.*, vol. 94, p. 025006, JAN 21 2005.
- [66] J. Egedal, W. Fox, N. Katz, M. Porkolab, M. Oieroset, R. P. Lin, W. Daughton, and D. J. F., “Evidence and theory for trapped electrons in guide field magnetotail reconnection,” *J. Geophys. Res.*, vol. 113, p. A12207, MAR 25 2008.
- [67] W. Daughton, J. Scudder, and H. Karimabadi, “Fully kinetic simulations of undriven magnetic reconnection with open boundary conditions,” *Phys. Plasmas*, vol. 13, p. 072101, JUL 2006.
- [68] A. Le, J. Egedal, W. Daughton, W. Fox, and N. Katz, “Equations of state for collisionless guide-field reconnection,” *Phys. Rev. Lett.*, vol. 102, p. 085001, FEB 27 2009.
- [69] A. Le, J. Egedal, W. Fox, N. Katz, A. Vrublevskis, W. Daughton, and J. F. Drake, “Equations of state in collisionless magnetic reconnection,” *Phys. Plasmas*, vol. 17, p. 055703, MAY 2010. 51st Annual Meeting of the Division of Plasma Physics of the American Physical Society, Atlanta, GA, NOV 02-06, 2009.
- [70] A. Le, J. Egedal, W. Daughton, J. F. Drake, W. Fox, and N. Katz, “Magnitude of the Hall fields during magnetic reconnection,” *Geophys. Res. Lett.*, vol. 37, p. L03106, FEB 11 2010.
- [71] J. Egedal, A. Le, P. L. Pritchett, and W. Daughton, “Electron dynamics in two-dimensional asymmetric anti-parallel reconnection,” *Physics of Plasmas*, vol. 18, no. 10, p. 102901, 2011.
- [72] J. Egedal, W. Fox, M. Porkolab, and A. Fasoli, “Experimental evidence of fast reconnection via trapped electron motion,” *Phys. Plasmas*, vol. 11, pp. 2844–2851, MAY 2004.
- [73] E. M. Lifshitz and L. P. Pitaevskii, *Physical kinetics*. 1981.

- [74] J. Buchner and L. Zelenyi, "Regular and chaotic charged-particle motion in magnetotail-like field reversals .1. basic theory of trapped motion," *J. Geophys. Res.*, vol. 94, pp. 11821–11842, SEP 1 1989.
- [75] R. G. Littlejohn, "Hamiltonian formulation of guiding center motion," *Physics of Fluids*, vol. 24, no. 9, pp. 1730–1749, 1981.
- [76] R. B. White, A. H. Boozer, and R. Hay, "Drift hamiltonian in magnetic coordinates," *Physics of Fluids*, vol. 25, no. 3, pp. 575–576, 1982.
- [77] T. G. Northrop, "Adiabatic Charged-Particle Motion," *Reviews of Geophysics and Space Physics*, vol. 1, pp. 283–304, 1963.
- [78] F. S. Mozer and P. L. Pritchett, "Spatial, temporal, and amplitude characteristics of parallel electric fields associated with subsolar magnetic field reconnection," *Journal of Geophysical Research (Space Physics)*, vol. 115, p. 4220, Apr. 2010.
- [79] S. I. Braginskii, "Transport Processes in a Plasma," *Reviews of Plasma Physics*, vol. 1, p. 205, 1965.
- [80] P. B. Snyder, G. W. Hammett, and W. Dorland, "Landau fluid models of collisionless magnetohydrodynamics," *Physics of Plasmas*, vol. 4, no. 11, pp. 3974–3985, 1997.
- [81] G. F. Chew, M. L. Goldberger, and F. E. Low, "The Boltzmann equation and the one-fluid hydromagnetic equations in the absence of particle collisions," *Proc. Royal Soc. A*, vol. 112, p. 236, 1956.
- [82] R. Fitzpatrick, "Scaling of forced magnetic reconnection in the hall-magnetohydrodynamic taylor problem," *Physics of Plasmas*, vol. 11, no. 3, pp. 937–946, 2004.
- [83] D. Biskamp, E. Schwarz, and J. F. Drake, "Two-fluid theory of collisionless magnetic reconnection," *Phys. Plasmas*, vol. 4, pp. 1002–1009, APR 1997.
- [84] M. Hesse, "Dissipation in magnetic reconnection with a guide magnetic field," *Phys. Plasmas*, vol. 13, p. 122107, DEC 2006.
- [85] E. Harris, "On a plasma sheath separating regions of oppositely directed magnetic field," *Il Nuovo Cimento (1955-1965)*, vol. 23, pp. 115–121, 1962. 10.1007/BF02733547.
- [86] A. L. Borg, M. Øieroset, T. D. Phan, F. S. Mozer, A. Pedersen, C. Mouikis, J. P. McFadden, C. Twitty, A. Balogh, and H. Rème, "Cluster encounter of a magnetic reconnection diffusion region in the near-Earth magnetotail on September 19, 2003," *Geophys. Res. Lett.*, vol. 32, p. 19105, Oct. 2005.

- [87] M. Hesse, K. Schindler, J. Birn, and M. Kuznetsova, "The diffusion region in collisionless magnetic reconnection," *Physics of Plasmas*, vol. 6, no. 5, pp. 1781–1795, 1999.
- [88] M. A. Shay, J. F. Drake, and M. Swisdak, "Two-scale structure of the electron dissipation region during collisionless magnetic reconnection," *Phys. Rev. Lett.*, vol. 99, OCT 12 2007.
- [89] H. Karimabadi, W. Daughton, and J. Scudder, "Multi-scale structure of the electron diffusion region," *Geophys. Res. Lett.*, vol. 34, p. L13104, JUL 2007.
- [90] M. Hesse, S. Zenitani, and A. Klimas, "The structure of the electron outflow jet in collisionless magnetic reconnection," *Phys. Plasmas*, vol. 15, no. 11, p. 112102, 2008.
- [91] J. R. Wygant, C. A. Cattell, R. Lysak, Y. Song, J. Dombeck, J. McFadden, F. S. Mozer, C. W. Carlson, G. Parks, E. A. Lucek, A. Balogh, M. Andre, H. Reme, M. Hesse, and C. Mouikis, "Cluster observations of an intense normal component of the electric field at a thin reconnecting current sheet in the tail and its role in the shock-like acceleration of the ion fluid into the separatrix region," *J. Geophys. Res.*, vol. 110, SEP 3 2005.
- [92] S. W. H. Cowley, "The effect of pressure anisotropy on the equilibrium structure of magnetic current sheets," *Planetary and Space Science*, vol. 26, no. 11, pp. 1037 – 1061, 1978.
- [93] S. W. H. Cowley, "A note on the motion of charged particles in one-dimensional magnetic current sheets," *Planetary and Space Science*, vol. 26, no. 6, pp. 539 – 545, 1978.
- [94] L. J. Chen, N. Bessho, B. Lefebvre, H. Vaith, A. Fazakerley, A. Bhattacharjee, P. A. Puhl-Quinn, A. Runov, Y. Khotyaintsev, A. Vaivads, E. Georgescu, and R. Torbert, "Evidence of an extended electron current sheet and its neighboring magnetic island during magnetotail reconnection," *J. Geophys. Res.*, vol. 113, DEC 19 2008.
- [95] G. A. Gary, "Plasma Beta above a Solar Active Region: Rethinking the Paradigm," *Solar Physics*, vol. 203, pp. 71–86, Oct. 2001.
- [96] R. P. Lin, D. W. Potter, D. A. Gurnett, and F. L. Scarf, "Energetic electrons and plasma waves associated with a solar type III radio burst," *Astrophys. J.*, vol. 251, pp. 364–373, Dec. 1981.
- [97] J. Egedal, W. Daughton, J. F. Drake, N. Katz, and A. Le, "Formation of a localized acceleration potential during magnetic reconnection with a guide field," *Phys. Plasmas*, vol. 16, p. 050701, MAY 2009.
- [98] J. Egedal, W. Daughton, and A. Le, "Large-scale electron acceleration by parallel electric fields during magnetic reconnection," *Nature Phys.*, 2012.

- [99] J. Egedal, A. Le, N. Katz, L. J. Chen, B. Lefebvre, W. Daughton, and A. Fazakerley, "Cluster observations of bidirectional beams caused by electron trapping during antiparallel reconnection," *J. Geophys. Res.*, vol. 115, p. A03214, MAR 23 2010.
- [100] J. Ng, J. Egedal, A. Le, W. Daughton, and L. J. Chen, "Kinetic structure of the electron diffusion region in antiparallel magnetic reconnection," *Phys. Rev. Lett.*, vol. 106, FEB 10 2011.
- [101] G. Paschmann, "Recent in-situ observations of magnetic reconnection in near-Earth space," *Geophys. Res. Lett.*, vol. 35, p. 19109, Oct. 2008.
- [102] J. D. Huba, "Hall magnetic reconnection: Guide field dependence," *Physics of Plasmas*, vol. 12, no. 1, p. 012322, 2005.
- [103] M. Swisdak, J. F. Drake, M. A. Shay, and J. G. McIlhargey, "Transition from antiparallel to component magnetic reconnection," *Journal of Geophysical Research (Space Physics)*, vol. 110, p. 5210, May 2005.
- [104] M. V. Goldman, G. Lapenta, D. L. Newman, S. Markidis, and H. Che, "Jet deflection by very weak guide fields during magnetic reconnection," *Phys. Rev. Lett.*, vol. 107, p. 135001, Sep 2011.
- [105] P. Pritchett, "Particle-in-cell simulations of magnetosphere electrodynamics," *Plasma Science, IEEE Transactions on*, vol. 28, pp. 1976–1990, dec 2000.
- [106] M. Hoshino, T. Mukai, T. Terasawa, and I. Shinohara, "Suprathermal electron acceleration in magnetic reconnection," *J. Geophys. Res.*, vol. 106, pp. 25979–25997, NOV 1 2001.
- [107] T. D. Phan, J. F. Drake, M. A. Shay, F. S. Mozer, and J. P. Eastwood, "Evidence for an elongated (~ 60 ion skin depths) electron diffusion region during fast magnetic reconnection," *Phys. Rev. Lett.*, vol. 99, DEC 21 2007.
- [108] R. Horiuchi and T. Sato, "Particle simulation study of driven magnetic reconnection in a collisionless plasma," tech. rep., June 1994.
- [109] R. G. Kleva, J. F. Drake, and F. L. Waelbroeck, "Fast reconnection in high-temperature plasmas," *Phys. Plasmas*, vol. 2, pp. 23–34, JAN 1995.
- [110] B. U. O. Sonnerup and L. J. Cahill, Jr., "Magnetopause Structure and Attitude from Explorer 12 Observations," *J. Geophys. Res.*, vol. 72, p. 171, Jan. 1967.
- [111] F. S. Mozer, P. L. Pritchett, J. Bonnell, D. Sundkvist, and M. T. Chang, "Observations and simulations of asymmetric magnetic field reconnection," *Journal of Geophysical Research (Space Physics)*, vol. 113, p. 0, Nov. 2008.
- [112] M. Øieroset, T. D. Phan, M. Fujimoto, and R. P. Lin, "Wind Observations of Asymmetric Magnetic Reconnection in the Distant Magnetotail," *AGU Fall Meeting Abstracts*, Dec. 2003.

- [113] P. A. Cassak and M. A. Shay, “Scaling of asymmetric magnetic reconnection: General theory and collisional simulations,” *Phys. Plasmas*, vol. 14, OCT 2007.
- [114] J. Birn, J. E. Borovsky, and M. Hesse, “Properties of asymmetric magnetic reconnection,” *Phys. Plasmas*, vol. 15, MAR 2008.
- [115] F. Mozer and P. Pritchett, “The spatial, temporal, and amplitude characteristics of parallel electric fields associated with sub-solar magnetic field reconnection,” *submitted to JGR*,, 2009.
- [116] H. W. Babcock, “The Topology of the Sun’s Magnetic Field and the 22-YEAR Cycle,” *Astrophys. J.*, vol. 133, p. 572, Mar. 1961.
- [117] D. S. Brown and E. R. Priest, “The topological behaviour of 3D null points in the Sun’s corona,” *Astron. and Astrophys.*, vol. 367, pp. 339–346, Feb. 2001.
- [118] C. J. Xiao, X. G. Wang, Z. Y. Pu, H. Zhao, J. X. Wang, Z. W. Ma, S. Y. Fu, M. G. Kivelson, Z. X. Liu, Q. G. Zong, K. H. Glassmeier, A. Balogh, A. Korth, H. Reme, and C. P. Escoubet, “In situ evidence for the structure of the magnetic null in a 3d reconnection event in the earth’s magnetotail,” *Nature Physics*, vol. 2, pp. 478–483, JUL 2006.
- [119] E. R. Priest and P. Démoulin, “Three-dimensional magnetic reconnection without null points. 1. Basic theory of magnetic flipping,” *J. Geophys. Res.*, vol. 100, pp. 23443–23464, Dec. 1995.
- [120] W. Gekelman, E. Lawrence, A. Collette, S. Vincena, B. Van Compernelle, P. Pribyl, M. Berger, and J. Campbell, “Magnetic field line reconnection in the current systems of flux ropes and Alfvén waves,” *Physica Scripta Volume T*, vol. 142, p. 014032, Dec. 2010.
- [121] N. F. Loureiro, A. A. Schekochihin, and S. C. Cowley, “Instability of current sheets and formation of plasmoid chains,” *Physics of Plasmas*, vol. 14, no. 10, p. 100703, 2007.
- [122] N. Gopalswamy, S. Yashiro, M. L. Kaiser, R. A. Howard, and J.-L. Bougeret, “Radio signatures of coronal mass ejection interaction: Coronal mass ejection cannibalism?,” *The Astrophysical Journal Letters*, vol. 548, no. 1, p. L91, 2001.
- [123] H. Karimabadi, J. Dorelli, V. Roytershteyn, W. Daughton, and L. Chacón, “Flux pileup in collisionless magnetic reconnection: Bursty interaction of large flux ropes,” *Phys. Rev. Lett.*, Jul 2011.
- [124] A. Bhattacharjee, Y.-M. Huang, H. Yang, and B. Rogers, “Fast reconnection in high-Lundquist-number plasmas due to the plasmoid Instability,” *Physics of Plasmas*, vol. 16, p. 112102, Nov. 2009.

- [125] W. Daughton, V. Roytershteyn, B. J. Albright, H. Karimabadi, L. Yin, and K. J. Bowers, "Transition from collisional to kinetic regimes in large-scale reconnection layers," *Phys. Rev. Lett.*, vol. 103, p. 065004, Aug 2009.
- [126] S. Tsuneta, "Moving plasmoid and formation of the neutral sheet in a solar flare," *The Astrophysical Journal*, vol. 483, no. 1, p. 507, 1997.
- [127] M. Karlický, "Series of high-frequency slowly drifting structures mapping the flare magnetic field reconnection," *A&A*, vol. 417, no. 1, pp. 325–332, 2004.
- [128] V. M. Fadeev, I. F. Kvabtskhava, and N. N. Komarov, "Self-focusing of local plasma currents," *Nuclear Fusion*, vol. 5, no. 3, p. 202, 1965.
- [129] J. M. Finn and P. K. Kaw, "Coalescence instability of magnetic islands," *Physics of Fluids*, vol. 20, no. 1, pp. 72–78, 1977.
- [130] A. Akmal, J. C. Raymond, A. Vourlidas, B. Thompson, A. Ciaravella, Y.-K. Ko, M. Uzzo, and R. Wu, "Soho observations of a coronal mass ejection," *The Astrophysical Journal*, vol. 553, no. 2, p. 922, 2001.
- [131] K. Shibata and S. Tanuma, "Plasmoid-induced-reconnection and fractal reconnection," *Earth, Planets, and Space*, vol. 53, pp. 473–482, June 2001.
- [132] V. Nakariakov, L. Ofman, E. DeLuca, B. Roberts, and J. M. Davila, "Trace observation of damped coronal loop oscillations: Implications for coronal heating," *Science*, vol. 285, pp. 862–864, AUG 6 1999.
- [133] S. K. P. Tripathi and W. Gekelman, "Laboratory simulation of arched magnetic flux rope eruptions in the solar atmosphere," *Phys. Rev. Lett.*, Aug 2010.
- [134] T. H. Stix, *Waves in plasmas*. 1992.
- [135] T. Takizuka and H. Abe, "A binary collision model for plasma simulation with a particle code," *Journal of Computational Physics*, vol. 25, no. 3, pp. 205 – 219, 1977.
- [136] C. Birdsall, "Particle-in-cell charged-particle simulations, plus monte carlo collisions with neutral atoms, pic-mcc," *Plasma Science, IEEE Transactions on*, vol. 19, pp. 65 –85, apr 1991.
- [137] L. Yin, B. Albright, K. Bowers, W. Daughton, T. Kwan, J. Margulies, E. Nelson, and H. Karimabadi, "New insights into collisionless magnetic reconnection enabled by ultra-high performance three-dimensional kinetic simulations," *Plasma Science, IEEE Transactions on*, vol. 36, pp. 1110 –1111, aug. 2008.
- [138] K. J. Bowers, B. J. Albright, L. Yin, B. Bergen, and T. J. T. Kwan, "Ultra-high performance three-dimensional electromagnetic relativistic kinetic plasma simulation," *Physics of Plasmas*, vol. 15, no. 5, p. 055703, 2008.